Ground deformation detection based on ALOS-PALSAR data utilizing DInSAR technique in Indonesia

(ALOS－PALSAR データの合成開口レーダ干渉法による

インドネシアにおける地殻変動の検出)

AGUSTAN

Doctor of Science

Graduate School of Environmental Studies

Nagoya University

2010

Ground deformation detection based on ALOS-PALSAR data utilizing DInSAR technique in Indonesia

(ALOS－PALSAR データの合成開口レーダ干渉法による
インドネシアにおける地殻変動の検出)

AGUSTAN

A dissertation for the degree of Doctor of Science
Department of Earth and Environmental Sciences,
Graduate School of Environmental Studies,
Nagoya University

2010

….is it ***true?***

“Then which of the Blessings of your Lord will you deny?”

ABSTRACT

Indonesia is located in a junction of four world's major plates, namely Eurasian, Australian, Pacific and Philippines plates. These plates subduct and collide with each other and make Indonesia prone to disaster considering the number of population that live in vulnerable areas. Ground deformation can be utilized to identify the vulnerable areas and also to understand the tectonic and volcanic processes that occur in particular region. However, ground deformation monitoring systems are not well developed yet in almost every part of the country.

Interferometric Synthetic Aperture Radar (InSAR) is one technique that can monitor ground deformation by measuring phase differences of the same ground pixel of Earth's surface. This technique is promising for observation of ground deformation in tropical rainforest area by utilizing L-band SAR data, especially in developing countries that lack ground deformation monitoring network systems.

The research presented in this dissertation aims to obtain the best strategies in InSAR data processing for ground deformation detection in Indonesia. Ground deformations related to seismic and volcanic processes are the main objects in this research. This research detects the ground deformation based on differential InSAR and discusses the mechanism of earthquake of Mw 7.6 January 2009 Papua earthquake, volcanic eruptions at Ibu Volcano in April 2008, and Anak Krakatau Volcano in October 2008. For ground deformation detection related to volcanic activity associated with eruptions, it is difficult to obtain clear fringes directly from InSAR data processing due to noises caused by conditions in the surrounding environment, especially from volcanic ash. To enhance the ground deformation signal, InSAR data processing strategies are extended with post-processed filtering technique. This method is applied after phase unwrapping and converting the deformation value of each pixel into grid format. It is found that a non-convolution spatial filtering method is proven to enhance the similarities of grids and suppress noise of InSAR deformation estimates hence a reliable displacement quantity is obtained. Based on this estimates, the mechanism of ground deformation can be modeled.

ACKNOWLEDGEMENTS

I would like to express my deep gratitude to Prof. Fumiaki KIMATA, my supervisor, for his guidance, support and supervision whilst undertaking this research. From him, I learn so many things especially the volcano behaviour and its ground deformation. I thank him also for introducing many wonderful and beautiful places around Japan and of course Japanese culture and lifestyles.

I am also indebted to Prof. Takeshi SAGIYA, who gave me a lot of invaluable input to improve my research, including at the finalization of my dissertation. My special thanks go to Prof. Makoto MURAKAMI, as a reviewer of this dissertation, who gave me many suggestions that really improve this work. Dr. Takeo ITO, my co-supervisor who gives me the basic knowledge about computer programs, and for being my team mate during field survey in remote Aceh and West Java where we share many interesting things include mie pangsit and soda susu. Should be mentioned: Dr. Taku Ozawa, Dr. Yo Fukushima, Dr. Urs Wegmuller, Dr. Ramon Hanssen, and Dr. Petar Marinkovic from whom I can rely in interferometric matters; Prof. Hasanuddin Z. Abidin and Mr. Yoga Pamitro for sharing useful data during this study; Prof. Joaquim Luis for valuable advices for data format.

I would also like to thank Prof. Koshun YAMAOKA, head of Research Center for Seismology, Volcanology and Disaster Mitigation (RSVD), Nagoya University for his enlightenment through lectures and discussions; and also to all RSVD staffs and members: Watanabe Sensei, Tadokoro Sensei, Yamanaka Sensei, Hashimoto Sensei, Yamazaki Sensei and Nakamichi Sensei, Mrs. Kishiko Mizuno, Mrs. Midori Kanahara and Mrs. Kazuko Kishi for their helps during my time in Nagoya University.

I would like to thank to members of Dynamics and Geophysics Group, which I will not forget the moment when we always meet together in various seminars. My fellow students in dynamics laboratory, Yamazaki-San, Miyata-San, Hashida-San, Endra-San and Rahma-San, Tominaga-San, Ozawa-San, Yamamoto-San, Asahi-San, Hirai-San,

Enrique-San, Duong-San, Ampana-San and other students that cannot be mentioned one by one for their supports.

Special thanks also go to the Dr. Irwan Meilano and Dr. Mohd Effendi, with whom I can share all things and without them I believe I cannot reach this stage of achievement. For Monbukagakusho (MEXT) for providing the scholarships; JAXA for providing ALOS-PALSAR data; and JICA that conducts training course in Seismology, Volcanology and Natural Hazard Disaster Mitigation since 2006 that enable me to interact with many participants from various countries. Also for Iwan Fals, Rendra, Michael Jackson and Laskar Pelangi for sharing their spirits. Not to forget: Yagami Sensei, Okada Sensei and Sano Sensei, teachers at Ikatsu Elementary school; also Kuwahara Sensei, Sano Sensei, Iguchi Sensei and Kato Sensei, teachers at Showa-Sho Hoikuen.

Finally, I would like to thank my lovely wife, Devi Kausar who I depend much and I believe without her I cannot do anything, my sons Almukantar Fikriansyah La Tinulu and Alnair La Patiroi; Ayah Kamba and Mammi Sitti Rahma at Rappocini; Bapak Dr. Kausar Ali Saleh and Ibu Iesye Kausar; Cece, Cici, Atto, Ana, Ria, Bimo, Kiko, Kalel, Irham, Taqif and Amed, all families in Makassar, Bone, Bogor and Jakarta. Thanks for all your support and prayer for us.

TABLE OF CONTENTS

Page

Chapter **Page**

LIST OF FIGURES

LIST OF TABLES

CHAPTER 1

INTRODUCTION

The Earth's shape is changing from time to time, hence the term dynamic Earth. The changes come from external sources such as gravity from other things in solar system; and internal sources mainly from energy transfer by heat convection from the sub-surface. The change itself can be categorized into periodic and un-periodic change. The Earth body tide is one example of the periodic change, whereas land surface deformation is an example for the un-periodic change. Land surface deformation may be related to seismo-tectonic processes such as earthquakes, faulting, volcanism, landslide; anthropogenic processes such as ground water pumping and mining; or other environmental phenomena such as glaciation and deglaciation. Most of these processes are associated with the continental plate movement caused by the mantle convection which can be explained by the theory of plate tectonics (Bervocici, 2003).

By monitoring the displacement continuously through precise positioning and mapping, the rate and the direction of the movement can be determined. Many observation methods and tools are developed to observe ground deformation by monitoring the movement of the objects on the Earth surface, such as volcano deflation and subsidence. Direct observation to the object on the Earth's surface can be performed by utilizing a terrestrial or extra-terrestrial method such as point positioning using theodolite or Global Positioning System (GPS). The GPS technique in general gives precise measurements or provides point-wise information. However it has limitation for

accessing isolated areas. It is also relatively expensive for covering regional area which deals with any spatial density issues.

The Interferometric Synthetic Aperture Radar (InSAR) is an example of indirect observation method, which could complement the limitation of direct observation method as mentioned. As developed based on remote sensing technique, InSAR relies on sensor system and carrier system. For ground deformation studies, spaceborne InSAR system with the sensor being put in space satellite is the most favorable way. However, the general problem with this system is that the temporal resolution is limited by the orbital passages of the satellites over the same area. This implies that InSAR method is an episodic method and impossible to implement as a real-time method, but on the other hand it provides a good spatial coverage or provide more spatially continuous information.

The ability of InSAR to estimate deformation phase is useful to study ground deformation. As mentioned before, ground deformation is related to earthquake (seismogenic) such as coseismic (i.e. Massonnet and Rabaute, 1993) and postseismic deformation (i.e. Burgmann et al., 2000b), volcanic activity (i.e. Palano et al., 2008), landslides, and human activity (anthropogenic) such as land subsidence caused by mining and ground water pumping activities (i.e. Bawden et al., 2001).

Most of the studies listed above were conducted in high latitude region with sub-tropical climate. Since interferogram requires good coherence between images, doing InSAR in low latitude areas is challenging since the land covers change rapidly due to the tropical

climate. In addition, the atmosphere above tropical region usually contains high precipitable water that disturbs the microwave propagation. These conditions are the major problems of InSAR, and therefore it is important to find out the best strategies in InSAR data processing to solve this problem.

On the other hand, there are limited studies of InSAR in low latitude region, especially in Indonesia, a country that is located on the junction of some plate boundaries, namely Eurasian plate, Australian plate, Pacific plate, and Philippine plate; which collided and subducted each other. These tectonic settings have resulted in high seismic activity in Indonesia along the plate boundary and also formed 129 active volcanoes along the volcanic arc located across the country. Ground deformations that occur due to these conditions should be monitored i.e. by using InSAR technique in order to assist in natural hazard mitigation efforts.

This dissertation is based on research that utilizes satellite SAR data. It is expected to contribute to ground deformation studies in Indonesia using InSAR technique. The main objectives of this research are:

1. To investigate the ability of InSAR technique for detecting ground deformation in Indonesia by utilizing L-band SAR data.
2. To find the best strategy in InSAR data processing for detecting ground deformation in Indonesia by utilizing L-band SAR data.
3. To find the suitable method in quantifying the ground deformation estimated from InSAR technique and then model the ground deformation based on InSAR estimates.

This dissertation is composed of six chapters. The introduction and the objectives are included in Chapter 1. An overview of Japan's new SAR satellite system and its data products are described in Chapter 2. In Chapter 3, fundamental concepts of synthetic aperture radar interferometry are introduced focusing on interferogram derivation based on satellite SAR data. A literature review is provided to show the application of InSAR for detecting ground deformation to date.

Chapter 4 discusses the application of InSAR technique in detecting large ground deformation triggered by an earthquake. In this chapter, coseismic deformation on Papua earthquake that occurred on January 3, 2009 is used as a case study. Chapter 5 discusses the application of InSAR technique in detecting small ground deformation related to volcanic activity. In this chapter, ground deformation on Ibu Volcano in Halmahera Island is used as a case study. A linear height dependent atmospheric phase is also discussed briefly as an effort to reduce the atmospheric phase from the interferogram.

Chapter 6 discusses the ability of InSAR to distinguish ground deformation mechanism based on long temporal observation. Ground deformation of Anak Krakatau Volcano is analyzed as a case study. A new technique called *post-processed filtering technique* to improve interpretation of ground deformation derived from InSAR estimates is also explained in this chapter to show the ability of InSAR technique to detect ground deformation in small volcanic island. Finally, Chapter 7 summarizes the research with conclusions and recommendations.

CHAPTER 2

ALOS – PALSAR SYSTEM

Radar operates in the microwave portion of electromagnetic spectrum, and therefore can be distinguished based on the utilized wavelength or band. Figure 2.1 illustrates the electromagnetic spectrum and radar wavelength. For remote sensing purposes, radar sensor is carried either by airplane (airborne) or by satellite (spaceborne). Table 2.1 summarizes satellite SAR system in the world.

Recent spaceborne SAR system is Advanced Land Observing Satellite (ALOS) equipped with Phased Array type L-band Synthetic Aperture Radar (PALSAR) sensor that works on 23.6 cm wavelength. The L-band SAR data has lower sensitivity for vegetation (Ernst et al., 2008) and therefore can obtain information from surface of a highly vegetated area. Based on this advantage, the InSAR is suitable for monitoring ground deformation in tropical region. This chapter summarizes the ALOS platform and the PALSAR sensor and data system.

2.1. An Overview of ALOS Platform

The ALOS system was launched by Japan Aerospace Exploration Agency (JAXA) with an H-IIA rocket from Tanegashima Space Center on January 24th 2006. This satellite system was designed for five missions (EORC, 2008):

(1) Production and renewal of topographical maps on a global scale (spatial data infrastructure),
(2) Support for sustainable development in various parts of the world through regional observations,
(3) Monitoring large-scale disasters around the world,
(4) Surveying of natural resources around the world, and
(5) Development of technologies necessary for future Earth observations.

To achieve these missions, ALOS is equipped with two optical sensors: the Panchromatic Remote-sensing Instrument for Stereo Mapping (PRISM) with 2.5 m resolution, and the Advanced Visible and Near Infrared Radiometer type 2 (AVNIR-2) with 10 m resolution; and one microwave sensor: PALSAR for day-and-night and all-weather land observation with various resolutions. The ALOS data, including calibration and validation of the onboard sensors, is maintained by the Data Utilization System at Earth Observation Research Center (EORC) of JAXA. Figure 2.2 illustrates the ALOS system.

ALOS is set to a sun-synchronous orbit with altitude 691 km and pass a local equator at about 10:30 in ascending direction and 22:30 in descending direction. The temporal resolution, time range that ALOS needs to pass the same location on the Earth's surface is 46 days. For data storage, ALOS is equipped with a 96-GB High-speed Solid-State Recorder (HSSR) which serves all three instruments (Rosenqvist et al., 2007). Data from ALOS are transmitted to ground station in two options: by Data Relay Test Satellite (DRTS) utilizing Ka-band antenna with 240 Mbps; or by direct transmission

(direct down-link) utilizing X-band antenna with 120 Mbps. The characteristics of ALOS are summarized in Table 2.2 (Rosenqvist et al., 2007 and EORC, 2008).

Other important instrument installed in ALOS is Attitude and Orbit Control Subsystem (AOCS) that function to acquire information of satellite attitude and location. This subsystem is comprised of Earth Sensor (ESA), Inertia Reference Unit (IRU), Star Tracker (STT), and GPS Receiver (GPSR), and also has function to keep satellite correct attitude and orbit by driving Reaction Control Subsystem (RCS) gas jet, Reaction Wheel (RW) and Magnetic Torque (MTQ). Especially for GPS receiver installed in ALOS, it can receive two frequencies (L1 and L2) of GPS signals and also can measure a phase of carrier wave of those signals. By utilizing this device, the high accuracy of satellite position and pointing location on Earth's surface can be achieved.

2.2. An Overview of PALSAR System

The PALSAR antenna dimension is 3.1 x 8.9 m that contains 80 transmission and receptions modules on four segments. The off-nadir angle is variable between 9.9^{o} and 50.8^{o} at mid-swath, and therefore the incidence angle also vary between 7.9^{o} – 60^{o} in range. This system is an enhanced version of previous JERS-1 (Japanese Earth Resources Satellite-1) SAR system that operated in 1992 to 1998.

PALSAR that is installed in ALOS is a fully polarimetric instrument and operates in L-band with centre frequency of 1270 MHz. Full polarimetric instrument allows PALSAR to switch from horizontal (H) to vertical (V) polarization and vice versa at respective transmission pulse, enabling four polarizations by double simultaneous polarization

(HH, HV, VH, VV). For examples, HH means the signals are transmitted and received in horizontal direction whereas HV means the signals are transmitted in horizontal direction and received in vertical direction. PALSAR can also simultaneously receive horizontal and vertical polarization per each polarized transmission, which is called multi polarimetry.

PALSAR has four observation modes as follows:

1. *High resolution mode*

The high resolution mode is the most commonly used under regular operation. It can be divided in two different types: Fine Beam Single (FBS) polarization and Fine Beam Dual (FBD) polarization that covers area (swath width) about 70 km. The maximum ground resolution of FBS is 10 x 10 m, whereas doubled for FBD.

2. *ScanSAR mode*

The ScanSAR mode enables to switch off-nadir angle from 3 to 5 times high resolution transmitted beams. It means this mode can cover wide area from 250 km to 350 km squares but the resolution is inferior to high resolution mode that approximately 100 m x 100 m.

3. *Direct downlink*

The direct downlink mode which is also known as direct transmission (DT) mode is operated to accommodate real time data transmission of single polarization. This observation mode is similar to high resolution single polarization mode but has a lower ground resolution of an approximate 20 m x 10 m.

4. Polarimetric mode

The polarimetric observation mode enables PALSAR to simultaneously receive horizontal and vertical polarization for each polarized transmission. In this observation mode, PALSAR also enables to switch from horizontal to vertical at respective transmission pulse that provides full Quad-Pol (HH/HV/VH/VV) scattering matrix with 12 alternative off-nadir angles between 9.7^{o} and 26.2^{o}. This observation mode has 30 x 10 m ground resolution for 30 km swath width.

The characteristics of PALSAR are illustrated in Figure 2.3 and summarized in Table 2.3 (Rosenqvist et al., 2007 and EORC, 2008).

2.3. PALSAR Data Products

There are five levels of PALSAR standard products; called Level 1.0, Level 1.1, Level 1.5, Level 4.1 and Level 4.2 (see tabulation in Table 2.4). This classification is based on processing grade and observation mode.

The Level 1.0 is unprocessed signal data or just a reconstruction from raw data appended with radiometric and geometric correction coefficients. The product is not yet subjected to the recovery process of SAR. Data type is in 8-bit unsigned integer and available in separate files for each polarization.

Level 1.1 is a complex data (SLC) and equally spaced on slant range compressed in range and azimuth directions. This product is SAR recovery processing of Level 1.0

data. Data type is in IEEE 32-bit floating point and available in separate files for each polarization.

Level 1.5 is multi-look processed image in determined projection map coordinates. There are two options for Level 1.5, systematically geocoded or systematically georeferenced. Geocoded data represents image that is converted into spatial data that can be displayed as a map, whereas the georeferenced data represents image that is aligned to a known coordinate system. The data is equally spaced on ground range. Data type is in 16-bit unsigned integer and available in separate files for each polarization.

Level 4.1 data product is special for polarimetry observation mode produced after processing Level 1.0 of dual or quad polarizations. The data is equally spaced on slant range and ground range. Data type is in 16-bit integer (signed and unsigned), and available in separate files for each polarization.

Level 4.2 data product is special for ScanSAR observation mode produced after processing Level 1.0 of single polarization. The data is equally spaced on ground range. Data type is in 16-bit unsigned integer and available in separate files for each polarization.

CHAPTER 3

SYNTHETIC APERTURE RADAR INTERFEROMETRY

The InSAR comes from the combination of the interferometry technique and radar (Radio Detection and Ranging) image. It emerges as a powerful technique in mapping Earth surface. This chapter will describe shortly of SAR, InSAR, and DInSAR based on satellite system.

3.1. Synthetic Aperture Radar (SAR)

Synthetic Aperture Radar (SAR) is a coherent radar system that generates high resolution remote sensing imagery that can work day and night because it is an active system. It can be used in all weather condition because it uses microwaves to observe Earth's surface or other planet observation (Elachi, 1982; Roth and Wall, 1995). This system was invented in 1953 by Carl Wiley and then was developed for fine resolution mapping and other remote sensing applications. As a part of remote sensing technique, this system needs a carrier to install the equipments, therefore the term airborne and spaceborne (satellite) SAR are introduced. In this research, only data from spaceborne SAR system is utilized.

Figure 3.1 briefly illustrates the geometric configuration of satellite SAR system. The basic concept of SAR had been explained in many references such as Franceschetti and

Lanari (1999); Elachi (1988); Curlander and McDonough (1991). These references explained the geometry of SAR and its mathematical function.

As an active system, radar antenna transmits energy (signals) with microwave frequencies to illuminate targets in the surface. The reflected signals that were received on the radar antenna represent the characteristics of the targets (scatterers) in electrical and geometrical properties. By precisely measuring the time difference between the transmitted pulse and the receipt of the reflected energy, the range between radar sensor and the reflecting object can be determined and known as slant range. Moreover, through digital data processing, the reflected signals (raw radar data) can be transformed to SAR image. There are four main steps required in SAR data processing, they are:

1. Parameter calculation.

   The Committee on Earth Observing System (CEOS) has established a standardization of SAR data structures which is known as CEOS format. SAR data in CEOS data format is composed by five files: volume directory file, leader file, image file, trailer file, and null volume directory file. In parameter calculation step, processing parameters are determined by extracting from the CEOS leader files and extracted from raw data. The parameters include the observation starting time, Earth's geometry parameters, scene's geometry parameters, track angle, platform altitude, pulse repetition frequency (PRF), and data properties.

2. Doppler center frequency estimation

   Since there are motions of sensor and targets during the processes of transmitting and receiving signals, the frequency is shifting, which is caused

by a Doppler effect. To eliminate this effect, the Doppler centroid (zero Doppler) frequency estimation is performed in SAR data processing. The Doppler centroid varies with both range and azimuth. The variation with range depends on the particular satellite attitude and how closely the illuminated footprint on the ground follows an iso-Doppler line on the ground, as a function of range. The variation in azimuth is due to relatively slow changes in satellite attitude as a function of time. There exist a number of algorithms to estimate the Doppler centroid frequency, for example multi-look cross correlation (MLCC) algorithm and multi-look beat frequency algorithm (MLBF) algorithm by Wong et al. (1996).

3. Range compression

The resolution in slant range direction in SAR system depends on the transmitted pulse width (τ) and can be defined as the minimum distance between two reflecting points along the look direction at the range at which the points could be sensed as separate and distinct.

$$\Delta R = \frac{c.\tau}{2} = \frac{c}{2.\Delta f} \tag{3.1}$$

$$\Delta x = \frac{c.\tau}{2.\sin\theta} \tag{3.2}$$

where ΔR is slant range resolution, c is speed of light, Δf is frequency changes in chirp modulation, Δx is ground resolution, and θ is the incident angle. Smaller pulse width gives higher resolution but need more power. To deal this problem, a technique called chirp modulation is developed to compress the transmitted pulse width. In range compression step, a filter to match the transmitted pulse with the recorded data is applied. This process is

used to recover the complex reflectivity of the surface convolved with the chirp.

4. Azimuth compression

   Resolution in azimuth direction can be written as:

$$\Delta Az_{RAR} = \frac{\lambda . R}{L} \tag{3.3}$$

$$\Delta Az_{SAR} = \frac{L}{2} \tag{3.4}$$

   where ΔAz_{RAR} is the along track resolution (azimuth direction) of real aperture system (without azimuth compression) whereas ΔAz_{SAR} is the resolution of azimuth direction in synthetic aperture system (with azimuth compression or based on Doppler effect), λ is radar wavelength, R is the distance between radar sensor and target, and L is the antenna length. It is shown that the resolution in azimuth direction is SAR system depends on the physical antenna size. Azimuth compression is the last important step in SAR data processing. This step is to focus the data in azimuth by considering the phase shift of the target as it moves through the aperture, and therefore the orbital parameter of the sensor is needed. Relative calibration of the antenna pattern in range, the variation in slant range, and the variation in length of the azimuth reference function are also executed in this step.

It can be concluded that by compressing transmitted pulse (chirp compression) in range and azimuth directions, the ground resolution of SAR system is improved. The final output of SAR data processing is SAR image that can be seen as a mosaic of small picture elements (pixels). Each pixel corresponds to a small area of the Earth's surface

that can be defined as a resolution cell. Each pixel contains a complex number that carries amplitude and phase information about the microwave field backscattered by all objects in corresponding resolution cell projected on the ground. These kinds of information are stored in complex format by adapting IQ (In-phase and Quadrature) data format as illustrated in Figure 3.2. Therefore, SAR image also known as single look complex (SLC) that is composed of a regular grid with complex values or phasors (Hanssen, 2001) and can be decomposed into amplitude (A) or real (R) and phase (ϕ) or imaginer (I) components as expressed in following equation:

$$y = A.e^{i\phi} \tag{3.5}$$

where: y is the SLC data that represents the electric field of a plane electromagnetic wave , A is amplitude of the electromagnetic pulse, and ϕ is phase angle. The amplitude represents the quantity of electromagnetic field scattered back grouped in each SAR image-sampling cell or pixel, whereas the phase represents an ambiguous measure of distance between sensor and each area on the ground corresponding to an image pixel (Raucoules et al., 2007).

3.2. Interferometric Synthetic Aperture Radar (InSAR)

SAR interferometry or InSAR is developed to derive topographic map for one particular area or topographic height for one particular point in Earth's surface. The product of this technique is an interferogram which is obtained by cross-multiplying, pixel by pixel, of two SAR image (two SLCs) and then a digital elevation model (DEM) that represents the Earth's topography can be derived. Figure 3.3 illustrates the InSAR geometry.

The first SAR image is called master and the second one slave. As a result, the interferogram amplitude is the amplitude of master image multiplied by that of slave image, whereas the interferometric phase is the phase difference between the images.

$$Interferogram = y(master) * y(slave) \tag{3.6}$$

$$Interferogram = A_M A_S e^{i(\phi_M - \phi_S)} \tag{3.7}$$

$$\phi_G = \phi_M - \phi_S = \tan^{-1}\left(\frac{I}{R}\right) = -\frac{4\pi(R_M - R_S)}{\lambda} \tag{3.8}$$

where ϕ_G is the interferometric phase or phase difference derived from master and slave images in one point, R_M and R_S are the geometric distances of satellite to target both acquisition times, and λ is the SAR system wavelength.

Since there are two different observation times, the orbit of the satellite is not exactly the same for the two images. The distance between the two satellite positions is known as the baseline (B), and can be decomposed into parallel baseline ($B_{\parallel}$) and perpendicular baseline ($B_{\perp}$). The parallel baseline is the component along the radar's line of sight whereas the perpendicular baseline is the component which is perpendicular to the line of sight. The satellites position and altitude when they observe the Earth's surface are required to calculate the baseline. This information is stored in satellite ephemeris or orbit file.

Based on Figure 3.3, the height of one point (G) in Earth's surface (H_G) above reference surface and the phase difference ($\partial\phi$) can be defined by following formulas (Hanssen, 2001):

$$H_G = \frac{\lambda R_M Sin(\theta_G^0)}{4\pi B_{\perp,G}^0}\partial\phi \tag{3.9}$$

$$B_{\perp,G}^0 = B\cos(\theta_G^0 - \alpha) \tag{3.10}$$

where: θ_G^0 is look angle in point (G) and α is angle of satellite baseline.

The $\partial\phi$ in Equation (3.9) can be replaced by 2π and gives the height ambiguity (h_a) that can be defined as the altitude difference that generates an interferometric phase change of 2π after interferogram flattening. Height ambiguity is related to the orbital separation between image acquisitions and equals the size of elevation change that would produce one fringe.

$$h_a = \frac{\lambda R_M Sin(\theta_G^0)}{2B_{\perp,G}^0} \tag{3.11}$$

A fringe is a line of equal phase in the interferogram and depends on baseline parameters. The parallel baseline ($B_{\parallel}$) generates systematic fringes whereas the perpendicular baseline ($B_{\perp}$) constructs topographic fringes. The interferometric fringes do not directly represent the surface height or altitude since it is wrapped in modulo 2π, therefore the unwrapping process is needed to obtain the correct number of whole phase cycles and scale them by height ambiguity value. In addition, the interferogram also contains phase changes caused by atmospheric heterogeneity and decorrelation sources which occur between acquisitions times.

3.3. Differential Interferometric Synthetic Aperture Radar (DInSAR)

The interferometric phase contains information of the topographic profiles (ϕ_{topo}), difference in orbital trajectory (ϕ_{orb}), possible deformation (ϕ_{defo}), atmospheric artifacts (ϕ_{atm}) and phase noise (ϕ_{noise}) and can be rewritten as:

$$\phi_G = \phi_{curv} + \phi_{topo} + \phi_{orb} + \phi_{defo} + \phi_{atm} + \phi_{noise} \tag{3.12}$$

$$\phi_G = \frac{4\pi}{\lambda} B \sin(\theta_G^0 - \alpha) + \frac{4\pi H_G B_{\perp,G}^0}{\lambda R_M \sin(\theta_G^0)} + \frac{4\pi}{\lambda} B_{\parallel} + \frac{4\pi}{\lambda} D_G + \phi_{atm} + \phi_{noise} \tag{3.13}$$

where D_G is the surface displacement in the direction between the satellite and ground pixel.

Therefore it is possible to estimate the deformation related to point displacement in the Earth's surface based on InSAR technique by removing other unwanted signals.

$$\phi_{defo} = \phi_G - \left\{ \frac{4\pi}{\lambda} B \sin(\theta_G^0 - \alpha) + \frac{4\pi H_G B_{\perp,G}^0}{\lambda R_M \sin(\theta_G^0)} + \frac{4\pi}{\lambda} B_{\parallel} + \phi_{atm} + \phi_{noise} \right\} \tag{3.14}$$

For ground deformation detection, the term differential InSAR (DInSAR) is introduced to subtract the topographic phase from the interferogram. The topographic phase can be derived from the following, i.e. a simulation of an existing DEM obtained from a topographic map; other survey techniques; or from the Shuttle Radar Topography Mission (SRTM). This kind of technique is known as 2-pass differential interferometry or simply DInSAR because it only needs two SAR images. The technique performs differentiation between real interferogram obtained from two SAR images and simulates interferogram derived from a DEM.

Other techniques are 3-pass and 4-pass differential interferometry. Three-pass differential interferometry is based on three SAR images to derived two interferogram based on the same reference (same master image). One of the pairs with a short acquisition time interval and rather large interferometric baseline not affected by deformation is used to estimate the topographic phase (topography pair). The other pair has to consist of one image before and after the deformation occur (deformation pair). The advantage of 3-pass differential interferometry is the same geometric condition since both topography and deformation pairs have the same master scene. Another advantage is that this strategy does not require a DEM.

Four-pass differential interferometry technique requires four SAR images to derive two independent interferograms (different reference or different master image). The two independent interferograms are then differentiated with each other. The difference with respect to 3-pass differential interferometry is that a pair of images independent from the differential pair is used for the generation of the topographic phase. Therefore resampling of the two interferograms is required to conform the geometry.

The generation of full resolution interferogram and then deformation signals requires following steps (expressed as differential InSAR processing chain in Figure 3.4):

1. ***Initial estimation***

   This step estimates the initial offset between two SAR images before cross-multiplying pixel by pixel.

2. Image registration and resampling

Image registration or co-registration step is a fundamental process in interferogram generation since this step ensures that each targeted object on the ground contributes to same pixel in both the master and slave image. Co-registration consists of computation offsets between master and slave image which are used to solve the transformation parameters to bring the slave image geometry identical with master image geometry. Once the transformation parameters are known, then the slave image is resampled to conform its geometry to master image in sub-pixel resolution. Appropriate interpolation methods are used to minimize interpolation errors.

3. Baseline estimation

The measurement of the distance between the two satellites when they observe the same target on the Earth's surface requires accurate satellites position and their attitude. This information is stored in satellite ephemeris or orbit file. In practice, the baseline can be estimated using:

① Orbital information, based on the state vector of the satellite obtained from the orbital file. This method works fine when accurate state vectors (orbit file) are available.

② Fringe rate of the interferogram, based on the local fringe rate in the unflattened interferogram. This method works fine when the fringes due to the Earth's curvature are dominant in the interferogram.

③ Ground control points, based on the inversion of the unwrapped phase to height. This method is the most accurate, however it can only be performed after unwrapping step and therefore this method is utilized to refine the baseline estimation as explained later in step 10.

4. ***Range spectral shift and azimuth common bandwidth filtering***

   This step allows the phase co-registration between images due to spectral shift in range and azimuth direction that may occur after registration and resampling image.

5. ***Interferometric phase computation***

   This step is the main process of InSAR technique. The interferogram is derived by pixel-to-pixel computation of two co-registered and spectral-shift-filtered images.

6. ***Generation of synthetic fringes (topographic phase)***

   This step can be said as an external process if 2-pass DInSAR strategy is selected. The topographic phase is simulated based on baseline information derived from orbital parameter of master and slave data. By utilizing the same orbital parameter, the simulated topographic phase will give the same pattern with the real interferometric phase that contains the topographic fringes. There are three methods to estimate the baseline: inversion from the parameters of satellite orbit, inversion from visible fringes, and inversion by least square method on the basis of ground control points. The important factor in this step if external DEM is utilized is the coordinate system. Since most of the interferogram processing is conducted in SAR coordinate system, therefore the external DEM which is usually in geo-referenced map coordinate system, should be transformed to SAR coordinate system. This step is not required if 3-pass or 4-pass DInSAR strategy is selected since the topographic phase is generated within the same coordinate system.

7. ***Subtracting topographic phase from the interferometric phase***

   This step is to remove the topographic phase from the interferometric phase to leave only deformation (differential) phase and other signals such as atmospheric phase and systematic orbital phase that may remain.

8. Differential phase filtering

Filtering the differential interferogram aims to reduce phase noise to make the phase unwrapping more efficient and simpler. In this step, there are three options to filter the interferogram: band pass filter, based on local phase gradient filter, and adaptive filter based on local fringe spectrum.

9. Unwrap the differential phase

The differential phase is still wrapped in modulo 2π , therefore this step aims to recover the integer number of cycles to be added to the wrapped phase so that the unambiguous phase value for each image pixel can be obtained.

10. Baseline refinement

The precise baseline estimates can be obtained by utilizing the topographic phase information (the second term in Equation 3.13). By knowing height information (from DEM) and the unwrapped topographic phase (from InSAR), then inversely the baseline can be estimated. The height information is used as ground control point (GCP). These GCPs are systemically distributed across the image and are utilized to estimate the baseline parameters using least square approach.

11. Mitigation of Atmospheric Component

The differential interferogram typically still contains an atmospheric phase component which can severely generate ‘pseudo’ deformation pattern. The atmospheric phase can be mitigated by estimating linear phase trend with elevation (modeling height dependent atmospheric phase) and by stacking the interferogram if there are a lot of interferogram derived in long term observation.

12. Deformation map generation

The final unwrapped differential phase is used to generate surface displacement map. This step calculates the displacement along the SAR look vector by utilizing the information of wavelength, incidence angle and slant range in near edge and far edge. Positive value of displacement along the look vector is interpreted as the displacement towards the sensor (satellite). In addition, the positive value means there is increasing surface height if projected to vertical component, or decreasing ground range if projected to horizontal component and vice versa.

3.4. InSAR and Ground Deformation Detection

The ability of InSAR to estimate deformation phase is useful to study ground deformation. As mentioned in Chapter 1, ground deformation is related to earthquake (seismogenic) such as coseismic and postseismic deformation, volcanic activity, landslides, and human activity (anthropogenic) such as land subsidence caused by mining and ground water pumping activities.

To detect coseismic deformation due to an earthquake, the interferogram must be formed from two SAR images that cover before and after the earthquake. Massonnet and Rabaute (1993) formed the first interferogram of Landers Earthquake, California that occurred in June 28, 1992. Since then, InSAR technique was used widely in characterizing the coseismic deformation field resulted from earthquakes, fault geometry, and slip distribution (Delouis et al., 2002; Feigl et al., 2002). This technique is also potential to be used in postseismic deformation and relaxation, and interseismic creep because of its ability to measure centimeter-scale changes in deformation over

time spans of days to years that had been studied i.e. by Burgmann et al. (2000a); Arnadottir et al. (2005); Cakir et al. (2005). Tobita et al. (1998) detected a significant postseismic deformation after 1995 earthquake in North Sakhalin Island, Russia, by processing the L-band JERS system.

Ground deformation related to volcanic activity is usually indicated by inflation and deflation pattern that can be identified by concentric fringes in the interferogram. For example, the deflation induced by the activation of Etna Volcano, Italy, had been measured using InSAR technique by Massonnet et al. (1995); the deformation field detection associated to the 1997 eruption of Okmok Volcano in Alaska by Lu et al. (1998); and modeling magma intrusions and edifice radial spreading after eruption during magma recharging phase was conducted by Palano et al. (2008).

For natural hazards warning such as high potential landsliding areas, InSAR technique is useful to identify the steep and rough topography. By combining with other parameters especially rainfall data and geological map, areas that prone to landslides can be mapped. Colesanti et al. (2003) have shown the application of InSAR to monitor landslides and tectonic motion.

Other phenomenon in ground deformation is land subsidence and uplift. Land subsidence is generally related to geological subsidence i.e. sediment consolidation due to its own weight and tectonic movements; or related to human activities such as withdrawal of ground water and geothermal fluid, oil and gas extraction from underground reservoirs, and collapse of underground mines. The amount of subsidence

or uplift can be estimated from the number of concentric fringes that appear in the interferogram. Carnec et al. (1996) detected subsidence related to underground coal mining near Gardanne, France, by using InSAR. Bawden et al. (2001) sensed the seasonal fluctuations of Santa Ana Basin, California, i.e. uplift due to ground water recharge during the wet winter season and subsidence due to groundwater withdrawal during the dry summer season.

However, as mentioned in Chapter 1, InSAR technique has limitations in temporal resolution, coherence, and noise related to decorrelation. Usually, longer time difference between observation epochs decreases the coherence of interferogram image's. The coherence is the cross-correlation coefficient of SAR image pair estimated over a small window. The coherence value ranges from 0, which represents the interferometric phase is just noise; to 1, which represents the complete absence of phase noise.

Detecting ground deformation based on InSAR technique, there are various different ways to produce a differential interferogram:

1. ***Single interferometric pair and near-zero baseline***

   Differential interferogram phase is derived from two SAR images (SLCs) and small (near zero) perpendicular baseline of satellite orbit.

2. ***Single interferometric pair and non-zero baseline***

   In the case the non-zero perpendicular baseline, the interferometric phase derived from two SAR images (SLCs) contains both altitude (topographic phase) and deformation. In this case, 2-pass DInSAR strategy should be applied.

3. ***Three interferometric images and no motion***

   This case is identical with 3-pass DInSAR that is explained in Section 3.3. The shortest temporal difference (to gain coherence and avoid terrain motion or deformation) with larger baseline should be selected as the first interferometric pair that represents the topographic phase. The second pair should have a larger temporal difference but a small baseline.

4. ***Two image pairs and no motion in one of them***

   This case is identical with 4-pass DInSAR that is explained in Section 3.3. This strategy has two master images and each of them has a slave image. The processing steps are the same with 3-pass DInSAR strategy.

Related to ground deformation detection, InSAR estimates only give one-dimensional information along line of sight (LOS) direction. After unwrapping the differential phase as a result of DInSAR data processing, LOS deformation can be decomposed to vertical and horizontal component along the LOS direction. Filtering method can also be applied to reduce noise and to improve homogeneity of pixel value on this stage. This is called post-processed filtering technique. By analyzing these differential phase, ground deformation based on InSAR estimates can be derived.

CHAPTER 4

LARGE GROUND DEFORMATION DETECTED BY INSAR

This chapter discussed application of InSAR in detecting large ground deformation triggered by an earthquake in Indonesia. Large coseismic deformation caused by Papua earthquake that occurred on January 3, 2009 was detected through processing ALOS PALSAR data.

4.1. An Overview of Study Area

The New Guinea Island is the second largest island in the world with the western part of this island belongs to Indonesia and known as Papua Province (previously known as Irian Jaya Province), whereas the eastern part belongs to Papua New Guinea. This island was formed on the northern edge of the Australian continental plate as a result of Pacific plate' subduction beneath. The eastern part of Indonesia is characterized by complex tectonics in which motions of numerous small plates are accommodating large-scale convergence between the Australia, Pacific, and Eurasia plates.

The tectonic setting around this island is oblique convergence between oceanic Pacific plate and the margin of continental Australia plate. The Pacific plate lithosphere is subducting beneath Australia plate lithosphere. The motion of Pacific plate (located north and northeast of the island) relative to Australia plate (located south of the island) is predicted by NUVEL-1 (DeMets et al., 1990) to be at azimuth of 248^{o} (south-west

direction) and rate of 110 mm per year across Papua. Evidence of this collision is the Highlands thrust belt, a 1000-km-long, 4-km-high, east-west trending mountain belt which covers much of the island. Abers and McCaffrey (1988) estimated that the Highlands thrust belt accounts for only 5 – 20% of the total convergence. The subduction zone along the northwest coast of New Guinea is characterized by an offshore oceanic trench, that is known as the New Guinea trench and Manokwari through on the northern part of New Guinea Island that partially accommodate the Pacific-Australia convergence as can be seen in Figure 4.1.

Puntodewo et al. (1994) had studied the crustal deformation and tectonic setting of this region and found that the oblique convergence between the Pacific and Australian plates was accommodated in two very different ways between eastern and western part of Biak Island. The eastern part was accommodated by Memberamo Thrust Belts and the New Guinea Trench, whereas the western part was accommodated largely by rapid westward motion of Bird's Head region relative to Australia and some thrusting fault of the Pacific beneath the New Guinea Trench and Manokwari Trough.

On January 3, 2009, at 19:43 UTC a Mw7.6 earthquake occurred about 10 km north of Bird’s Head area, near the New Guinea trench (Figure 4.1). This earthquake killed at least four and injuring dozens of people. The epicenter was located approximately at 0.408°S, 132.886°E or 150 kilometers west-northwest of Manokwari and about 170 km east-northeast of Sorong, on the Bird's Head Peninsula. This earthquake occurred about 470 km west of the magnitude 8.2 earthquake of February 17, 1996 which was known as Biak Tsunami earthquake 1996 that killed at least 108 people. In order to detect

ground deformation related to January 3, 2009 earthquake, PALSAR data was processed based on InSAR technique.

4.2. Data and Processing Method

Two ascending PALSAR data in fine resolution double polarimetry (FBD) observation mode with Level 1.1 were obtained from Japan Aerospace Exploration Agency (JAXA) through the ALOS User Interface Gateway (AIUG) under a collaborative volcano research project. These data was processed to obtain interferogram and then deformation phase signals using GAMMA SAR Software (Wegmuller and Werner, 1997).

The data observed on October 14, 2008 was set as master, whereas the one observed on January 14, 2009 was set as slave. It means the temporal baseline is 92 days, or 81 days before and 11 days after the earthquake. The image parameters and properties were tabulated in Table 4.1. With this condition, the co-seismic deformation should be detected based on InSAR technique.

Initial estimation of perpendicular baseline was calculated based on satellite orbital information utilizing Equation (3.10). It was found that the baseline was approximately 1 m, hence the single interferometric pair and near-zero baseline data processing strategy was applied.

Since data was obtained in Level 1.1, therefore the initial step was to convert the data from CEOS format directly to SLC format based on the information contained in leader

file. The dimension of SLC data was 9280 samples in range direction and 18432 samples in azimuth direction. The range pixel spacing was approximately 4.6 m, and 3.2 m for the azimuth pixel spacing. Further, co-registration and resampling of slave image to master image to conform the geometry were performed. Then phase co-registration by the range spectral shift and the azimuth common bandwidth filtering. It was found that the co-registration of the two images was 0.1. This indicated the geometry of both images was conformed in sub-pixel accuracy. This information ensured the high level of interferometric correlation.

The interferogram was derived after the data was looked down into 4 and 6 in range and azimuth direction respectively. Hence, the interferogram dimension was 2320 in range (width) and 3072 in azimuth (interferogram azimuth lines). The interferogram pixel spacing was 19 m in range and 19 m in azimuth. The Earth's curvature interferogram was removed based on the first term of Equation (3.13) and can be seen in Figure 4.2. Since the perpendicular baseline was small, this flattened interferogram thus contained the deformation quantity in wrapped phase.

4.3. Results

To obtain ground deformation based on InSAR estimates, the 2π wrapped phase as shown in color fringes should be unwrapped. However, before unwrapping the phase, it is important to improve fringe visibility and reduce phase noise. For this purpose, an adaptive interferogram filtering algorithm (Goldstein and Werner, 1998) was applied to the flattening image. The PALSAR observation area was covered by high dense

vegetation or forest canopy, therefore the phase noise was in high level (Zebker and Villasenor, 1992).

To deal with this condition, the adaptive interferogram filtering was applied by setting a large rectangular patch (window) sizes and high values of exponential power spectrum filter parameter. Referring to adaptive interferogram filtering algorithm, this study found that 256 x 256 patch size and 1.0 filter parameter improved fringe visibility significantly. The result is illustrated in Figure 4.3.

Phase unwrapping was performed to retrieve the displacement information and true ground range by adding the correct integer multiple of 2π to the interferometric fringes. In this study, minimum cost flow (MCF) algorithm (Costantini, 1998) was used to deal with low coherence area due to layover and shadowing area caused by rough terrain.

Figure 4.4 illustrates the unwrapped deformation phase. This information was then converted to displacement by considering the wavelength and the incidence angle. To obtain the displacement in map coordinates, geocoding process should be conducted. This means the transformation from SAR coordinate system to a selected map coordinate system. In the conventional way, one cycle of color represents half of wavelength of path difference. For example, for L-band SAR data, one color cycle of differential phase represents 11.8 cm displacement along the line of sight (LOS) relative to reference point.

The geo-referenced displacement map could then be analyzed and used to derive the earthquake source mechanism. InSAR estimates only give one-dimensional information along line of sight direction. However, the line of sight deformation can be decomposed to vertical and horizontal component along its direction. Since vertical component is identical with one dimension, deformation derived from InSAR estimates can be analyzed by converting into vertical component. Moreover, by assuming the master image as the reference height, the vertical component of line of sight displacement can be analyzed easily. The conversion of the line of sight displacement to vertical component displacement can be expressed as:

$$V_{disp} = \left(\frac{LOS}{\cos\theta} \right) \tag{4.1}$$

where V_{disp} is displacement in vertical component, LOS is displacement information obtained after unwrapping process and θ is the incidence angle (illustrated in Figure 4.5).

The coseismic deformation of Mw 7.6 January 3, 2009 Papua earthquake derived from InSAR estimates found that vertical displacements were 50 cm uplift and 30 cm subsidence. The maximum uplift was located in the coastal area near the epicenter location, whereas the subsidence was located in the southern part of the coast and created a clear concentric pattern. The vertical displacement map is showed in Figure 4.5.

The InSAR estimates vertical displacement can be used to estimate the fault parameter of the Papua Earthquake. Firstly, the vertical component displacement is converted to grid format to make the estimation process more convenient. Then, based on vertical

displacement pattern of InSAR estimates, various fault models were derived based on Okada solution (Okada, 1992). These fault models then were simulated to derive vertical displacement. One line (illustrated as line AB in Figure 46) was then created to extract the vertical deformation (profile) values from InSAR estimates and generated models.

The InSAR vertical profile estimate is used to constrain the fault parameters. The best model is selected by fitting the extracted vertical displacement from InSAR estimates and fault parameter model candidates. The best fault model which fit to InSAR estimates has the following parameter:

- Fault dimension is 72 km in length and 28 km width,
- Dip angle is approximately 14^o
- Depth is approximately 13 km
- Dislocation geometry: strike slip, rake, maximum slip are 107^o, 90^o and 2.5m respectively

Based on these fault parameters, the moment magnitude (Mw) is calculated based on Kanamori (1977); Hanks and Kanamori (1979) with formulas as follows:

$$M_W = \frac{2}{3}\log_{10} M_0 - 10.7 \tag{4.2}$$

$$M_0 = \mu LWu \tag{4.3}$$

where: M_W is moment magnitude, M_0 is seismic moment, μ is the shear modulus of the rocks involved in the earthquake, which is typically 30 Gigapascals (Aki and Richards, 2002), L is the length dimension of fault rupture geometry, W is the width

dimension of fault rupture geometry, and u is the average displacement (slip) on rupture area.

Based on InSAR estimate, moment magnitude for January 3 2009 Papua Earthquake is 7.4. This result is smaller compared to the result that was derived from waveform analysis such as Mw 7.6 by Yamanaka (2009) and Hayes (2009). The discrepancy (tabulated in Table 4.2) is because of the limitation of InSAR itself that estimates ground deformation only in line of sight direction. In addition, the area coverage that is analyzed is based on one scene of PALSAR image that is approximately 70 km^2 hence the fault dimension is constrained based on the displacement on this area only. Figure 4.6 illustrates the comparison of vertical displacement profile derived from InSAR estimates and other models.

Based on InSAR deformation signals, this earthquake shows evidence of North-South compression prior to the January 3, 2009 earthquake. This earthquake is located between Manokwari Trough and Sorong Fault, which is controlled by North-South tectonic compression. It was a result of thrust faulting on a plate-boundary along the northwest coast of the island of New Guinea.

CHAPTER 5

SMALL GROUND DEFORMATION RELATED TO VOLCANIC ACTIVITY DETECTED BY INSAR

Small ground deformation in the vicinity of the volcano that is related to subsurface magma activity can be identified by InSAR technique. Beside cloud cover, high density of vegetation, which is common in rain forests, is also a major obstacle for studying ground deformation in Indonesia. Therefore a longer wavelength such as L-band radar data is suitable to address these problems. This chapter describes the advantages of InSAR technique by processing PALSAR data and the application of post-processed filtering in detecting small ground deformation. As a study case, Ibu Volcano in Halmahera Island, Indonesia, was selected.

5.1. Introduction

To understand the status of a volcano, a complete volcano monitoring system comprises seismic observation, geodetic observation and geochemical observation (Dzurisin, 2007) is required. This observation system is useful to prepare mitigation efforts in order to face the volcanic hazards such as:

1. Ash falls that can make dark clouds and cover the land;
2. Ash flowing through the river valley and is related to pyroclastic flow;
3. Mudflows or lahars;
4. Volcanic landslides or debris avalanche;
5. Volcanic tsunamis;

6. Lava flows that can reach an average velocity of 30 km/hr; and
7. Volcanic gases such as carbon dioxide (CO_2), sulphate (SO_4), Hydrogen sulfide (H_2S), and Hydrogen fluoride (HF)

Especially for volcano eruption, the International Association of Volcanology and Chemistry of the Earth Interior (IAVCEI) has standardized the five groups of the eruptive characteristics as follows:

1. The vent location that classify the origin of eruption location into central crater eruption, flank vent eruption, radial fissure eruption, and regional fissure eruption.
2. Interaction with water that distinguish the eruption into submarine eruption, new island formation eruption, sub-glacial eruption, and crater lake eruption.
3. Tephra-related processes that classify the eruption into explosive eruption, pyroclastic flows eruption, phreatic explosions, and fumarolic activity.
4. Lava extrusion process that can be classified into lava flows, lava lake eruption, dome extrusion, and spine extrusion.
5. The impact of eruptions on humans that is recognized into fatalities, damage, mudflows (lahars), and tsunami.

The seismic observation is designed to monitor the volcanic activity beneath the surface; geodetic observation to detect deformation on the surface; and geochemical observation to monitor the chemical substance properties that emerge to the surface and the atmosphere. However, a complete volcano monitoring system requires a lot of expenses, and this is a common problem in developing countries such as Indonesia. Therefore, InSAR as a part of remote sensing technique that has advantages in regional

scale observation is an alternative choice to complement the volcano deformation monitoring.

Ibu Volcano with 1340 m height is located in Halmahera Island, North Moluccas, Indonesia. The approximation coordinate is 1.475°N and 127.642°E as illustrated in Figure 5.1. This volcano has not been much studied yet, and monitored by only one seismometer installed at 1.5 km western side of the summit (crater) on the altitude of 782 m. This observation was designed to record the deep (A-type) and shallow (B-type) volcanic earthquake (Minakami, 1960).

The volcano erupted in 1911, 1998, 2001, and 2004. Volcanic activities have increased since January 2008 and Ibu once again erupted on March, 18 2008. The eruption was classified as phreatomagmatic type which was recognized from the volcanic ash.

5.2. Data Sets

This study utilized six ascending Level 1.1 PALSAR images which were observed on August 2007, October 2007, January 2008, February 2008, April 2008 and July 2008 with common data properties summarized in Table 5.1. These PALSAR data were obtained from Japan Aerospace Exploration Agency (JAXA) through the ALOS User Interface Gateway (AIUG) under a collaborative volcano research project. These data was processed to obtain interferogram and then deformation phase signals using GAMMA SAR Software (Wegmuller and Werner, 1997).

5.3. Data Processing Strategies

Data processing steps are started by converting PALSAR Level 1.1 products from CEOS format into software processing (GAMMA SAR) format by considering radiometric calibration factor. Table 5.1 shows that there are two different data based on observation modes, FBS (28 MHz, high bandwidth) and FBD (14 MHz, low bandwidth) observation mode. These kinds of data have different dimension in range direction. Methods that have been developed to derive an interferogram from FBS and FBD observation mode can be classified into two different approaches, in example:

1. Interpolation method (Sandwell et al., 2008). This method is based on interpolation algorithm to convert the raw waveform data between FBD (14 MHz) and FBS (28 MHz) modes. This conversion approach is to Fourier transform each complex radar echo and double the length of the array in the frequency domain. This algorithm provides a smooth interpolation yet retains the complex value of the original FBD data at every other data point.
2. Oversampling method (Werner et al., 2007). This method is based on resampling algorithm for SLC data in range direction. This method works fine in situations where a range spectrum shift has occurred due to high deskew. This method is performed using Fast Fourier Transform (FFT) combined with a bandpass filter centered on the range frequency centroid. The range pixel spacing and the number of range pixels in output SLC image parameter file are adjusted for the range oversampling factor that has been inputted.

Since both methods give the same result (Sandwell et al., 2008), this study utilized the oversampling method by applying oversampling factors 2 in range direction. Up to this step, the results are the SLC images for six observation epoch. Since this study only focuses on Ibu Volcano region, therefore the SLC data were cropped to area around Ibu Volcano as illustrated in the bottom part of Figure 5.1.

There were five interferograms formed based on a sequence observation with a short temporal baseline as tabulated in Table 5.2. Table 5.2 shows that the perpendicular baseline ranging from 66 m to 421 m and combined the information from Table 5.1, the effects of the topographical phase (height ambiguity) can be estimated using Equation (3.11).

$$\min \frac{\lambda R_M Sin(\theta_G^0)}{2B_{\perp,G}^0} < \phi_{topo} < \max \frac{\lambda R_M Sin(\theta_G^0)}{2B_{\perp,G}^0} \tag{5.1}$$

$$\min \frac{\lambda R_M Sin(\theta_G^0)}{2B_{\perp,G}^0} = \frac{0.236x856000xSin(34.3)}{2x66} \approx 862m$$

$$\max \frac{\lambda R_M Sin(\theta_G^0)}{2B_{\perp,G}^0} = \frac{0.236x856000xSin(34.3)}{2x421} \approx 135m$$

It can be estimated that in the interferogram phase, one fringe is equal to 135 m height for 421 m perpendicular baseline whereas 862 m height for 66 m perpendicular baseline.

To suppress the speckle noise, these interferograms were looked down in range and azimuth by 4 and 6, respectively producing roughly 19 m x 19 m pixels. Once the interferogram was generated, a flattening process was applied to exclude the phase trend

expected from a curved Earth (ϕ_{curv}) based on the first term of Equation (3.13). The flattened interferograms and their coherence are presented in Figure 5.2. It is shown that clear fringes are located around the volcano, and it relates to either topographical phase or deformation phase.

As discussed in Section 3.3 especially expressed in Equation (3.14), to obtain the particular phase of ground deformation based on InSAR data processing, other unwanted signals phase should be mitigated or reduced, especially the topographic phase. It was found that the perpendicular baseline for each interferogram was not equal to zero and therefore 2-pass DInSAR strategy should be applied (single interferometric pair and non-zero baseline strategy data processing) to eliminate topographical phase (ϕ_{topo}) as illustrated in Figure 3.4.

There are two strategies to calculate the topography contribution based on an interferogram, the first strategy is from an interferogram image which is derived from two radar images; and the other strategy is derived from simulation of existing digital elevation model (DEM).

A complete DEM for the world is available since the SRTM (Shuttle Radar Topography Mission) was launched by NASA on 2000 (Farr and Kobrick, 2000). SRTM data are organized into individual cells, covering one degree by one degree in latitude and longitude. Sample spacing for individual data points are 1 arc second, 3 arc seconds, or 30 arc seconds. They are referred to as SRTM-1, SRTM-3 and SRTM-30, respectively.

However, up to now, the 1 arc second only covers the United States of America regions, while for the rest of the world only the 3 arc seconds is available.

For SRTM-3 data, each tile is 1201 pixels wide and 1201 pixels long, and has posting of 8.3333330e-04 degrees. Each tile is identified by the geographical coordinate of the bottom left pixel. For example a tile called N02E120.hgt covers an area between 2 and 3 degree North and between 120 and 121 degree East.

The disadvantage of the SRTM data is the gap or the hole which corresponds to no data value that exists in the data. In addition there are no data that covers high latitude (near polar) area. The gap that exists in SRTM data is a consequence of the interferometric method that is used to process the SRTM data especially in phase unwrapping step.

In this study, the topographic phase was derived from a simulation of the SRTM-3 data. Mirone tool (Luis, 2007) was used to prepare the SRTM data including filling the gaps and conversion format to derive a DEM. To reduce pixel size contribution error, the SRTM data was manipulated by resampling to 20 m resolution using weighted interpolation and adaptive smoothing window which was available in GAMMA SAR Software. Then the DEM was simulated to derive topographic phase based on the second term of Equation (3.13).

Precise orbital information is needed to remove the possible orbital fringes (ϕ_{orb}). This study estimated the baseline in two steps, first by combining the satellite orbit state vectors and fringe rate as initial information. Next, by refining this baseline using

ground control points derived from DEM after phase unwrapping step. After removing the topographic and orbital effects, phase noise (ϕ_{noise}) was reduced by applying adaptive filtering (Goldstein and Warner, 1998) to the differential interferogram.

Phase unwrapping was performed to retrieve the topographic height, displacement information by adding the correct integer multiple of 2π to the interferometric fringes. In this study, minimum cost flow (MCF) algorithm (Costantini, 1998) was used to deal with low coherence areas due to layover and shadowing caused by rough terrain. The unwrapping differential phase of PALSAR for Ibu Volcano can be seen in Figure 5.3.

Series of the unwrapped differential phase were analyzed and it was found that four interferograms show an anomaly in differential phase value. Until this data processing stage, based on the Equation (3.13), all the unwanted signals had been eliminated except the atmospheric phase (ϕ_{atm}). Therefore these anomalies are related to the atmospheric phase and should be mitigated from the differential phase because the effect of atmospheric phase is large. The atmospheric phase depends strongly on the meteorological conditions as well as on the topography of the sites.

The atmosphere is one of the most important limiting factors in InSAR application since its properties, the water vapor in troposphere layer, delay the signals propagation. The effect of the atmospheric delay to InSAR result is illustrated in Figure 5.4. The atmospheric phase can be mitigated by:

- Stacking the interferograms (Zebker et al., 1997). This method involves temporal averaging of numbers that are independent of each other to reduce

the temporally uncorrelated noise. However this method will degrade the temporal resolution of InSAR measurement (Li et al., 2006)

- Permanent scatterers techniques (Ferretti et al., 2001). This method is based on the strong correlation of the atmospheric components at short distances, in which the mean value of the atmospheric phase screen contribution is estimated from large number of interferograms. The atmospheric phase screen contribution is removed by filtering resampling techniques.
- Calibration with external data sources, such as continuous GPS networks (Bock and Williams, 1997; Williams et al., 1998) or space-based atmospheric monitoring (Li et al., 2005).
- Modeling the atmospheric phase based on terrain elevation information (Li et al., 2006). The height-dependent model is based on assumption that the atmospheric path delay depends upon the atmospheric water vapor and the pressure profiles between the acquisitions of the interferometric pair and linear relation to altitude.

From four strategies mentioned above, modeling the atmospheric phase based on topography had been the only option for Ibu Volcano area since stacking method would degrade the temporal resolution. There were only five interferograms available, and which was not adequate to apply permanent scatterers strategy. Moreover, there has been no GPS station or other meteorological data that can be applied as a correction to the interferograms.

This study applies a linear phase trend estimated from terrain elevation information, derived from a digital elevation model (DEM) data to reduce the atmospheric phase. This method estimates a linear height dependent atmospheric phase ($Est\phi_{atm}$) based on phase constant (a_0) in radians, and phase slope (a_1) in units of radians per meter.

$$Est\phi_{atm} = a_0 + a_1 \times DEM \tag{5.2}$$

The height dependent atmospheric phase estimates were subtracted from the differential phase, resulting in deformation and unmodeled atmospheric phases. To assess the result of this strategy, a line profile across the volcano was generated as illustrated as line AB in Figure 5.3. The profile along line AB of each interferogram was compared before and after the atmospheric phase mitigation strategy was applied. It is shown that this strategy can mitigate the atmospheric phase significantly and therefore the deformation of Ibu Volcano can be analyzed. It is also shown that there is a large phase variation around the crater as marked by a square in Figure 5.3 and this area became the focus of the deformation analysis related to volcanic activity.

5.4. Results

The corrected differential phase was converted to line of sight (LOS) displacements. Assuming that the displacement is purely in the vertical direction, the magnitude can be quantified as a function of incidence angle (θ). The vertical component of LOS displacement was calculated using Equation (4.1).

The spatial median filter was applied to reduce noise that might be caused by unmodeled atmospheric error. Displacement in contour maps and profiles were then

derived and the results can be seen in Figure 5.5. It is shown that there was 2 cm inflation around the rim of crater and 1 cm subsidence on the crater between August 2007 and October 2007. The volcanic process then continued to deflation, which was approximately 7 cm only on the crater between October 2007 and January 2008 observation. Then, there were almost no displacements detected from two interferograms of January 2008 to February 2008, and February 2008 to April 2008 observations. For the last interferogram, 10 cm subsidence on the crater between April 2008 and July 2008 was detected.

As mentioned before, volcanic activities including both earthquakes and eruptions increased significantly after January 2008. Compared with seismic data as illustrated in Figure 5.6, it was shown that the inflation-deflation process was dominated by deep volcanic earthquake, whereas large subsidence between April 2008 and July 2008 was related to shallow and eruption earthquakes. As high number of eruptions was recorded, surely number of ejected materials from beneath also increased and influenced the volume changes of pressure source at Ibu Volcano.

DInSAR results showed a concentric deformation pattern around the crater, which was a characteristic of central eruption type (Minakami, 1960). The maximum height of ash column during the eruption was observed at 800 m above the crater which was classified into scale 1 of Volcanic Explosivity Index (VEI), small, strombolian and effusive eruptions type (Newhall and Self, 1982). This classification agrees with the small ground deformation detected by DInSAR.

This study had shown the ability of L-band PALSAR data to sense ground deformation around Ibu Volcano by applying DInSAR technique. Despite the location of Ibu Volcano in a tropical region with dense vegetation covering its surface, deformation assumed to be related to the volcanic activities could be observed. It was found that the ground deformation had already started since October 2007 and the largest deformation was detected during the period April 2008 – July 2008.

PALSAR with DInSAR data processing is useful for detecting ground deformation especially in remote areas that are hard to access, a problem commonly found in an archipelagic country like Indonesia. Such techniques can be used to provide complementary data in determining the volcanic status in Indonesia and for natural hazards mitigation.

CHAPTER 6

INSAR LONG TERM GROUND DEFORMATION MONITORING

Long temporal baseline deformation monitoring using InSAR has a challenge of decreasing coherence between images. However, to monitor a long and steady deformation such as an active volcano needs sequences long term observation. This chapter describes strategies to deal with long term ground deformation monitoring by InSAR technique. As a case study, Anak Krakatau Volcano that shows an increasing activity for almost two years (2007 to 2009) is selected. A new technique called post-processing filtering technique to improve interpretation of ground deformation derived from InSAR estimates is also explained in this chapter to show the ability of InSAR technique to detect ground deformation in small volcanic island for longer time period.

6.1. Introduction of Study Area

Anak Krakatau is a small volcanic island located in the center of Krakatau complex (as illustrated in Figure 6.1) in the volcanic arc that extends 7000 km in Indonesian region (as illustrated in inset map of Figure 5.1). The Krakatau complex consists of four islands: Sertung, Panjang, Rakata, which are remnant of the caldera collapse of the August 27 1883 Krakatau eruption, and Anak Krakatau, which was born on February 18 1929 or 46 years after that paroxysmal eruption, and was constructed of alternating layers of lava and pyroclastic deposits that had been formed since 1930 (Sutawidjaja, 1997). In addition, the presence of Anak Krakatau activity appears as a consequence of

its location on the intersection of an active fault with the north-south trending volcanic line in Sunda Strait (Harjono et al., 1991).

Since it is located in Sunda Strait, the Krakatau complex is influenced by the tectonic setting of this region. The Sunda Strait marks the transitional zone from Sumatra trench with oblique subduction to Java trench with nearly frontal subduction. This implies the opening of Sunda Strait which was initiated in the early Late Miocene created the evolution of three major graben systems which had been regarded as pull-apart basins (Susilohadi et al., 2009). These three major graben systems are West and East Semangko Grabens and Krakatau Graben. Pull-apart basins formation and the opening of Sunda Strait are the main source of clastics related to volcanism in this region.

Previous studies in Sunda Strait found that most of this area is mostly covered by Quaternary volcanic products (Nishimura et al., 1986) and that the volcanic complex in this area is characterized by an explosive behavior. A weakness zone with $N150^{o}$ orientation is also identified (Deplus et al., 1995). The magma body for Krakatau complex is identified in two zones, at a depth of 22 km with very large reservoir, and at a depth of 9 km which consists of separate pockets of magma and fractures directly beneath and south of Anak Krakatau (Harjono et al., 1989).

Many studies that have been conducted on Krakatau complex, mainly discussed the famous 1883 Krakatau eruption and its tsunamis (Yokoyama, 1981; 1987; Rampino and Self, 1982; Francis, 1985; Dories, 2003); and Anak Krakatau (Sutawidjaja, 1997; Deplus et al., 1995; Ibs-von Seht, 2008). However, studies on ground deformation as

one indicator of volcanic activity for Anak Krakatau are still limited. Yet there are two observation stations developed to monitor this volcano and designed to record deep (A-type) and shallow (B-type) volcanic earthquakes (Minakami, 1960) from analog seismograph. However, to understand the status of a volcano, a complete volcano monitoring system comprising seismic observation, geodetic observation and geochemical observation (Dzurisin, 2007) is required.

One technique in geodetic observation for volcano deformation detection is interferometric synthetic aperture radar (InSAR) that has been used since 1995 to monitor surface displacement related to volcanic activity. Massonnet and Feigl (1998) had successfully documented ground deformation before, during and after eruptions with 1 cm vertical accuracy for Mount Etna in Italy. However, Stevens and Wadge (2004) highlighted some factors that might constrain the InSAR application for volcano monitoring such as:

1. Radar system constraints. These factors include data swath width and spatial resolution, wavelength, orbit repeat interval, baselines, pointing, line of sight, and data storage and reception.
2. Surface constraints. This factor related to the impact of vegetation and slope to InSAR result. On some volcanoes the only non-vegetated surfaces available to give clear signals are recent volcanic deposits. If there another deposits came, these surfaces can become non-coherent.
3. Operational constraints. These factors include targeting the object, sensor lifespan, processing, and archival data.

4. Interpretational constraints. These factors are related to how to interpret the InSAR estimates of volcano deformation. Most of the analysis assumed that the observed deformation field could be represented by a point source in an elastic half-space (Mogi model), finite shape of the pressure source, discontinuities and surface topography, fracture dislocation on dikes, and aseismic gravity sliding on decollement or fault systems.

Since InSAR works are based on coherent radar, coherence aspect is the most important in detecting ground deformation using this technique. Coherence is affected by environment condition including medium that propagated and target on the surface. These conditions depend much on time observation including the season and time separation between observations. Longer time separation will degrade the coherence between images especially in tropical region that is characterized by high humidity, and high dense vegetation. However, in some cases in deformation monitoring, longer time interval observation is required to understand the mechanism of deformation.

Anak Krakatau Volcano showed an increasing activity including the eruption stage that started at the end of October 2007 and ended on August 2008 after being reposed in six years. To understand this event, PALSAR data ranging from June 2007 to February 2009 was processed by applying DInSAR technique with one common master data.

6.2. Data Sets

Five ascending Level 1.0 and 1.1 PALSAR data which were observed on June 2007, September 2007, February 2008, September 2008, and February 2009 (Table 6.1) were

processed using GAMMA SAR Software (Wegmuller and Werner, 1997) to obtain SLC images and interferometric phase. Table 6.1 shows that the time difference for each observation ranging from 92 days to 598 days. Single Look Complex (SLC) image generation processes as discussed in Section 3.1 are applied to Level 1.0 data. Conversion format from CEOS data format to GAMMA SAR data format is applied for Level 1.1 data by applying appropriate radiometric calibration value.

To deal with different observation mode, oversampling method (Werner et al., 2007) as mentioned in Section 5.3 is applied to Fine Beam Dual (FBD) polarization observation mode to obtain the same dimension with Fine Beam Single (FBS) polarization observation mode. The image of PALSAR data for Anak Krakatau Volcano is illustrated in Figure 6.2.

6.3. Data Processing Strategies

6.3.1. Differential interferogram derivation

Once the SLC images are generated, then the focus area is cropped out to derive the interferogram and deformation signals. This strategy is applied to minimize the co-registration error that might be occurred since the area is surrounded by open water. Open water is a specular reflector for radar signals that make the amplitude of each pixel almost zero (signal strength is low). This condition degrades the number of pixel offset when registering the slave image to master image to conform the geometry. Large number of pixel offset with high accuracy estimation ensures the visibility of interferogram generated.

As had been discussed in Section 3.3 and described in Section 5.3, the PALSAR data were processed by applying single interferometric pair and non-zero baseline based on two different approaches: first, based on short temporal baseline or sequential InSAR data processing, and secondly based on one common master data processing strategy. Short temporal baseline strategy generates interferogram based on shifting master data. This strategy is advantageous in short term period of ground deformation and for rapid assessment of its deformation. On the other hand, one common master data generates interferogram based on fixed master data. This strategy is useful to monitor the deformation that occurs continuously in long term period and also the information given from all interferograms are based on the same reference. For this study, since Anak Krakatau Volcano shows a long term activity, one common master based strategy is the appropriate strategy to be applied in understanding the mechanism of Anak Krakatau Volcano for 2007 - 2009 eruption periods.

There are three considerations in selecting master data. The first consideration is the epoch observation at least before the eruption stage. Since the eruption period for Anak Krakatau Volcano started on October 2007, there are two possible choices of master data: June 2007 and September 2007. The second consideration is the coherence between master data and the longest time difference (February 2009 data). After assessment especially for image coherence, it was found that the coherence was almost the same level as illustrated in Figure 6.3. The third consideration is the perpendicular baseline. Table 6.1 shows that the average perpendicular baseline of June 2007 combination is smaller compare to September 2007 combination. Therefore, the ground

deformation for Anak Krakatau Volcano was analyzed based on four interferograms derived from June 2007 epoch.

This study utilized the Shuttle Radar Topography Mission (SRTM) 3 arc seconds data to simulate a topographic phase (ϕ_{topo}). The same strategy as discussed in Section 5.3 is applied to improve the quality of SRTM data. The interferograms were looked down by 2 and 3 times in range and azimuth, respectively producing roughly 10 m x 10 m pixels size. Once the interferogram was generated, a flattening process was applied to exclude the phase trend expected from a curved Earth.

To remove the orbital fringes (ϕ_{orb}), a precise satellite baseline was estimated in two steps, at first by combining the satellite orbit state vectors and fringe rate as initial information, and later, the baseline information was refined using ground control points derived from Digital Elevation Model (DEM) after phase unwrapping step. After removing the topographic and orbital effects, phase noise of the differential interferogram was reduced by applying adaptive filtering algorithm (Goldstein and Warner, 1998). Phase series of the interferogram and the flattened interferogram of Anak Krakatau Volcano are illustrated in Figure 6.4.

Phase unwrapping was performed to retrieve the topographic height, displacement information by adding the correct integer multiple of 2π to the interferometric fringes using minimum cost flow (MCF) algorithm (Costantini, 1998). This technique is a global optimization technique to phase unwrapping problem that give the advantages in dealing with the gaps area caused by low coherence by considering their density in

triangular network. In addition, by masking, adaptive thinning and patch processing steps in MCF allows the efficient and robust unwrapping for interferogram image in any dimension. To reduce the atmospheric phase (ϕ_{atm}), this study utilizes a linear phase trend with elevation module as discussed in Section 5.3 and Equation (5.2).

The corrected unwrapped differential phase was converted to vertical component of line of sight (LOS) displacements as illustrated in Figure 3.4. However, the deformation signals as a final objective in ground deformation monitoring was hard to be interpreted as it still contained noise related to volcanic ash, and spatial resolution or pixel size factor. To address this problem a post-processed filtering technique was applied to DInSAR displacement estimates. This technique is proposed to suppress noise and increase the similarity of pixel value based on two-dimensional spatial filtering.

6.3.2. Post-processed filtering technique

Since there was still difficulty in interpreting information obtained from DInSAR due to noise contained, further filtering process called post-processed filtering technique was applied. This technique was based on the fact that noise that interferes with the deformation signals usually originates from different spatial locations. To suppress noise with this pattern, spatial filter can be applied (Veen and Buckley, 1988).

Spatial filtering of digital images such as products of interferometry technique is accomplished by convolving an image (digital data) with a point-spread function (PSF) that is a two-dimensional data of point source (Schowengerdt, 1983). Carr (1990)

showed that if $f(x,y)$ is the original digital data, $g(x,y)$ is the filtered data, a two-dimensional convolution of a PSF with a digital data can be expressed as Equation (6.1). In practice, the PSF is a collection of weights and the convolution is approximated by a double summation as written in Equation (6.2).

$$g(x,y) = PSF(x,y) * f(x,y) \tag{6.1}$$

$$g(x_0,y_0) = \sum_i \sum_j PSF(x_0 - x_i, y_0 - y_j) * f(x_i,y_j) \tag{6.2}$$

Equation (6.2) shows that the PSF is a box filter that is also known as *subimage* or *filter mask* or *filter window* with column and row dimension and its values are referred as coefficients, rather than pixels. The process of spatial filtering consisted simply of moving the filter mask from point to point in the digital data. At each point (x,y) the response of the filter at that point was calculated using a predefined relationship such as linear convolution (weighted averaging) or non-linear convolution (i.e. statistical measure) relationship.

In this study, the LOS displacements were converted from float and big-endian data format (GAMMA SAR Software) to grid data format by modifying Mirone tools (Luis, 2007) utilities. Median filter as a non-linear convolution method was applied to obtain a filtered LOS displacement. The Median filter process ranks the input values to determine window size and assign the median value as the output which is not affected by the actual value of outlier cells within the filter window. The processing chain is illustrated in Figure 6.5. It was found that for interferogram derived in this study, the filter size of 20 x 20 pixels size was effective to improve the grid similarity. A filtered displacement map had the tendency to appear flat unless strong frequency repeat

patterns were brought out. By applying this method, it had been possible to derive LOS displacement map that was useful to study ground deformation.

Figure 6.6 illustrates the LOS displacements before and after applying post-processed filtering technique. The smoothed grids that contain LOS displacements can then be interpreted by modeling the deformation. Based on deformation patterns as illustrated in Figure 6.6, the deformation can be modeled by a rectangular dislocation model on elastic half-space based on Okada solution (Okada, 1992).

6.4. Results and Discussions

From InSAR data processing results, it is clear that during the observation periods, the deformation signals was only found in Anak Krakatau Volcano and was certainly related to the volcanic activity.

Ground deformation pattern from June 2007 to September 2007 showed a shortening LOS displacement (inflation) about 4 cm that was accompanied with an extension LOS displacement (deflation) pattern around the crater in 92 days (Figure 6.6-c1). In this period, only shallow and deep volcanic earthquakes were recorded as illustrated in Figure 6.7. The ground deformation pattern changed to deflation (an extending LOS displacement) from June 2007 to February 2008 for the whole area, especially around the crater, the LOS was extended with a maximum of 16 cm for 230 days (Figure 6.6-c2). During this period, Anak Krakatau started to erupt on October 2007 with an average eruption of 160 times a day. In addition, increasing number of shallow volcanic earthquakes was also recorded.

From early February 2008 to mid April 2008, no eruption was recorded. However, shallow and deep volcanic earthquakes still occurred albeit in small number. Starting April 14 2008, the volcanic activity increased significantly until September 2008. It was shown that the summit area had been inflated (LOS was shortened) up to 20 cm whereas the southwestern flank was deflated (LOS was extended) by 10 cm in 460 days, from June 2007 to September 2008 (Figure 6.6-c3). The eruption stage stopped on August 2008 but the volcanic activity continued, as indicated by shallow and deep volcanic earthquakes. Shallow volcanic earthquake dominated the volcanic activity starting December 2008 until the end of observation period. In this period, it showed a continuation in deformation pattern of the previous period. From June 2007 to February 2009 (Figure 6.6-c4), the southwestern area continued to deflate (LOS was extended) with 18 cm whereas the northeastern area was inflated (LOS was shortened) with maximum 12 cm in 598 days.

The ground deformations estimated from InSAR were then modeled to have an idea of the source that controlled Anak Krakatau activity during the time of observation based on June 2007. Hence, ground deformations obtained from DInSAR data processing and filtered with Median filter in prost-processed strategy were analyzed and modeled. This approach ensures a reliable result since the utilization of a single master data allowed a more consistent way of detecting the changes as they were processed based on the same master data. A LOS displacement profile was generated for each period to identify the deformation pattern (Figure 6.8). The deformation pattern indicates a dipping rectangular tensile dislocation mechanism, especially after the eruption started on October 2007.

Since the deformed area was only detected in small region, it was assumed that the source was located in shallow depth. After assessing various depths from 0 to 1 km, it was found that the source was located on 400 m depth. Fault and dislocation geometry parameter, based on Feigl and Dupre (1999) definition, were estimated by constraining the ground deformation observed by InSAR for each period. The results are tabulated in Table 6.2 and illustrated in Figure 6.9. A dipping rectangular tensile dislocation model estimated a maximum opening of an approximately 4 m with normal faulting mechanism that was found on June 2007 to February 2009 observation period. The strike direction slightly changed from each period and dip angle changed from 65^{o} to 50^{o}, which indicated a dyke intrusion.

Residual and LOS displacement profile from observed, filtered and modeled results was compared and it showed the model fit well especially in the second observation period (June 2007 to February 2008) as illustrated in Figure 6.10 and 6.11. There was an inflation-deflation pattern before the eruption, whereas after the eruption started, subsidence occurred on the southwestern flank of the summit. On the other hand, the northeastern flank continued to uplift. In this observation period, it was found that Anak Krakatau uplifted 12 cm/year in average.

The volume source at the first observation and the last observation slightly decreased. Before eruption, the volume change was estimated at 1.06×10^{6} m^{3} in 92 days, whereas it was 1.25×10^{6} m^{3} after the eruption in 598 days, from June 2007 to February 2009 as illustrated in Figure 6.12. It was found that during the 2007-2008 eruptions period, the source was dominated by a dip-slip components coupled with an opening component.

The LOS displacement profile suggests the same pattern of morphological evolution with time of Anak Krakatau discussed by Deplus et al. (1995). It indicates the southwestern flank of the cone is more unstable compared to the northeastern flank, which the tensile crack source is estimated located on this area.

Anak Krakatau is located in Krakatau complex and Krakatau Graben, the volcanic activity in this region is influenced by Sunda Strait tectonic setting, identified as an active pull-apart basin. This mechanism increases the potential hazard related to volcano volatility, which is proven from the periodic eruption cycle of Anak Krakatau that has been recorded at least every one to six year (Venzke et al., 2002) and summarized in Table 6.3 and shown in Figure 6.13. It is shown that the activity of Anak Krakatau was almost constant in term of temporal cycle and that maximum scale of volcanic explosive index (VEI) was 2 since its initial eruption in 1927.

In addition, Sutawidjaja (1997) illustrated the growth of Anak Krakatau as shown in Figure 6.13. It is shown in Figure 6.13 that there are three extreme time periods related to height progression: first period from 1927 to 1935, second period from 1952 to 1957, and third period starting from 1982 until 1996.

The model estimates the northwestward fault strike direction which is parallel to the association of the Sunda Strait opening with the northwestward movement of the Sumatra Sliver (Susilohadi et al., 2009). In addition, the fault orientation from this model, which is characterized as NW-SE trend, corresponds to the behavior of Sumatra oblique subduction orientation and Sumatra fault system in general.

The ground deformation is caused by a shallow tensile source, which has variations in fault dimension, albeit in small dimension. Indeed, Harjono et al. (1989) had identified the magma body located in upper (9 km) and deep (22 km) zones with large reservoir. The magma intrusion could reach tensile source location by the activation of the NW-SE fault system which was identified by Susilohadi et al. (2009).

During 2007-2008 eruptions period, the source was speculated to have originated from the shallow reservoir zone considering the same horizontal position of magma body location estimated by Harjono et al. (1989) and volcanic source location estimated by this study. This study also found that the intruding magma was only in small total volume of an approximately 1.25 x 10^6 m^3 indicating the small quantity of energy involved during this eruption period. However, recognizing other eruptive characteristics, such as a column height of more than 1 km, Strombolian and explosive eruption type; this eruption period can be classified into scale 2 of Volcanic Explosivity Index (Newhall and Self, 1982).

However, this study shows the limitation of InSAR to detect clear fringe visibility on the low coherence area covered by volcanic ash. In addition there is no ground truth data (i.e. GPS observation or leveling data) that can be used to validate the InSAR estimates. It is shown that after applying post-processed filtering technique of vertical displacement, the deformation pattern can be modeled to understand the volcanic sources. In conclusion, this study shows the ability of InSAR technique to detect ground deformation for Anak Krakatau Volcano.

CHAPTER 7

CONCLUSIONS AND RECOMMENDATIONS

One of the advantageous of remote sensing technique is the ability to access the hard, remote and even dangerous location as have been described and discussed in three chapters of this study. Hard access at Manokwari region in Papua Island, remote area in Halmahera Island, both in eastern part of Indonesia; and dangerous location in Anak Krakatau Volcano, a small volcanic island in Sunda Street, are the selected location to conduct the research on ground deformation by utilizing L-band PALSAR data using differential interferometry technique.

Large ground deformation and its pattern related to co-seismic event in high-dense vegetation covered in tropical region was clearly detected by processing ALOS-PALSAR data in interferometric technique. This result shows the advantage of L-band to deal with canopy factor in ground deformation studies. Moreover, long wavelength of L-band radar also can accommodate large displacement in fringe visibility.

Small ground deformation in vicinity Ibu Volcano in Halmahera Island can also be detected by utilizing L-band ALOS-PALSAR data in differential interferometric technique. It is shown that by mitigating and reducing other unwanted signals from the interferogram, deformation signals can be pointing out. It is also shown that the atmospheric phase is the most contributor signals after removing topographical phase from simulating a digital elevation model. In this study, the atmospheric phase was

subtracted out by modeling its signals based on linear-dependent height algorithm. This study can quantify the deformation based on sequential observation to make clear the deformation for each observation period related to volcanic activity.

For long term observation, the mechanism of Anak Krakatau Volcano during its eruption period on 2007 – 2009 can be analyzed by InSAR estimates. From analyzing the interferograms, it shows that it is very hard to get a clear fringe around the crater after the eruption due to the low coherence areas. The low coherence area might be related to the volcanic ash (contains gas, liquid and solid materials) that disturb the phase propagation. To address the heterogeneity of pixel value, post-processed filtering technique is suitable to be applied. It is found that by applying non-linear spatial filtering, the deformation pattern of erupted Anak Krakatau Volcano can be analyzed.

This research found that extending InSAR data processing strategies with post-processed filtering technique enhances the ground deformation signals detection in Indonesian region which is located in low latitude, mostly covered by dense tropical rain forest, and high precipitation in the atmosphere.

For further research, it is interesting to analyze the possibility to improve the atmospheric phase mitigation based on assimilating an appropriate external weather and meteorological data. Also, the characteristic of low coherence area is interesting to be analyzed, how to distinguish whether it is caused by land cover changes or by volcanic ash.

REFERENCES

Abers, G. and McCaffrey, R., 1988. Active Deformation in the New Guinea Fold-and-Thrust Belt: Seismological Evidence for Strike-Slip Faulting and Basement-Involved Thrusting. *Journal of Geophysical Research*, 93(B11): 13332-13354.

Aki, K. and Richards, P.G., 2002. *Quantitative Seismology*. University Science Books, 700 pp.

Arnadottir, T., Jonsson, S., Pollitz, F.F., Jiang, W. and Feigl, K.L., 2005. Postseismic Deformation Following the June 2000 Earthquake Sequence in the South Iceland Seismic Zone. *Journal of Geophysical Research*, 110(B12308).

Bawden, G.W., Thatcher, W., Stein, R.S., Hudnut, K.W. and Peltzer, G., 2001. Tectonic Contraction across Los Angeles after Removal of Groundwater Pumping Effects. *Nature*, 412: 812-815.

Bercovici, D., 2003. The Generation of Plate Tectonics from Mantle Convection. *Earth and Planetary Science Letters (Frontiers)*, 205: 107-121.

Bird, P., 2003. An Updated Digital Model of Plate Boundaries. *Geochemistry Geophysics Geosystem*, 4(3), 1027, doi:10.1029/2001GC000252.

Bock, Y. and Williams, S., 1997. Integrated Satellite Interferometry in Southern California. *EOS Trans. AGU*, 78(29): 290-300.

Burgmann, R., Rosen, P. and Fielding, E., 2000a. Synthetic Aperture Radar Interferometry to Measure Earth's Surface Topography and Its Deformation. *Annual Reviews of Earth and Planetary Sciences*, 28: 169-209.

Burgmann, R., Schmidt, D., Nadeau, R.M., d'Alessio, M., Fielding, E., Manaker, D., McEvilly, T.V. and Murray, M.H., 2000b. Earthquake Potential Along the Northern Hayward Fault, California, *Science*, 289(5482): 1178-1182.

Cakir, Z., Akoglu, A.M., Belabbes, S., Ergintav, S. and Meghraoui, M., 2005. Creeping Along the Ismetpasa Section of the North Anatolian Fault (Western Turkey): Rate and Extent from InSAR. *Earth and Planetary Science Letters*, 238(1-2): 225-234.

Carnec, C., Massonnet, D. and King, C., 1996. Two Examples of the Use of SAR Interferometry on Displacement Fields of Small Spatial Extent. *Geophysical Research Letters*, 23(24): 3579-3582.

Carr, J., 1990. Application of Spatial Filter Theory to Kriging. *Mathematical Geology*, 22(8): 1063-1079.

Colesanti, C., Ferretti, A., Prati, C. and Rocca, F., 2003. Monitoring Landslides and Tectonic Motions with the Permanent Scatterers Technique. *Engineering Geology*, 68(1-2): 3-14.

Costantini, M., 1998. A Novel Phase Unwrapping Method Based on Network Programming. *IEEE Transactions Geoscience and Remote Sensing*, 36(3): 813-821.

Curlander, J.C. and McDonough, R.N., 1991. *Synthetic Aperture Radar: Systems and Signal Processing*. John Wiley & Sons, New York, 647 pp.

Delouis, B., Giardini, D., Lundgren, P. and Salichon, J., 2002. Joint Inversion of InSAR, GPS, Teleseismic, and Strong-Motion Data for the Spatial and Temporal Distribution of Earthquake Slip: Application to the 1999 Izmit Mainshock, *Bulletin of the Seismological Society of America*, 92(1): 278-299.

DeMets, C., Gordon, R.G., Argus, D.F. and Stein, S., 1990. Current Plate Motions. *Geophysical Journal International*, 101(2): 425-478.

Deplus, C., Bonvalot, S., Dahrin, D., Diament, M., Harjono, H. and Dubois, J., 1995. Inner Structure of the Krakatau Volcanic Complex (Indonesia) from Gravity and Bathymetry Data. *Journal of Volcanology and Geothermal Research*, 64(1-2): 23-52.

Dörries, M., 2003. Global Science: The Eruption of Krakatau. *Endeavour*, 27(3): 113-116.

Dzurisin, D., 2007. *Volcano Deformation New Geodetic Monitoring Techniques*. Springer Praxis Books, UK, 441 pp.

Elachi, C., 1982. Radar Images of the Earth. *Scientific American*, 271(6): 54.

Elachi, C., 1988. Spaceborne Radar Remote Sensing: Applications and Techniques. *IEEE Press*: 285.

EORC, 2008. *ALOS Data Users Handbook Revision C*, Earth Observation Research and Application Center, Japan Aerospace Exploration Agency.

Ernst, G.G.J., Kervyn, M. and Teeuw, R.M., 2008. Advances in the Remote Sensing of Volcanic Activity and Hazards, with Special Consideration to Applications in Developing Countries. *International Journal of Remote Sensing*, 29(22): 6687-6723.

Farr, T.G. and Kobrick, M., 2000. Shuttle Radar Topography Mission Produces a Wealth of Data. *EOS Trans. AGU*, 81: 583-585.

Feigl, K.L. and Dupre, E., 1999. Rngchn: A Program to Calculate Displacement Components from Dislocations in an Elastic Half-Space with Applications for Modeling Geodetic Measurements of Crustal Deformation. *Computers and Geosciences*, 25: 695-704.

Feigl, K.L., Sarti, F., Vadon, H., McClusky, S., Ergintav, S., Durand, P., Burgmann, R., Rigo, A., Massonnet, D. and Reilinger, R., 2002. Estimating Slip Distribution for the Izmit Mainshock from Coseismic GPS, ERS-1, Radarsat, and Spot Measurements, *Bulletin of the Seismological Society of America*, 92(1): 138-160.

Ferretti, A., Prati, C. and Rocca, F., 2001. Permanent Scatterers in SAR Interferometry. *IEEE Transactions on Geoscience and Remote Sensing*, 39(1): 8-20.

Franceschetti, G. and Lanari, R., 1999. *Synthetic Aperture Radar Processing*. CRC Press, Boca Raton, 307 pp.

Francis, P.W., 1985. The Origin of the 1883 Krakatau Tsunamis. *Journal of Volcanology and Geothermal Research*, 25(3-4): 349-363.

Goldstein, R.M. and Werner, C.L., 1998. Radar Interferogram Filtering for Geophysical Applications. *Geophysical Research Letters*, 25(21): 4035-4038.

Hanks, T.C. and Kanamori, H., 1979. A Moment Magnitude Scale. *Journal of Geophysical Research*, 84(B5): 2348-2350.

Hanssen, R.F., 2001. *Radar Interferometry: Data Interpretation and Error Analysis*. Kluwer Academic Publishers, Dordrecht, 328 pp.

Harjono, H., Diament, M., Nouaili, L. and Dubois, J., 1989. Detection of Magma Bodies beneath Krakatau Volcano (Indonesia) from Anomalous Shear Waves. *Journal of Volcanology and Geothermal Research*, 39(4): 335-348.

Harjono, H., Diament, M., Dubois, J., Larue, M. and Zen, M.T., 1991. Seismicity of the Sunda Strait: Evidence for Crustal Extension and Volcanological Implications. *Tectonics*, 10(1): 17-30.

Hayes, G., 2009. *Preliminary Result of the Jan 3, 2009 Mw 7.6 Papua Earthquake*, http://earthquake.usgs.gov/earthquakes/eqinthenews/2009/us2009bjbn/

Ibs-von Seht, M., 2008. Detection and Identification of Seismic Signals Recorded at Krakatau Volcano (Indonesia) Using Artificial Neural Networks. *Journal of Volcanology and Geothermal Research*, 176(4): 448-456.

Kanamori, H., 1977. The Energy Release in Great Earthquakes. *Journal of Geophysical Research*, 82(20): 2981-2987.

Li, Z., Muller, J.-P., Cross, P. and Fielding, E.J., 2005. Interferometric Synthetic Aperture Radar (InSAR) Atmospheric Correction: GPS, Moderate Resolution Imaging Spectroradiometer (MODIS), and InSAR Integration. *Journal of Geophysical Research*, 110(B03410).

Li, Z.W., Ding, X.L., Huang, C., Wadge, G. and Zheng, D.W., 2006. Modeling of Atmospheric Effects on InSAR Measurements by Incorporating Terrain Elevation Information. *Journal of Atmospheric and Solar-Terrestrial Physics*, 68(11): 1189-1194.

Lu, Z., Mann, D. and Freymueller, J., 1998. Satellite Radar Interferometry Measures Deformation at Okmok Volcano. *EOS Trans. AGU*, 79(39): 461-468.

Luis, J.F., 2007. Mirone: A Multi-Purpose Tool for Exploring Grid Data. *Computers and Geosciences*, 33(1): 31-41.

Massonnet, D. and Rabaute, T., 1993. Radar Interferometry: Limits and Potential. *IEEE Transactions on Geoscience and Remote Sensing*, 31(2): 455-464.

Massonnet, D., Briole, P. and Arnaud, A., 1995. Deflation of Mount Etna Monitored by Spaceborne Radar Interferometry. *Nature*, 375(6532): 567-570.

Massonnet, D. and Feigl, K.L., 1998. Radar Interferometry and Its Applications to Changes in Earth's Surface. *Reviews of Geophysics*, 36: 441-500.

Minakami, T., 1960. Fundamental Research for Predicting Volcanic Eruptions (Part 1). *Bulletin of the Earthquake Research Institute*, 38.: 497-544.

Newhall, C.G. and Self, S., 1982. The Volcanic Explosivity Index (VEI) an Estimate of Explosive Magnitude for Historical Volcanism. *Journal of Geophysical Research*, 87: 1231-1238.

Nishimura, S., Nishida, J.i., Yokoyama, T. and Hehuwat, F., 1986. Neo-Tectonics of the Strait of Sunda, Indonesia. *Journal of Southeast Asian Earth Sciences*, 1(2): 81-91.

Okada, Y., 1992. Internal Deformation Due to Shear and Tensile Faults in a Half-Space. *Bulletin of the Seismological Society of America*, 82(2): 1018-1040.

Palano, M., Puglisi, G. and Gresta, S., 2008. Ground Deformation Patterns at Mt. Etna from 1993 to 2000 from Joint Use of InSAR and GPS Techniques. *Journal of Volcanology and Geothermal Research*, 169(3-4): 99-120.

Puntodewo, S.S.O., McCaffrey, R., Calais, E., Bock, Y., Rais, J., Subarya, C., Poewariardi, R., Stevens, C., Genrich, J., Fauzi, Zwick, P. and Wdowinski, S., 1994. GPS Measurements of Crustal Deformation within the Pacific-Australia Plate Boundary Zone in Irian Jaya, Indonesia. *Tectonophysics*, 237(3-4): 141-153.

Rampino, M.R. and Self, S., 1982. Historic Eruptions of Tambora (1815), Krakatau (1883), and Agung (1963), Their Stratospheric Aerosols, and Climatic Impact. *Quaternary Research*, 18(2): 127-143.

Raucoules, D., Colesanti, C. and Carnec, C., 2007. Use of SAR Interferometry for Detecting and Assessing Ground Subsidence. *Comptes Rendus Geosciences*, 339(5): 289-302.

Rosenqvist, A., Shimada, M., Ito, N. and Watanabe, M., 2007. ALOS PALSAR: A Pathfinder Mission for Global-Scale Monitoring of the Environment. *IEEE Transactions on Geoscience and Remote Sensing*, 45(11): 3307-3316.

Roth, L.E. and Wall, S.D., 1995. The Face of Venus, the Magellan Radar-Mapping Mission, *National Aeronautics and Space Administration*, Washington, D.C.

Sandwell, D.T., Myer, D., Mellors, R., Shimada, M., Brooks, B. and Foster, J., 2008. Accuracy and Resolution of Alos Interferometry: Vector Deformation Maps of the Father's Day Intrusion at Kilauea. *IEEE Transactions on Geoscience and Remote Sensing*, 46(11): 3524-3534.

Schowengerdt, R.A., 1983. *Techniques for Image Processing and Classifications in Remote Sensing*. Academic Press, 249 pp.

Stevens, N. and Wadge, G., 2004. Towards Operational Repeat-Pass SAR Interferometry at Active Volcanoes. *Natural Hazards*, 33(1): 47-76.

Susilohadi, S., Gaedicke, C. and Djajadihardja, Y., 2009. Structures and Sedimentary Deposition in the Sunda Strait, Indonesia. *Tectonophysics*, 467(1-4): 55-71.

Sutawidjaja, I.S., 1997. The Activities of Anak Krakatau Volcano During the Years of 1992-1996. *Annuals of the Disaster Prevention Research Institute*, 40: 13-22.

Thornton, I.W.B., Ward, S.A., Zann, R.A. and New, T.R., 1992. Anak Krakatau - a Colonization Model within a Colonization Model? *GeoJournal*, 28(2): 271-286.

Tobita, M., Fujiwara, S., Ozawa, S., Rosen, P.A., Fielding, E.J., Werner, C.L., Murakami, M., Nakagawa, H., Nitta, K. and Murakami, M., 1998. Deformation of the 1995 North Sakhalin Earthquake Detected by JERS-1/SAR Interferometry. *Earth Planets Space*, 50: 313-325.

Veen, B.D.V. and Buckley, K.M., 1988. Beamforming: A Versatile Approach to Spatial Filtering. *IEEE ASSP Magazine*, 5: 4-24.

Venzke E, Wunderman R W, McClelland L, Simkin, T, Luhr, JF, Siebert L, Mayberry G, and Sennert S (eds.) (2002). Global Volcanism, 1968 to the Present. Smithsonian Institution, *Global Volcanism Program Digital Information Series*, GVP-4 (http://www.volcano.si.edu/reports/).

Wegmuller, U. and Werner, C., 1997. GAMMA SAR Processor and Interferometry Software. *Third ERS Symposium on Space at the service of our Environment*, held in Florence, Italy, 14-21 March, 1997. Compiled by T.-D. Guyenne and D. Danesy. European Space Agency, p.1687.

Werner, C., Wegmuller, U., Strozzi, T., Wiesmann, A. and Santoro, M., 2007. PALSAR Multi-Mode Interferometric Processing, *The First Joint PI symposium of ALOS Data Nodes for ALOS Science Program*, Kyoto.

Williams, S., Bock, Y. and Fang, P., 1998. Integrated Satellite Interferometry: Tropospheric Noise, GPS Estimates and Implications for Interferometric Synthetic Aperture Radar Products. *Journal of Geophysical Research*, 103(B11): 27051-27067.

Winchester, S., 2003. *Krakatoa: The Day the World Exploded: August 27, 1883*. Perennial, New York, 416 pp.

Wong, F. and Cumming, I.G., 1996. A Combined SAR Doppler Centroid Estimation Scheme Based Upon Signal Phase. *IEEE Transactions on Geoscience and Remote Sensing*, 34(3): 696-707.

Yamanaka, Y., 2009. *Seismological Notes Ngy No.13* (in Japanese), http://www.seis.nagoya-u.ac.jp/sanchu/Seismo_Note/2009/NGY13.html.

Yokoyama, I., 1981. A Geophysical Interpretation of the 1883 Krakatau Eruption. *Journal of Volcanology and Geothermal Research*, 9(4): 359-378.

Yokoyama, I., 1987. A Scenario of the 1883 Krakatau Tsunami. *Journal of Volcanology and Geothermal Research*, 34(1-2): 123-132.

Zebker, H.A. and Villasensor, J., 1992. Decorrelation in Interferometric Radar Echoes. *IEEE Transactions on Geoscience and Remote Sensing*, 30(5): 950-959.

Zebker, H.A., Rosen, P.A. and Hensley, S., 1997. Atmospheric Effects in Interferometric Synthetic Aperture Radar Surface Deformation and Topographic Maps. *Journal of Geophysical Research*, 102(B4): 7547-7563.

FIGURES
AND
TABLES

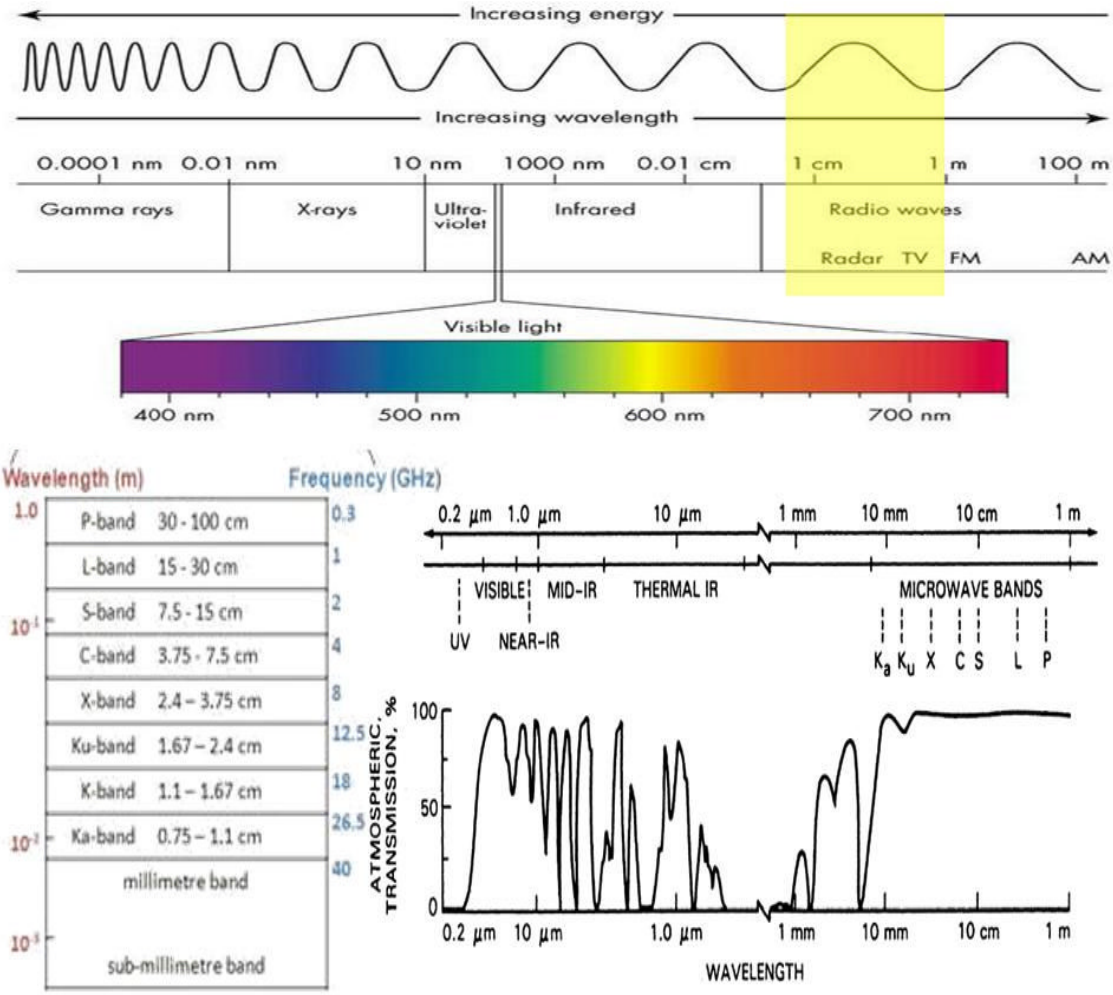

Figure 2.1 The electromagnetic spectrum include the visible light and the microwave region. This figure also shows the atmospheric penetration ability of the different wavelength

Table 2.1 Past, Current and Future Spaceborne SAR Systems

Name	Launched	Ended	Country	Band	Orbit Height (km)	Revisit (Days)
Seasat	1978	1978	USA	L-band	800	*
ERS-1	1991	2000	Europe	C-band	785	35
JERS-1	1992	1998	Japan	L-band	568	44
ERS 2	1995		Europe	C-band	780	35
Radarsat 1	1995		Canada	C-band	798	24
Space Shuttle SRTM	2000	2000	USA	X-band	233	*
Envisat ASAR	2002		Europe	C-band	800	3
RISAT	2006		India	C-band	609	13
ALOS	2006		Japan	L-band	700	46
Cosmo/Skymed (2+4x)	2006		Italy	X-band	619	14
SAR-Lupe	2006		Germany	X-band	500	**
JianBing-5	2007		China	L-band	628	**
Radarsat 2	2007		Canada	C-band	798	3
TerraSAR-X	2008		Germany	X-band	530	11
TecSAR	2008		Israel	X-band	580	**
TanDEM-X	2009		Germany	X-band	514	11
Kompsat-5	2009		South Korea	X-band	550	**
HJ-1-C	2009		China	S-band	500	**
Smotr	2010		Russia	X-band	650	**
Sentinel-1	2011		Europe	C-band	700	12
SAOCOM-1	2012		Argentina	L-band	659	**
MapSAR	2012		Brazil + Germany	L-band	620	**
ALOS-2	2012		Japan	L-band	700	**

Note: * Single mission, there is no revisiting location
** Not known the revisiting time due to the flexibility or still under planning

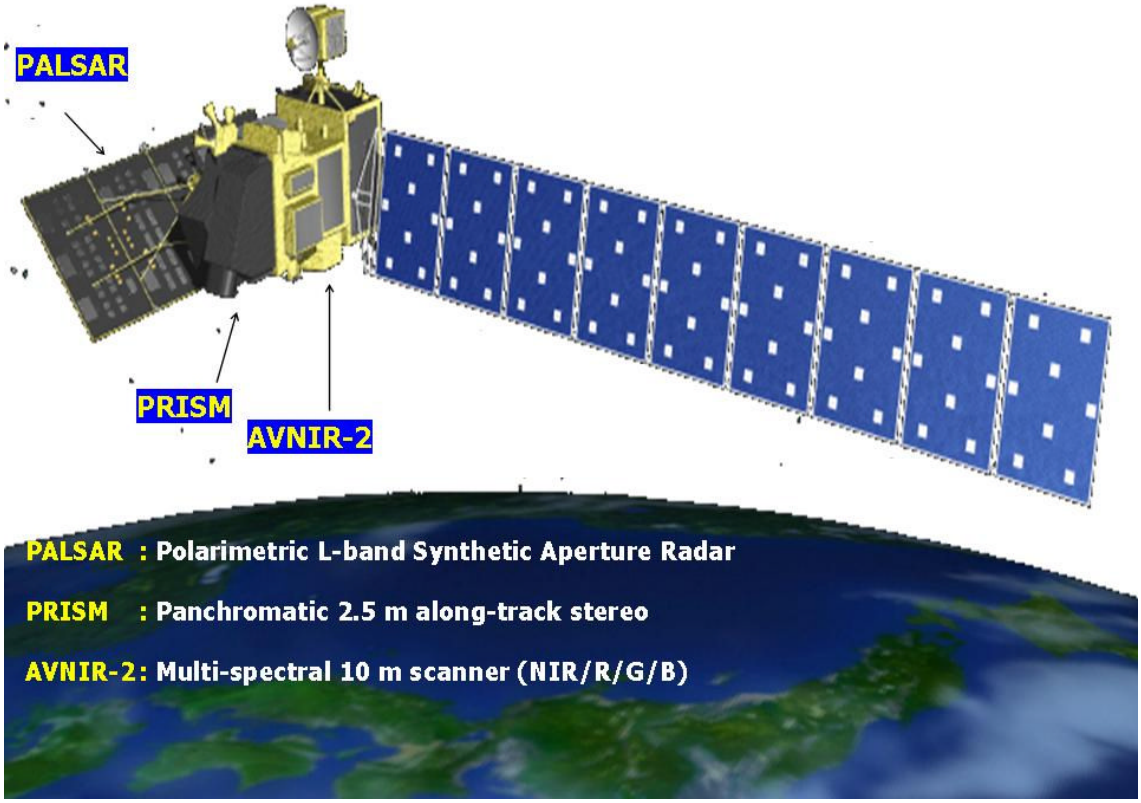

Figure 2.2 The illustration of ALOS satellite system completed with PALSAR, PRISM and AVNIR-2 sensors

Table 2.2 ALOS Characteristics (modified from Rosenqvist et al., 2007 and EORC, 2008)

Item	Specification / Characteristics
Spacecraft Mass	Approx. 4 tons
Solar Array Paddle	3 m x 22 m, 9 segments
Launch Date	24 January 2006
Launch Vehicle	H-IIA
Launch Site	Tanegashima Space Center
Orbit Type	Polar, Sun-Synchronous
Orbit Altitude (Above Equator)	691.65km
Orbit Inclination	98.16 (degree)
Recurrence Cycle	46 days (2 days sub-cycle)
Orbital Posistion Accuracy	0.78 m (off-line)
Attitude Determination Accuracy	2.0 x 10-4degree (with GCP)
Sensor Instruments	Panchromatic Remote-sensing Instrument for Stereo Mapping (PRISM) Wavelength (0.52-0.77 micrometers) radiometer, 2.5 m spatial resolution, swath width is 70 km in nadir-only mode
	Advanced Visible and Near Infrared Radiometer type 2 (AVNIR-2) AVNIR-2: multispectral radiometer - Band 1 (Red) : 0.42-0.50 micrometers - Band 2 (Green) : 0.52-0.60 micrometers - Band 3 (Blue) : 0.61-0.69 micrometers - Band 4 (Near Infrared) : 0.76-0.89 micrometers 10 m spatial resolution, swath: 70 km
	Phased Array type L-band Synthetic Aperture Radar (PALSAR) PALSAR: radar with 23.6 cm wavelength 4 - 100 m range resolution (depends on observation mode) swath area: 40 - 350 km (depends on observation mode)
Data Recording and Reproducing	High Speed Solid State Recorder (HSSR) 1 set -Recording capacity: over 96GB -Recording speed: 360/240/120Mbps (selectable) -Reproducing speed: 240/120Mbps (selectable) Low Speed Solid State Recorder (LSSR) 1 set -Recording capacity: 1GB (0.5GB x 2 partitions) -Recording speed: 40kbps -Reproducing speed: 16Mbps
Data Transmission	Ka-band antenna 277.52Msps / 240Mbps (DRTS) X-band antenna 138.76Msps / 120Mbps (Direct Transmission)

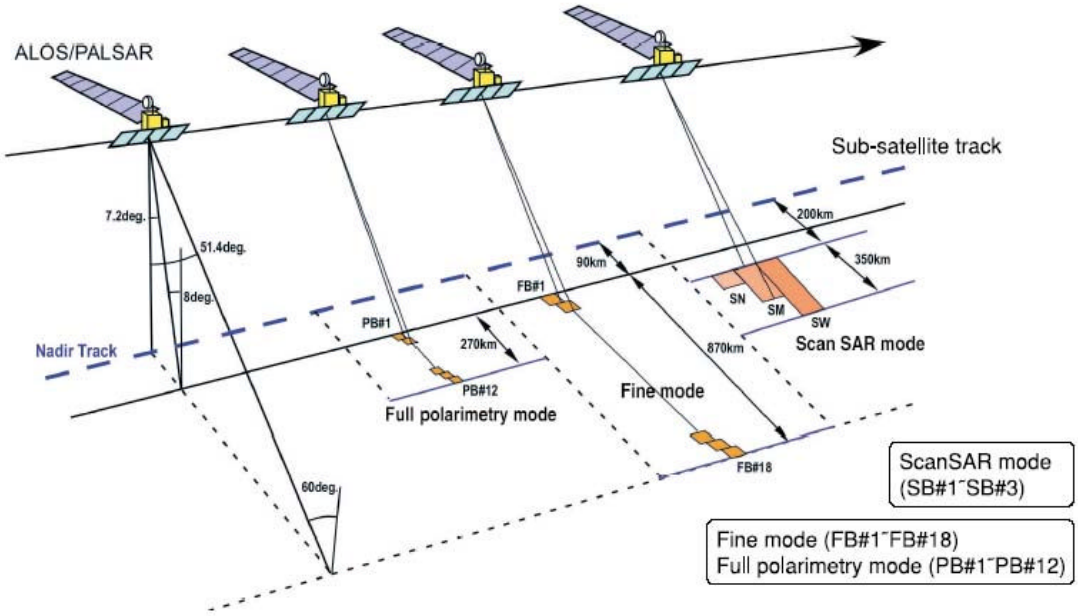

Figure 2.3 The PALSAR observation mode

Table 2.3 Summary of PALSAR Characteristics (modified from Rosenqvist et al., 2007 and EORC, 2008)

	Observation Mode				
	Fine Resolution		**ScanSAR**	**Polarimetric**	**Direct Downlink**
	Single Beam	**Double Beam**			
Center Frequency	1270 MHz(L-band)				
Chirp Bandwidth	28MHz	14MHz	14MHz, 28MHz	14MHz	14MHz
Polarization	HH or VV	HH/HV or VV/VH	HH or VV	HH/HV/VH/VV	HH or VV
Incidence angle	8 to 60deg.	8 to 60deg.	18 to 36deg 18 to 40deg 18 to 43deg.	8 to 30deg.	8 to 60deg.
Range Resolution	10 m*	20 m*	100m* (multi-look)	30 m*	20 m*
Azimuth Resolution	10 m	20 m	100m (multi-look)	10 m	10 m
Observation Swath	70 km*	70 km*	250 km 300 km 350 km	30 km*	70 km*
Bit Length	5 bits	5 bits	5 bits	3 or 5bits	5 bits
Data rate	240Mbps	240Mbps	120Mbps, 240Mbps	240Mbps	120Mbps
Radiometric accuracy	scene: 1dB / orbit: 1.5 dB				

Note: * For 34.3 degree Off-nadir (Fine Resolution, ScanSAR, Direct Downlink) and 21.5 degree for Polarimetric Mode.

Table 2.4 Summary of PALSAR Data Products

Product Level	Observation Mode	Polarization	Format	Data type	Data size of one pixel (sample)
Level 1.0 (Scene Length 70 km)	High resolution mode	1 polarization (HH/VV)	CEOS	8 bit unsigned integer	I and Q channel 8 bit unsigned integer 2 bytes in total for single polarization 4 bytes in total for 2 polarizations 8 bytes in total for 4 polarizations
		2 polarization (HH+HV/VV+VH)			
	Polarimetry mode	4 polarization (HH+HV+VH+VV)			
	ScanSAR mode	1 polarization (HH/VV)			
Level 1.1 (Scene Length 70 km)	High resolution mode	1 polarization (HH/VV)	EORC: CEOS format ERSDAC: Vexcel format	IEEE 32 bit floating point	Real and imaginary parts of complex number 8 bytes in total for single polarization 16 bytes in total for 2 polarizations 32 bytes in total for 4 polarizations
		2 polarization (HH+HV/VV+VH)			
	Polarimetry mode	4 polarization (HH+HV+VH+VV)			
Level 1.5 (Scene Length 70 km)	High resolution mode	1 polarization (HH/VV)	CEOS	16 bit unsigned integer	2 bytes
Level 4.1 (Scene Length 70 km)	High resolution mode	2 polarization (HH+HV/VV+VH)	CEOS	16 bit integer(signed and unsigned)	HH*HH', HV*HV', VV*VV' Real number Unsigned integer (2 byte) HH*HV', HH*VV', VV*HV' Complex number Real and imaginary parts Signed integer (2 byte) 8 bytes in total for 2 polarizations 18 bytes in total for 4 polarizations
	Polarimetry mode	4 polarization (HH+HV+VH+VV)			
Level 4.2 (Scene Length 300 km)	ScanSAR mode 3 scans	1 polarization (HH/VV)	CEOS	16 bit unsigned integer	2 bytes
	ScanSAR mode 4 scans	1 polarization (HH/VV)			
	ScanSAR mode 5 scans	1 polarization (HH/VV)			

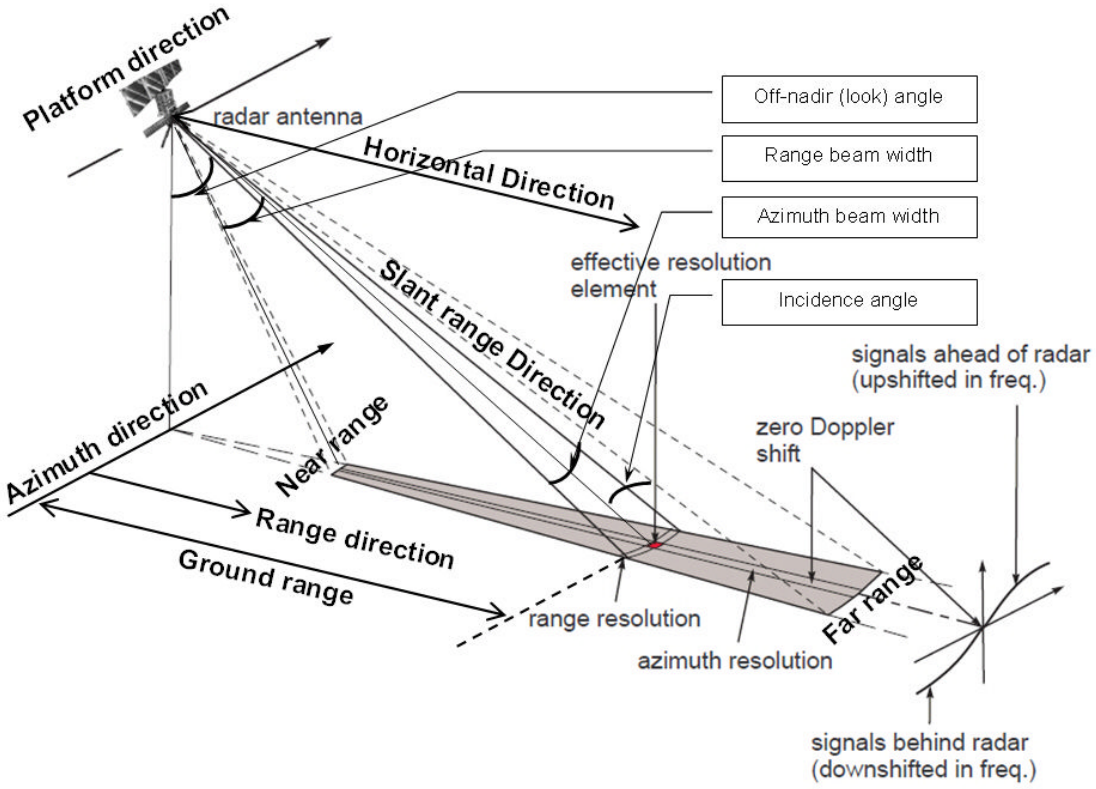

Figure 3.1 The Geometric Configuration of Satellite SAR System

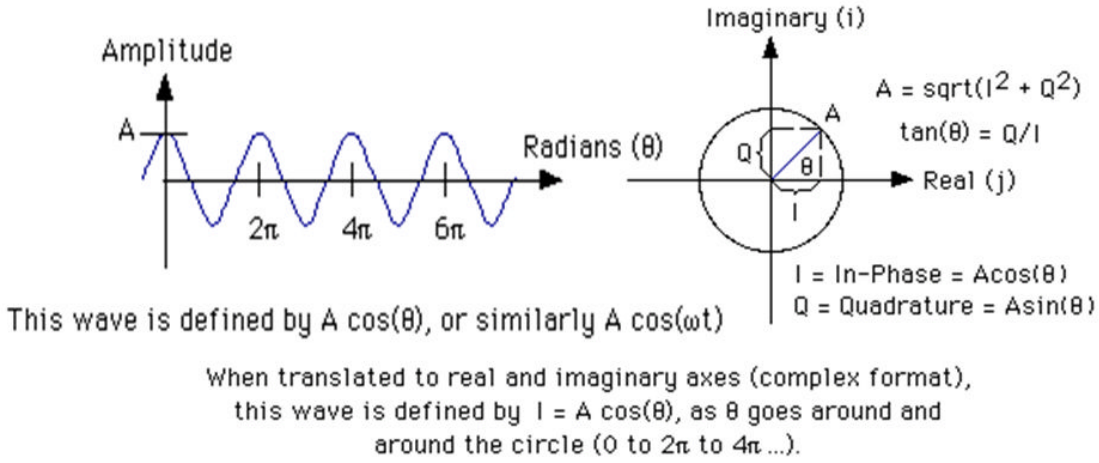

Figure 3.2 The SAR IQ (In-Phase and Quadrature) Data Format

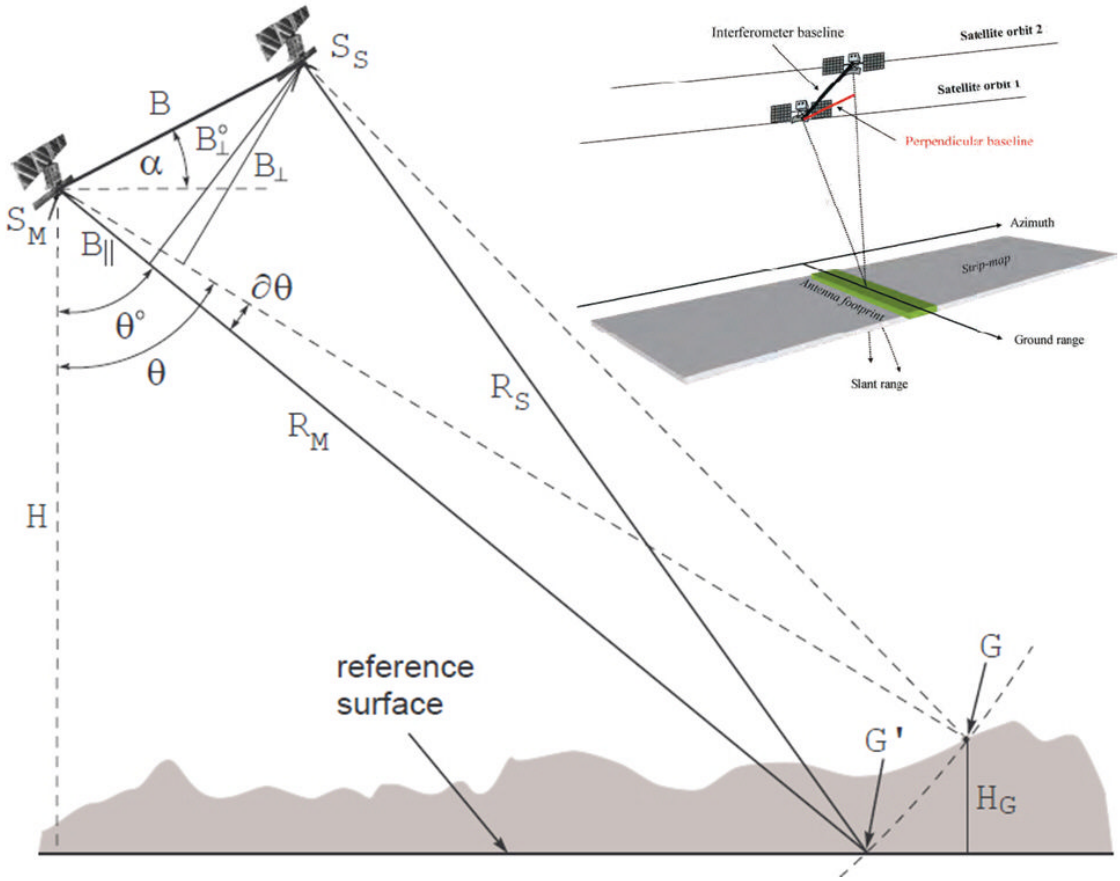

Figure 3.3 The Geometry of InSAR

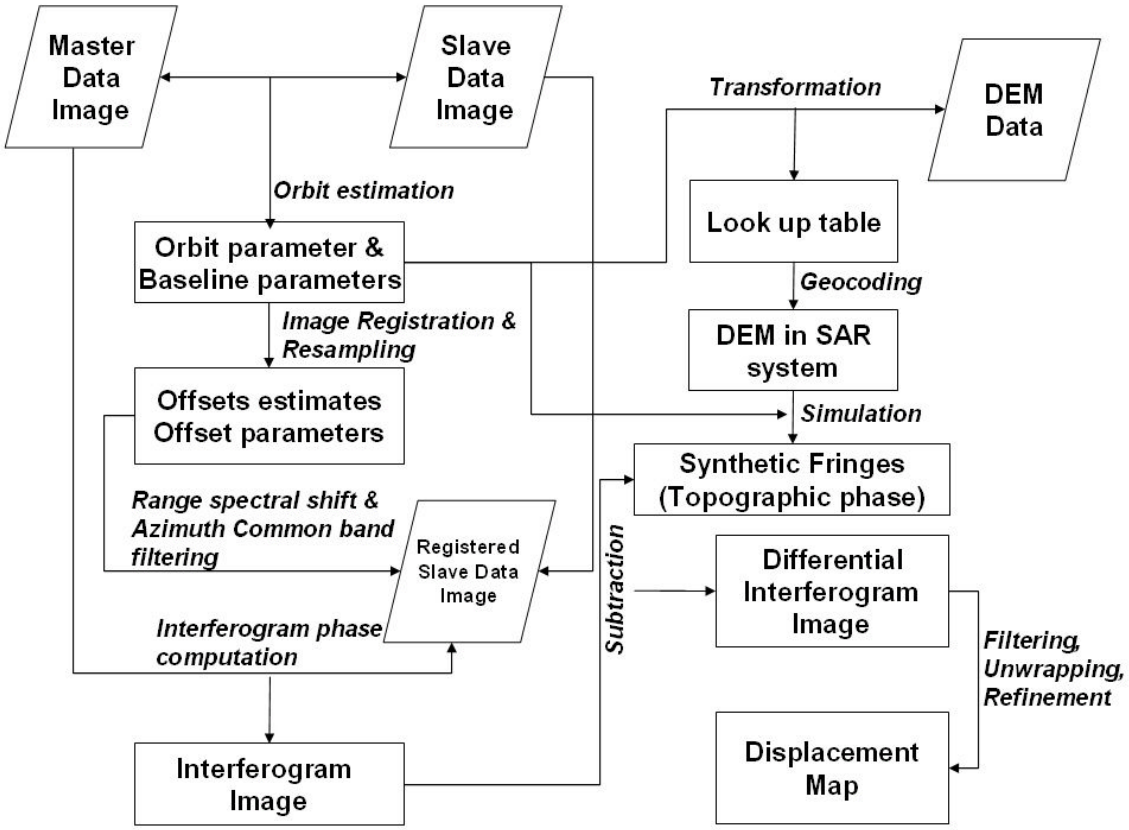

Figure 3.4 The Processing Chain of DInSAR

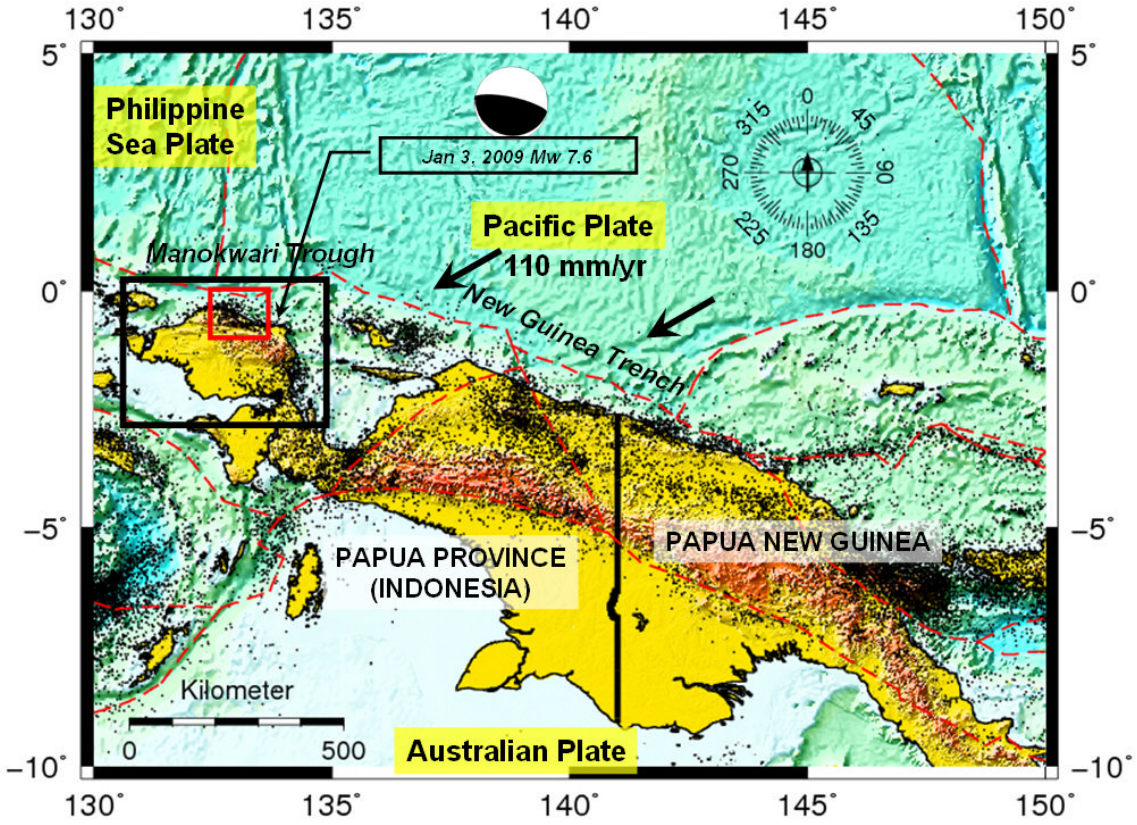

Figure 4.1 The New Guinea Island. Region in black box represents the Bird's Head area or Kepala Burung in Indonesian term, whereas the red box represents the PALSAR coverage area for this study. Red dashed line illustrates the plate boundary based on Bird (2003).

Table 4.1 The Image Parameters of PALSAR data for Papua Region

	Epoch 1 (Master)	**Epoch 2 (Slave)**
Date	14 October 2008	14 January 2009
Range Samples	9280	9344
Azimuth Lines	18432	18432
Image Geometry	Slant range	Slant range
Center Latitude (deg):	-0.5727338	-0.573587
Center Longitude (deg):	132.5682473	132.5695218
Heading (deg):	-11.9674104	-11.9557149
Range Pixel Spacing (m):	4.684257	4.684257
Azimuth Pixel Spacing (m):	3.182244	3.182252
Near Range SLC (m):	847016	846866
Center Range SLC (m):	868748.6104	868748.5073
Far Range SLC (m):	890481.2207	890631.0146
Incidence Angle (deg):	38.8151	38.8222
Chirp Bandwidth (Hz):	1.40E+07	2.80E+07
Receiver Gain (dB):	24	24

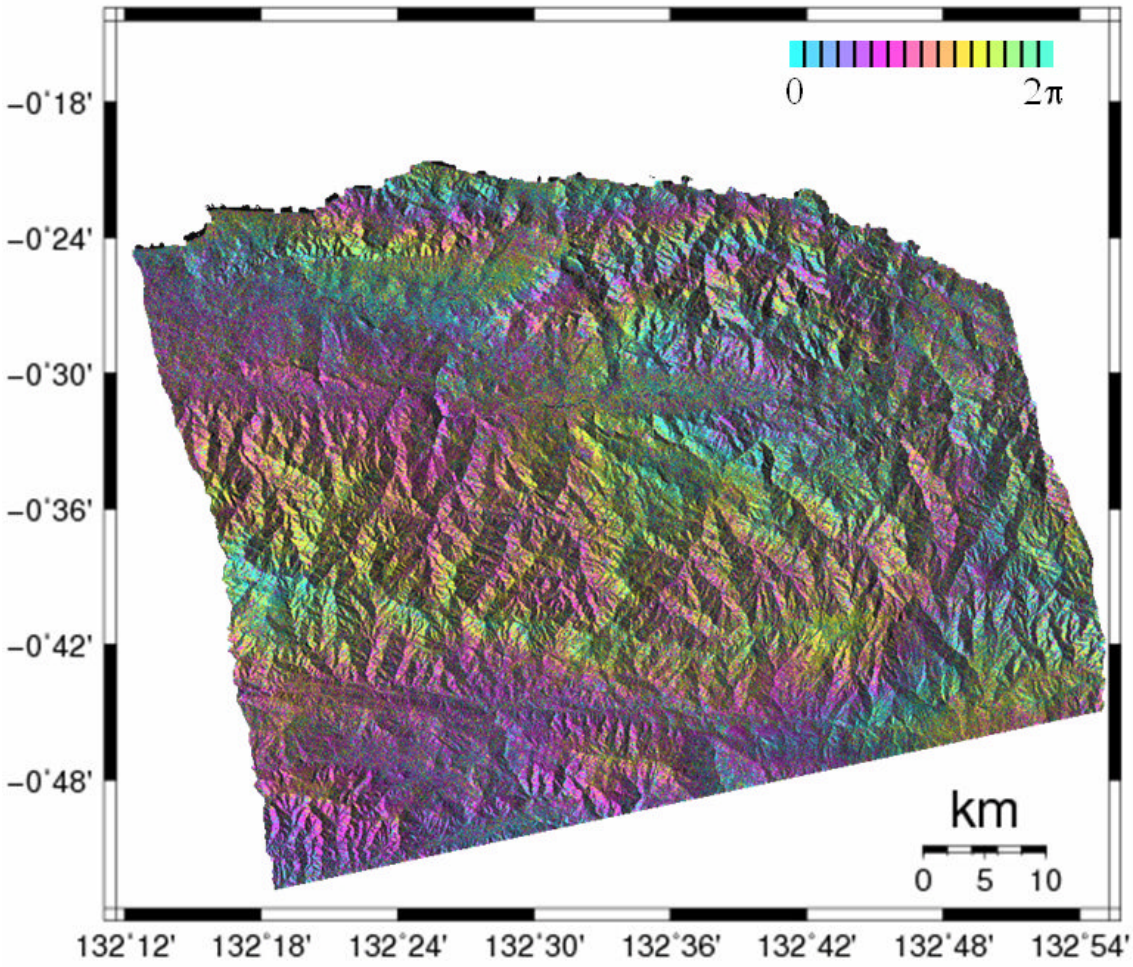

Figure 4.2 The Flattened Interferogram for Manokwari Region. This image shows an interferogram phase overlaid with the backscattered (amplitude) image.

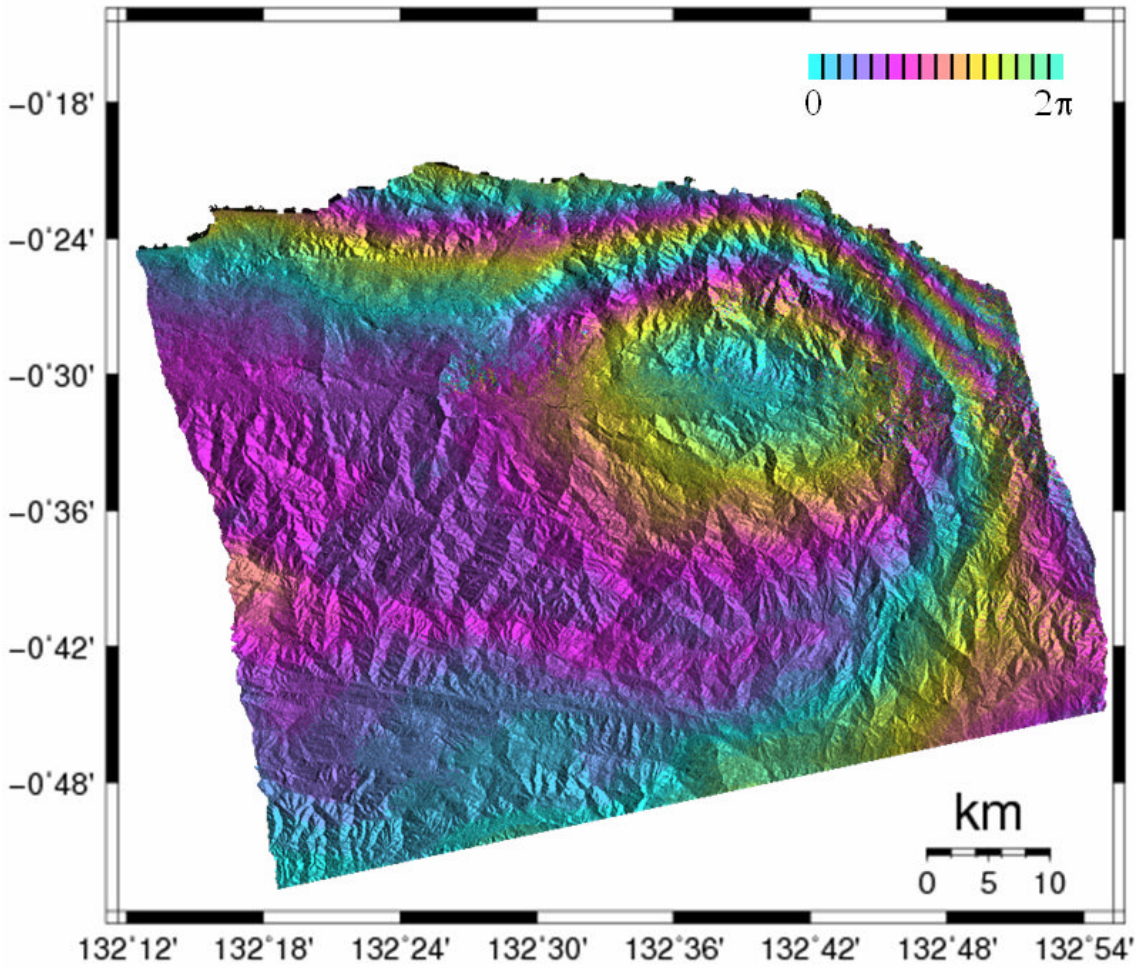

Figure 4.3 The Filtered Phase of Manokwari Region. This image shows an interferogram phase overlaid with the backscattered (amplitude) image.

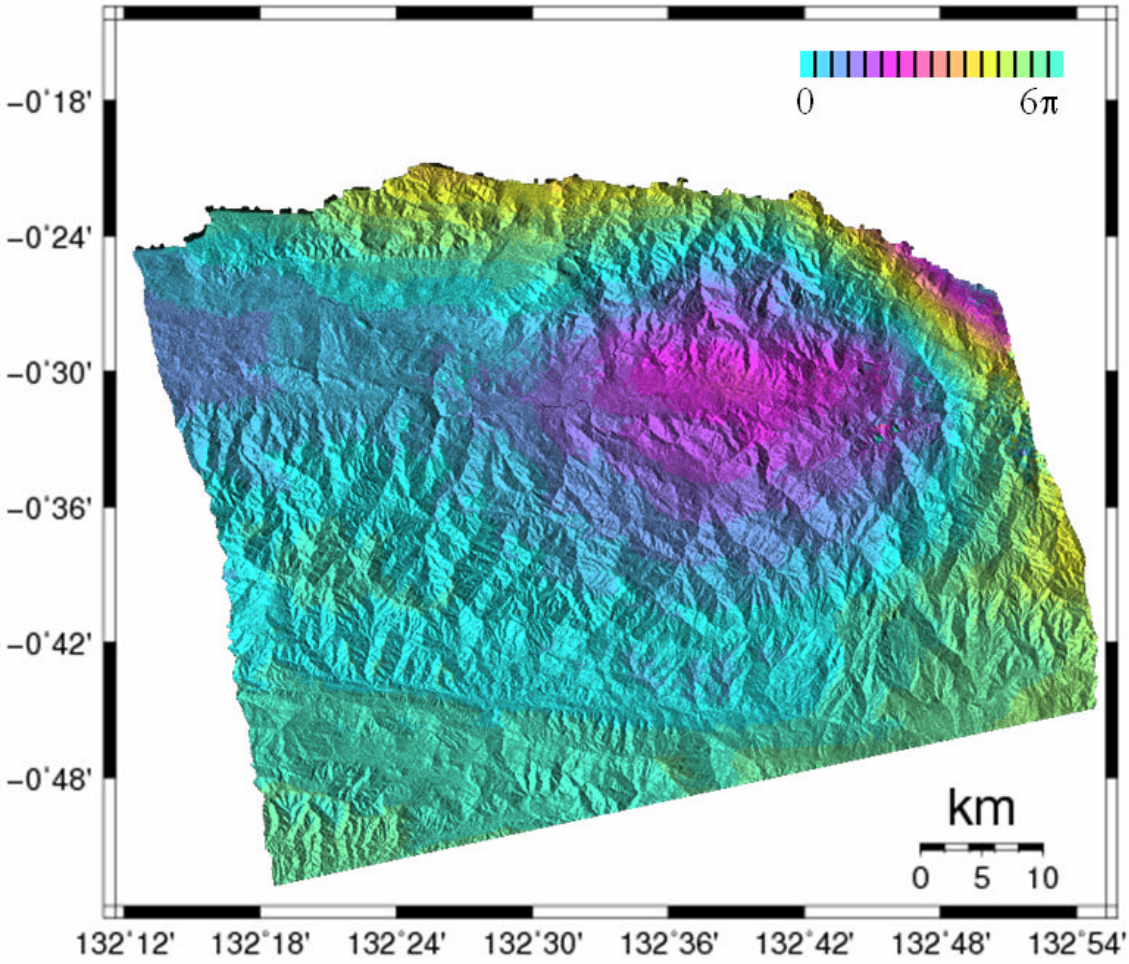

Figure 4.4 The Unwrapped Deformation Phase of Manokwari Region. This image shows an interferogram phase overlaid with the backscattered (amplitude) image.

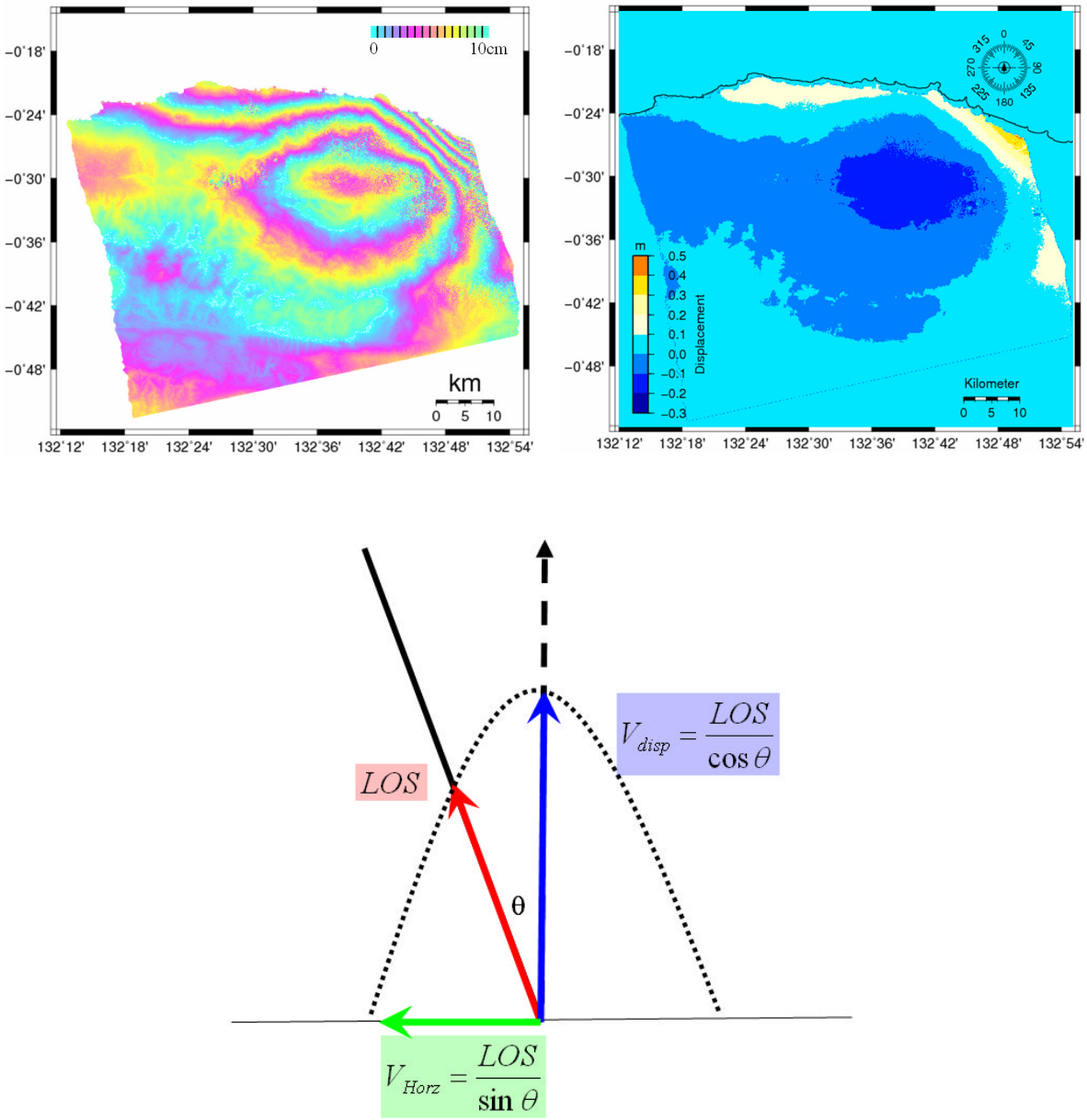

Figure 4.5 Map of Vertical Displacements of Papua Earthquake. The left figure illustrates the vertical component of line of sight displacement wrapped in 10 cm color cycle, whereas the right figure illustrates the vertical component of line of sight displacement in two-dimensional map. The bottom part illustrates the relation between line of sight displacement and possible true ground deformation in vertical and horizontal components

Table 4.2 The Discrepancy of Fault Parameter Model of Papua Earthquake

Parameter	USGS (2009)	Yamanaka (2009)	InSAR (Model)
Length (km)	60	105	72
Width (km)	30	50	28
Depth (km)	29	15	13
Strike (deg)	112	107	107
Dip (deg)	36	24	32
Rake (deg)	77	58	90
Slip (m)	5	2.7	2.5
Mw	7.6	7.6	7.4

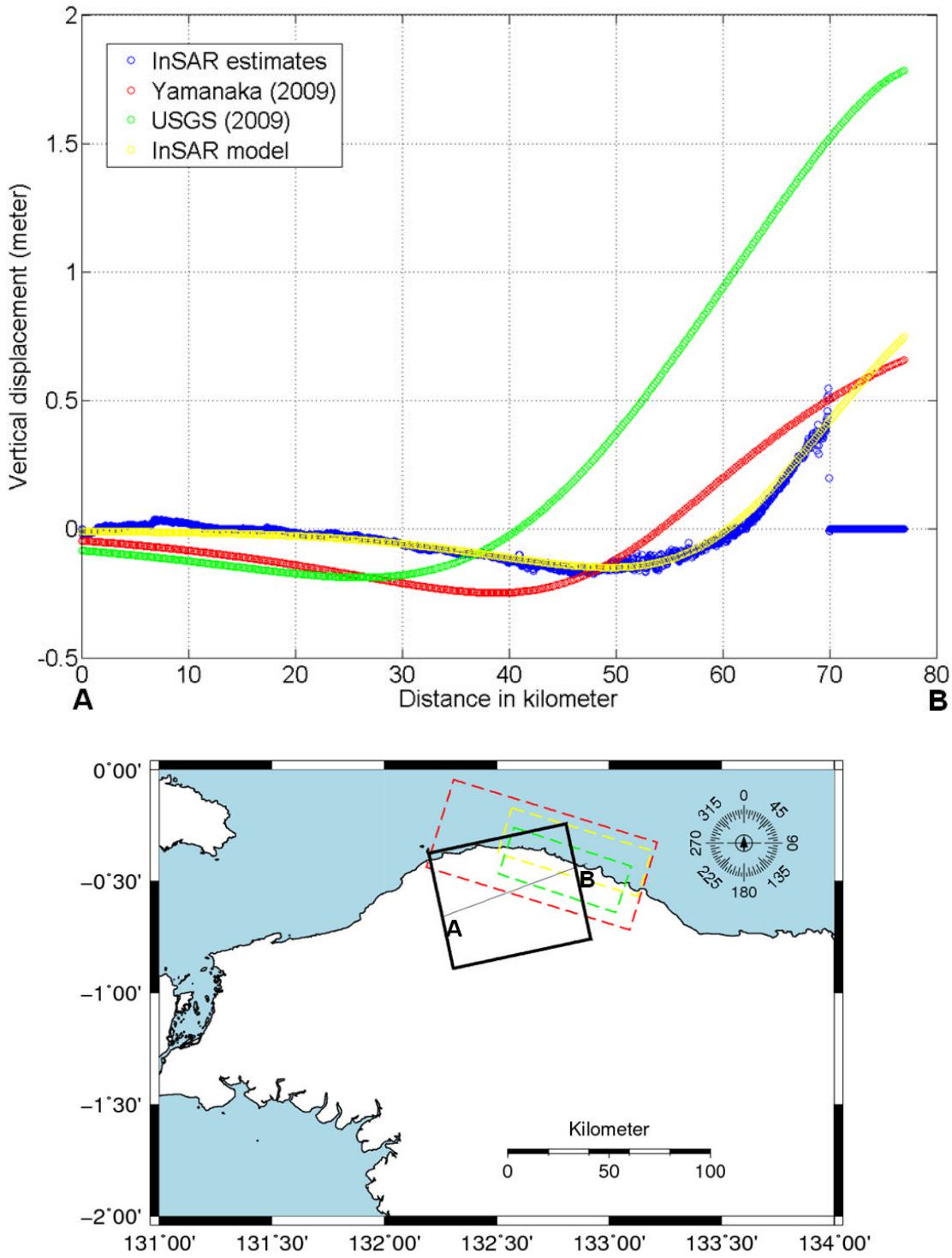

Figure 4.6 Comparison of Vertical Displacement Profiles of Papua Earthquake. Bottom part illustrates the fault geometry and line profile A-B that is used to extract profile from deformation derived from different models: red dashed line based on Yamanaka (2009), green dashed line based on USGS (2009) and yellow dashed line based on InSAR estimates model. The black solid line illustrates the PALSAR coverage area.

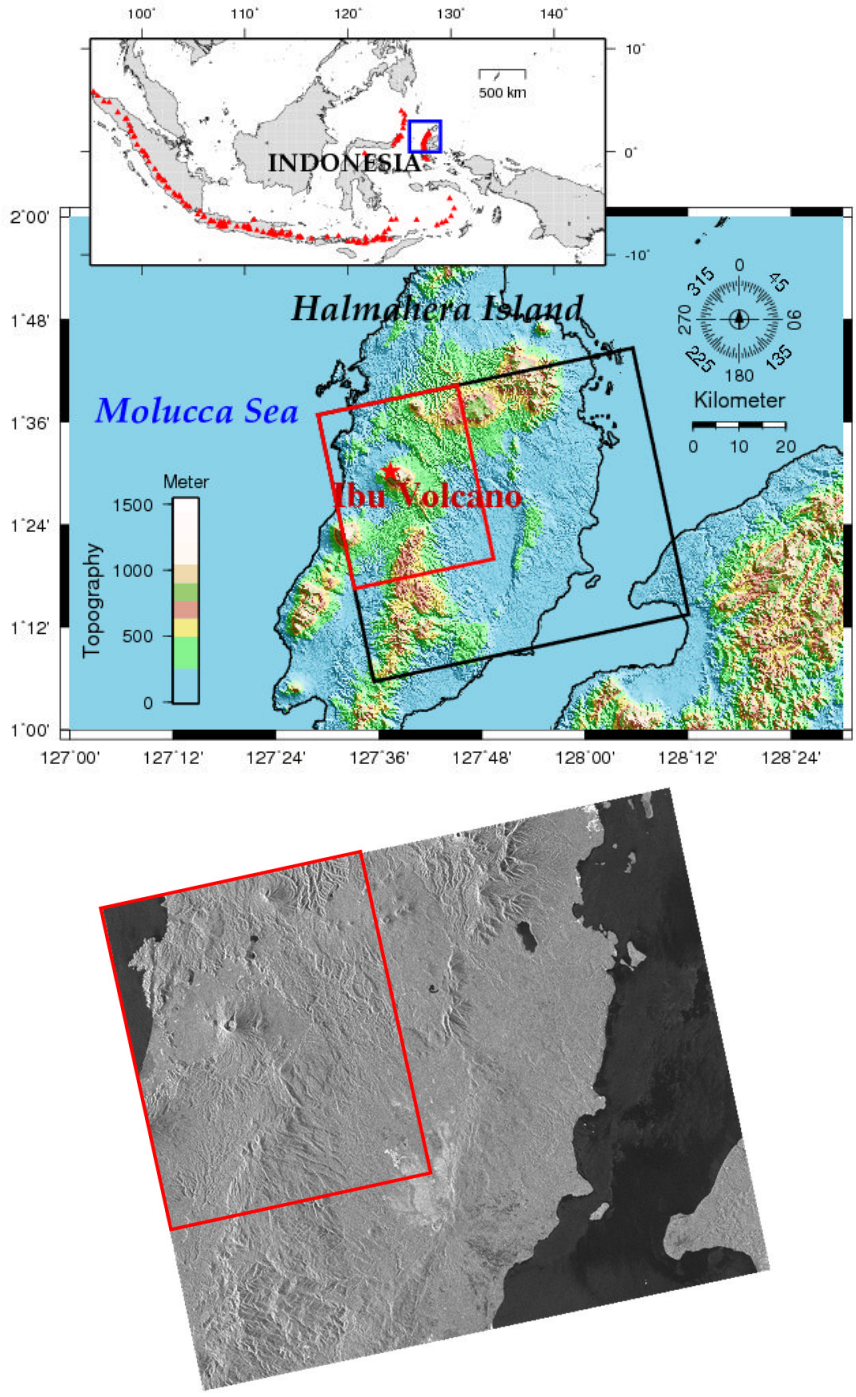

Figure 5.1 The Location of Ibu Volcano. Inset map shows the study area (blue square) with Indonesian map and volcanoes (red triangles). The area inside the black line illustrates the PALSAR coverage for one scene for Ibu region whereas the area that covered by the red line is the cropped region that is analyzed for this study. The PALSAR image is shown in the bottom part.

Table 5.1 The Description of Ibu Volcano PALSAR Data Sets

Parameter	Value
Frequency, (GHz)	1.270
Wavelength, (m)	0.23605705
Sampling frequency, (Hz)	3.2×10^7
Pulse repetition frequency, (Hz)	2155.172414
Pulse length, (μs)	27
Chirp bandwidth, (MHz)	28 (FBS mode) 14 (FBD mode)
Number of range samples	9344 (FBS mode) 4640 (FBD mode)
Number of lines	18432 (FBS and FBD modes)
Range resolution, (m)	~7.495 (FBS mode) ~14.99 (FBD mode)
Range pixel spacing, (m)	~4.68 (FBS mode) ~9.36 (FBD mode)
Typical slant range to center, (km)	~856
Azimuth resolution, (m)	~4
Azimuth pixel spacing, (m)	~3
Swath width, (km)	~43.47
Typical incidence angle, (deg)	~38.8
Typical look angle, (deg)	~34.3

Table 5.2 Interferogram Baseline of Ibu Volcano PALSAR Data Sets

Interferogram	**20070825 FBD**	**20071010 FBD**	**20080110 FBS**	**20080225 FBS**	**20080411 FBS**	**20080712 FBD**
A	M ● → S Δt = 46 days, $B_\perp$ = 112 m					
B		M ● → S Δt = 92 days, $B_\perp$ = 91 m				
C			M ● → S Δt = 46 days, $B_\perp$ = 66 m			
D				M ● → S Δt = 46 days, $B_\perp$ = 99 m		
E					M ● → S Δt = 92 days, $B_\perp$ = 421 m	

Observation epoch of PALSAR data, and their interferogram completed with time difference information (Δt) and perpendicular baseline ($B_\perp$). M indicates master image, whereas S is slave image

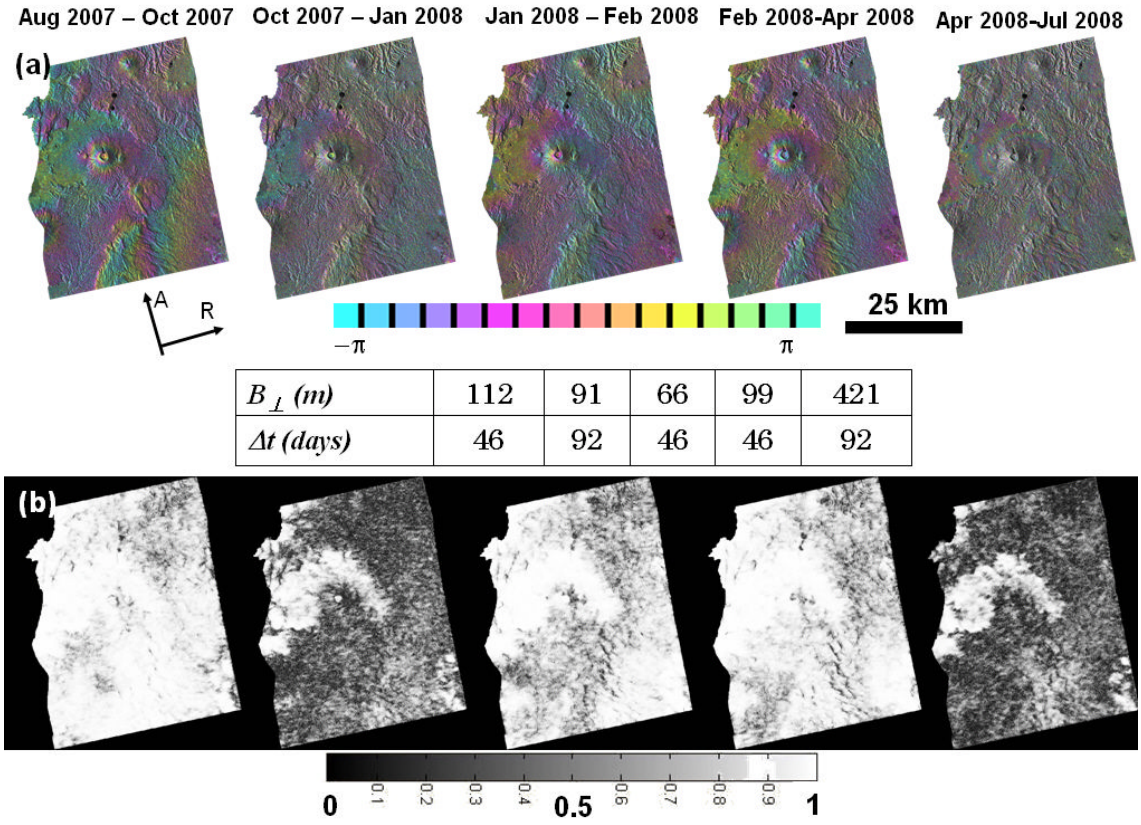

$B_{\perp}$ *(m)*	112	91	66	99	421
Δt *(days)*	46	92	46	46	92

Figure 5.2 The Flattened and Coherence Interferogram for Ibu Volcano. (a) The interferogram after flattening. (b) The coherence, from August 2007 to July 2008. A indicates the azimuth direction, R is range direction, Δt and $B_{\perp}$ are time and perpendicular baselines for each interferogram respectively.

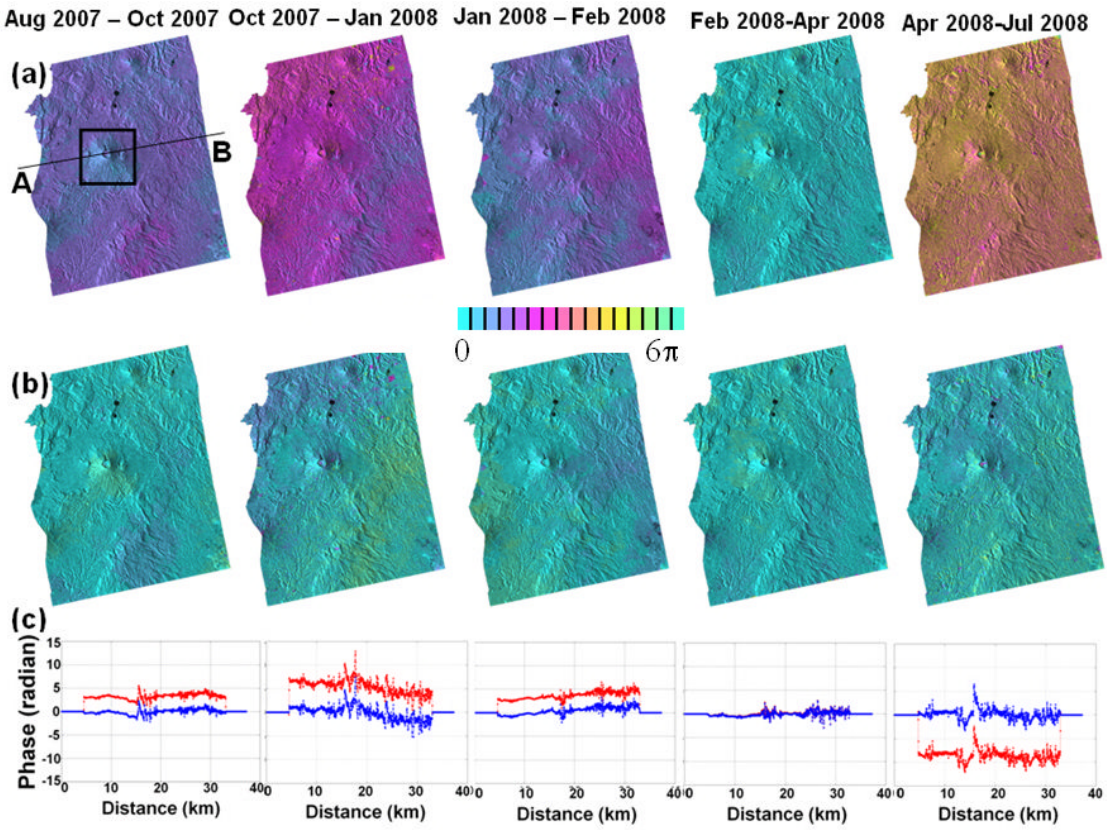

Figure 5.3 The Unwrapping Differential Phase for Ibu Volcano. (a) The unwrapped differential phase before applying a linear height dependent atmospheric phase (b) The unwrapped differential phase after applying a linear height dependent atmospheric phase (c) Comparison profiles along line A-B for each interferogram with red dots for the unwrapped differential phase whereas blue dots for the unwrapped differential phase after applying a linear height dependent atmospheric phase. Area marked by a square is the focus of deformation assessment.

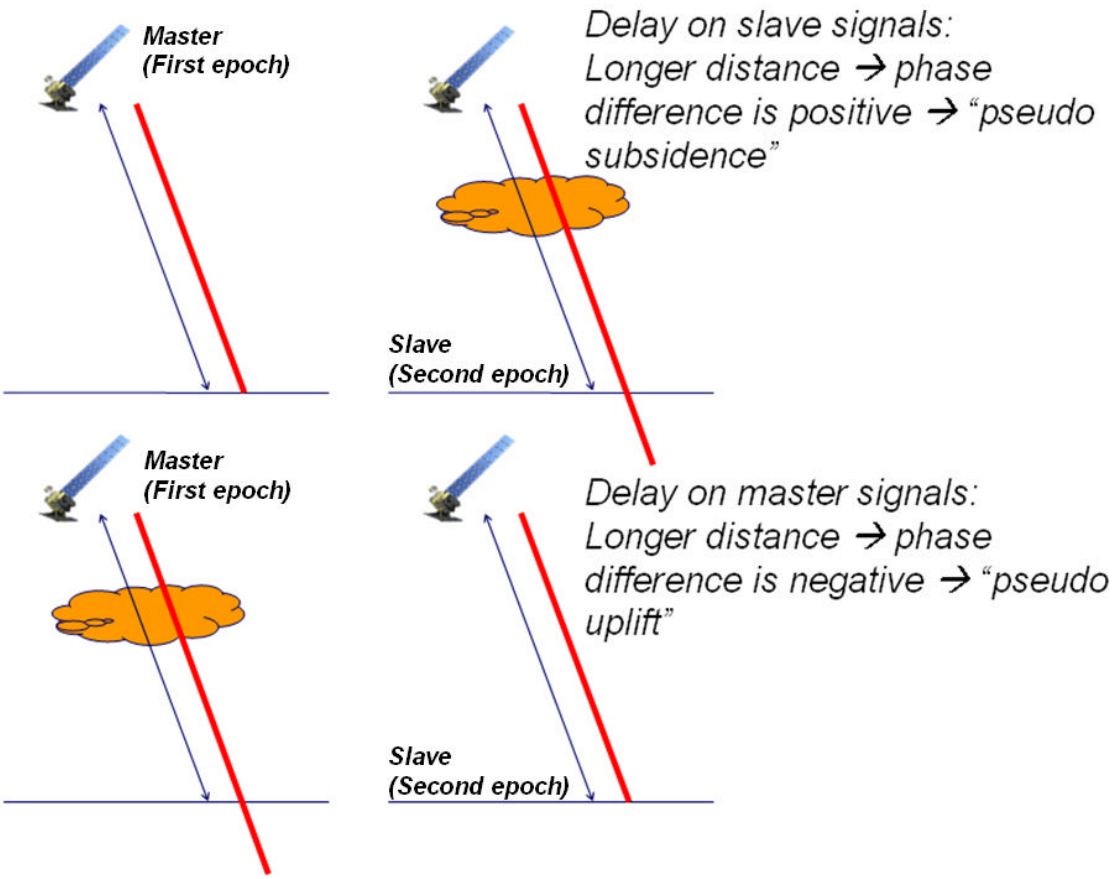

Figure 5.4 The Effect of the Atmospheric Delay to Interferogram. The blue line illustrates the true range from satellite to the target, whereas the red line is the real range observed from satellite to the target.

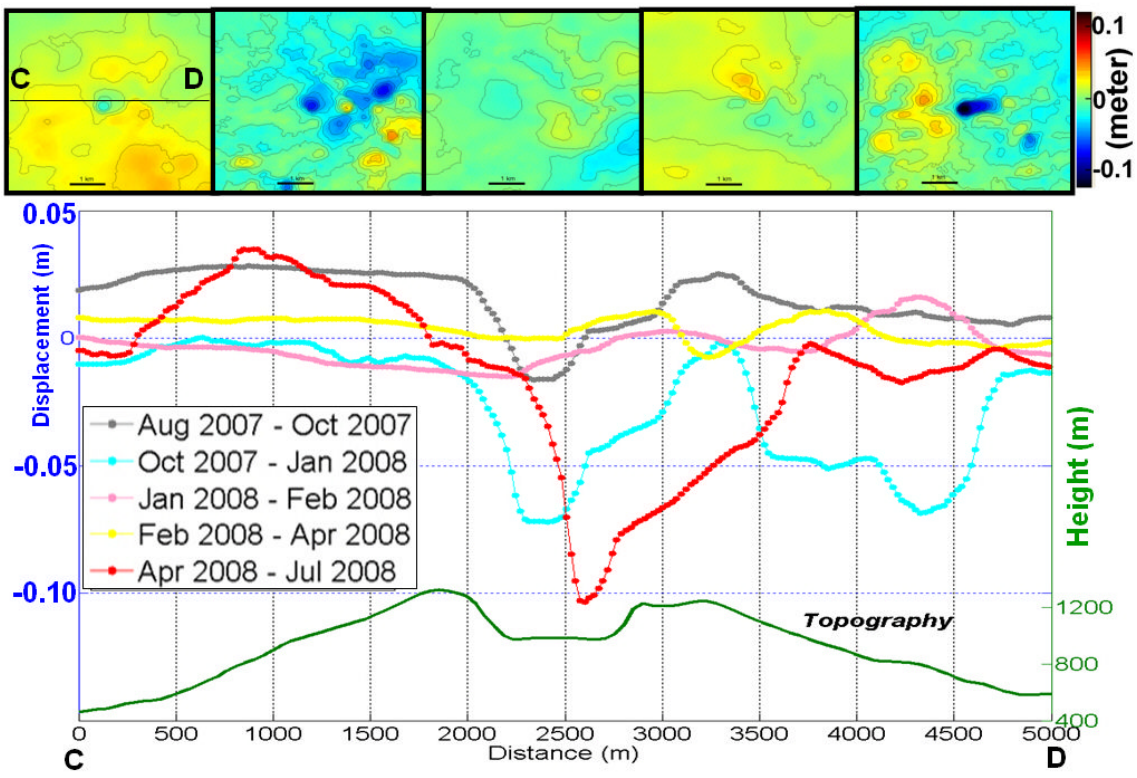

Figure 5.5 The Deformation of Ibu Volcano. Upper part illustrates the vertical displacement maps, with 1 cm contour interval for period (a) August to October 2007, (b) October 2007 to January 2008, (c) January 2008 to February 2008, (d) February to April 2008, and (e) April to July 2008. Lower part illustrates the corresponding profiles along line C-D on vertical displacement maps.

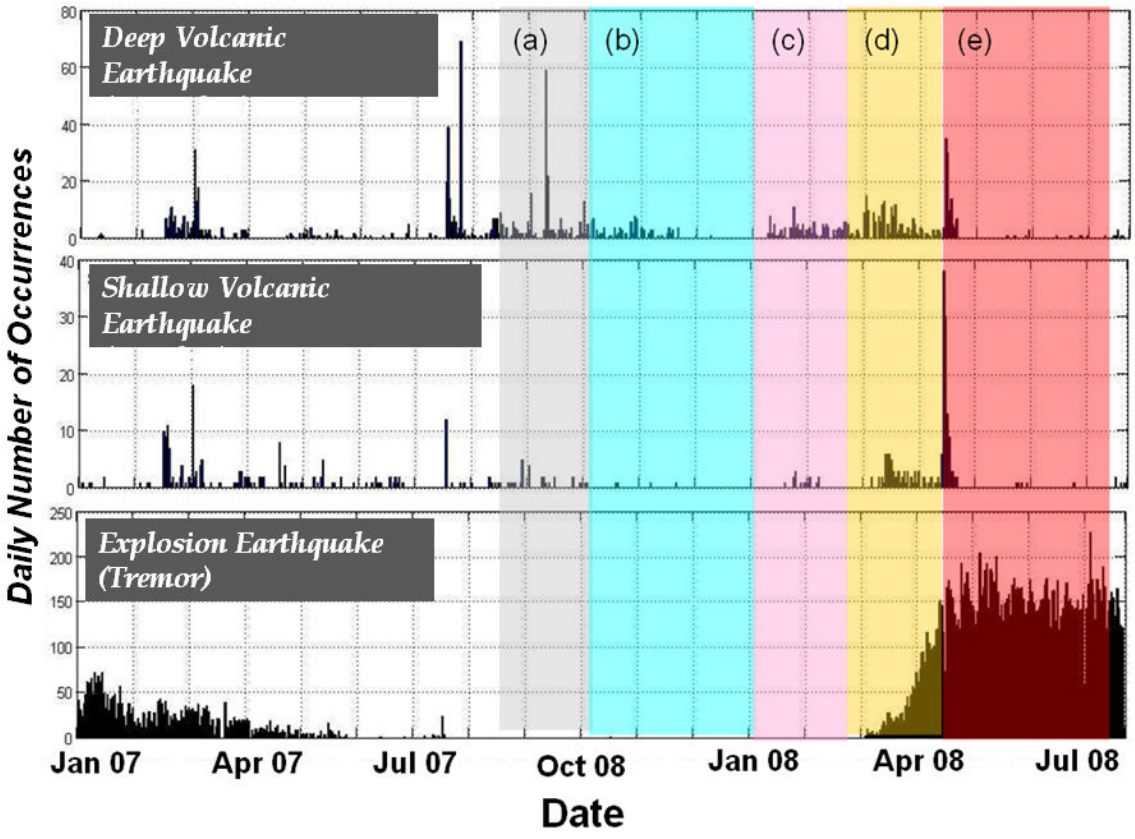

Figure 5.6 Daily Number of Earthquake for Ibu Volcano. The three types of seismic data: deep, shallow and explosion related to volcanic earthquake recorded from January 2007 to August 2008 for Ibu Volcano and corresponding interferograms in Figure 5.5. Data obtained from the Center of Volcanology and Geological Hazard Mitigation, Indonesia.

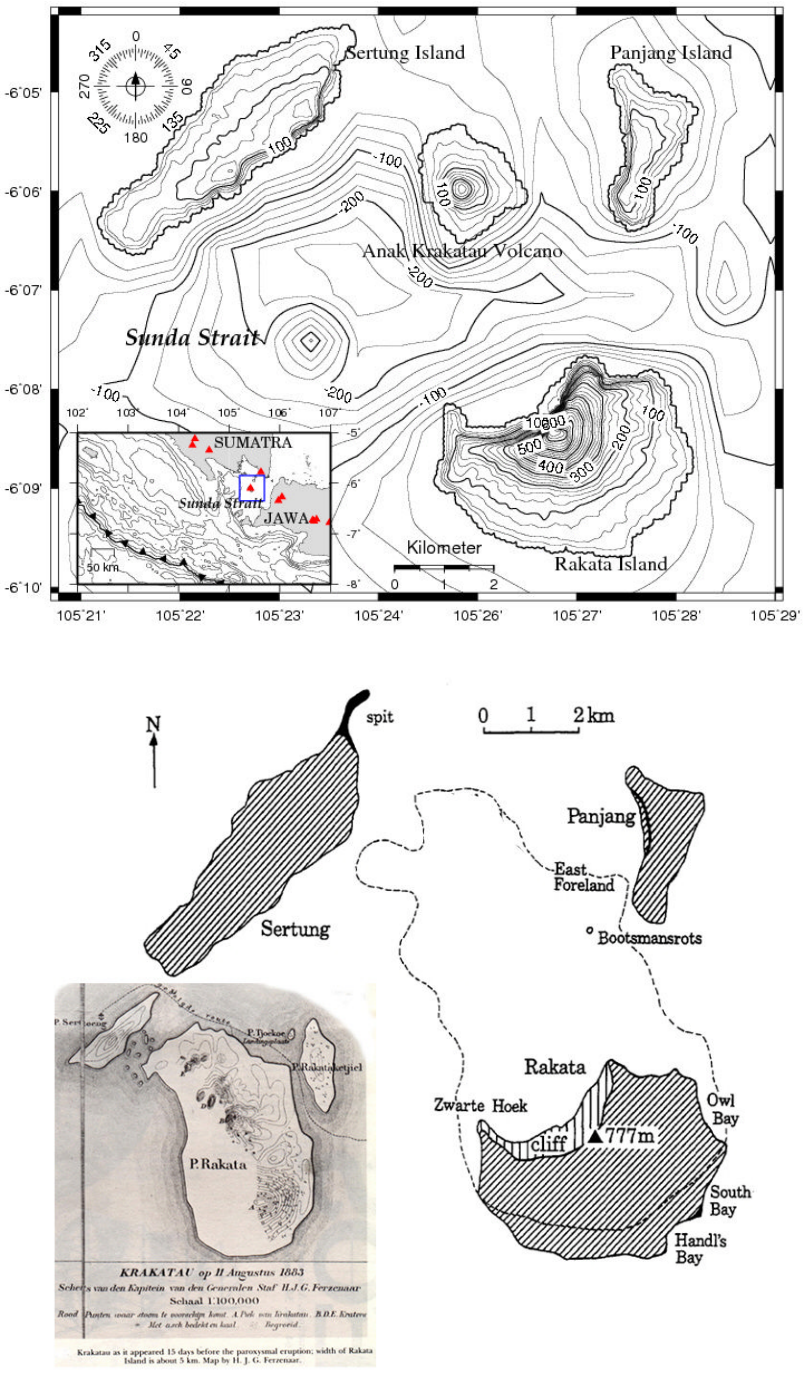

Figure 6.1 The location of Anak Krakatau Volcano. This figure illustrates the location of Anak Krakatau Volcano with 25 meter contour line. Inset map shows the study area (blue square) and 500 m interval bathymetry map of Sunda Strait, and volcanoes distribution (red triangles) in part of Sumatra and Java Island. Lower part illustrates the Krakatau Complex before (by Captain H. J. G. Ferzenaar) and after 1883 eruption (Souce: modified from Winchester, 2003 and Thornton et al., 1992)

Table 6.1 Summary of PALSAR Data Sets for Anak Krakatau Volcano

ΔT / $B_{\perp}$	**20070623 FBD 1.0**	**20070903 FBD 1.0**	**20080208 FBS 1.1**	**20080925 FBD 1.1**	**20090210 FBS 1.1**
20070623		92 days	230 days	460 days	598 days
20070903	344 m		138 days	368 days	506 days
20080208	262 m	82 m		230 days	368 days
20080925	750 m	1093 m	1010 m		138 days
20090210	489 m	833 m	751 m	260 m	

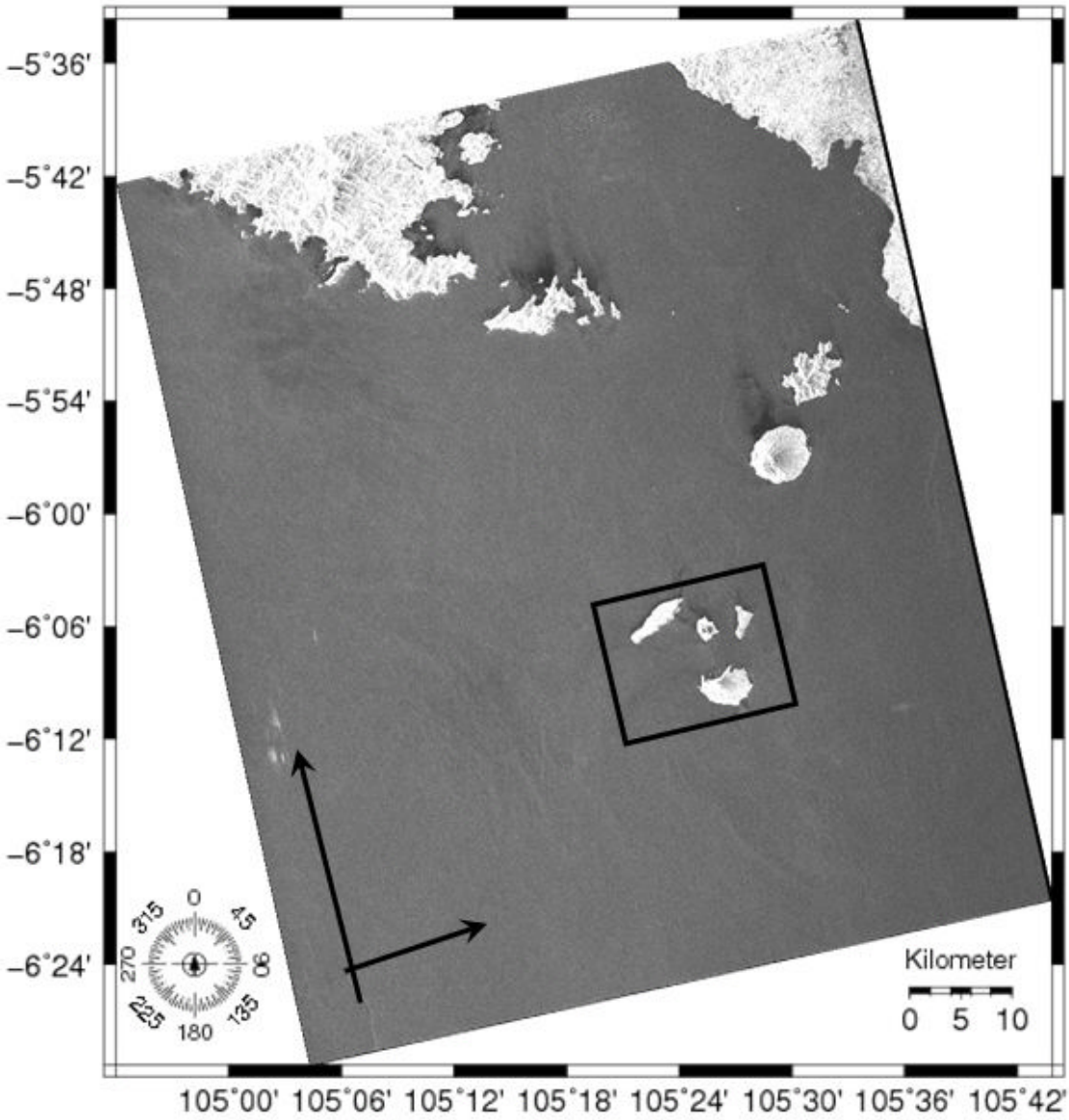

Figure 6.2 The SLC Image for Krakatau Area. The black square line illustrates the Krakatau Complex that was analyzed in this study.

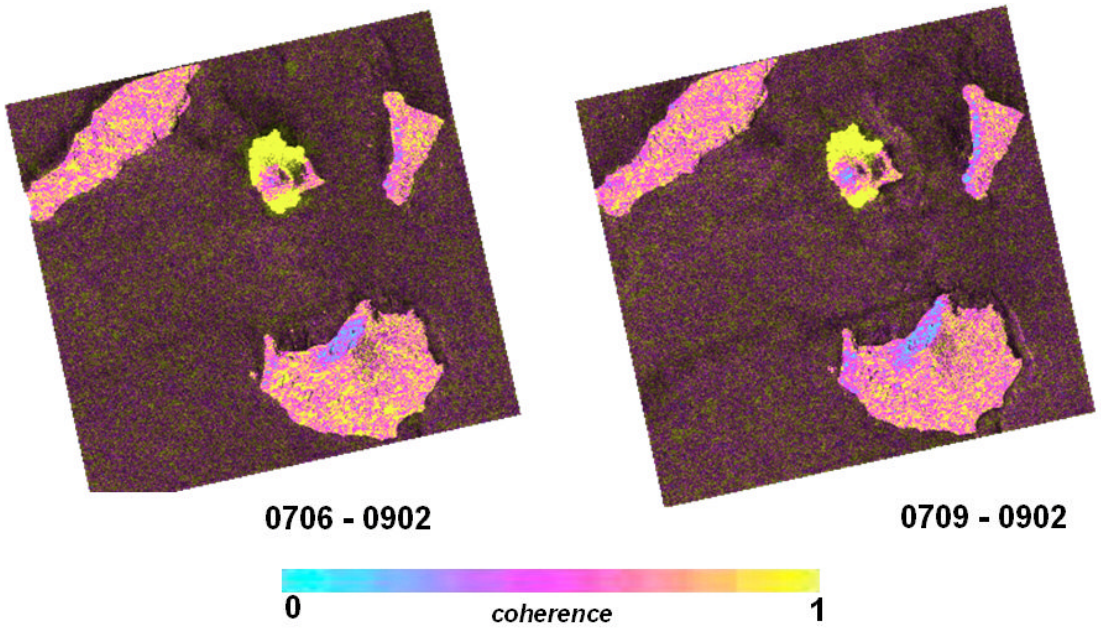

Figure 6.3 The Comparison of Coherence in Master Selection for Anak Krakatau Volcano. The left figure illustrates the coherence between June 2007 and February 2009, whereas the right figure illustrates the coherence between September 2007 to February 2009. The yellow color indicates the high coherence area, that representing value more than 0.7 in the scale from 0 to 1.

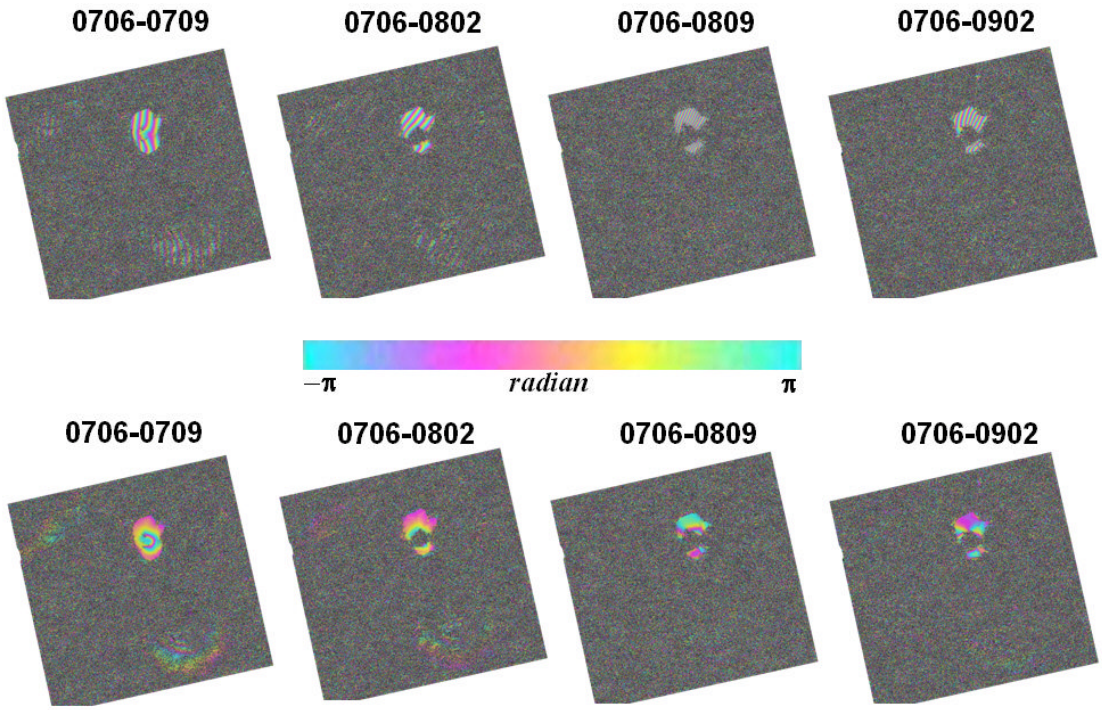

Figure 6.4 Series of the interferogram and the flattened of Anak Krakatau Volcano.

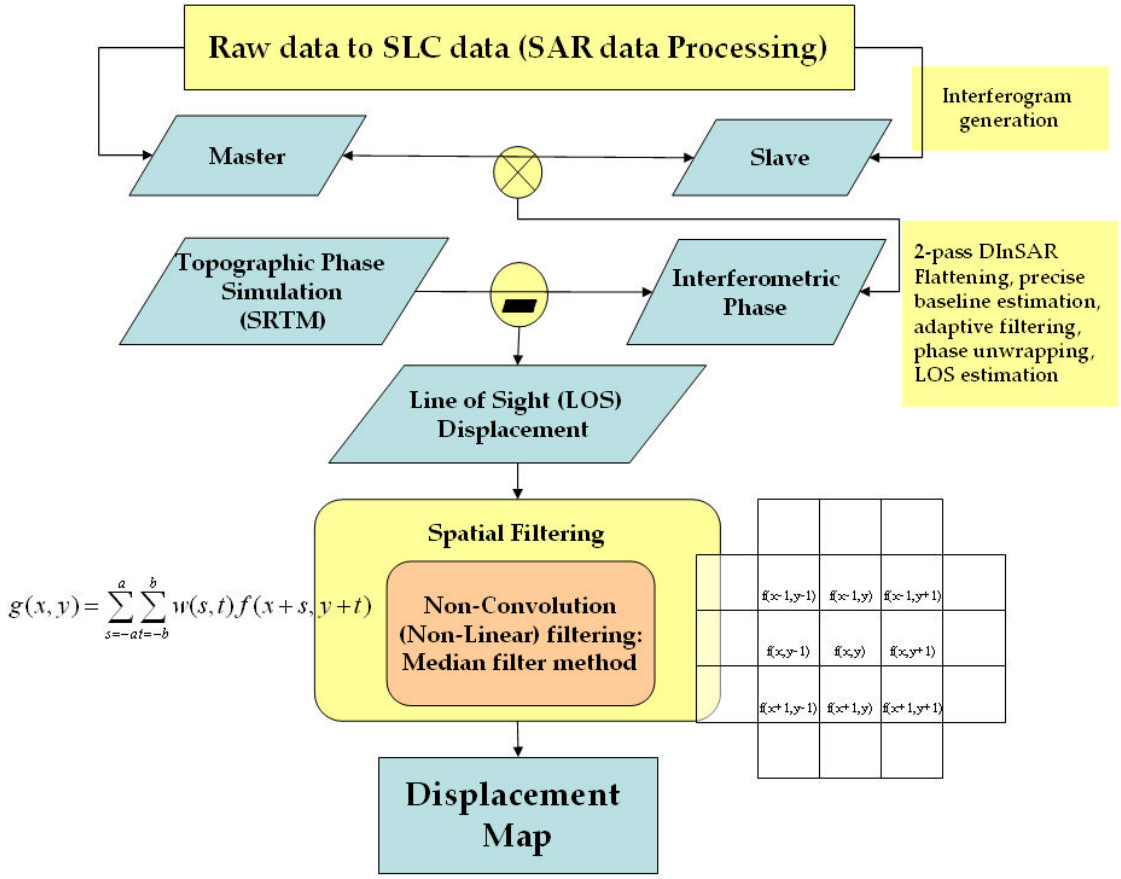

Figure 6.5 The Processing Chain of Post-Processed Filtered Strategy.

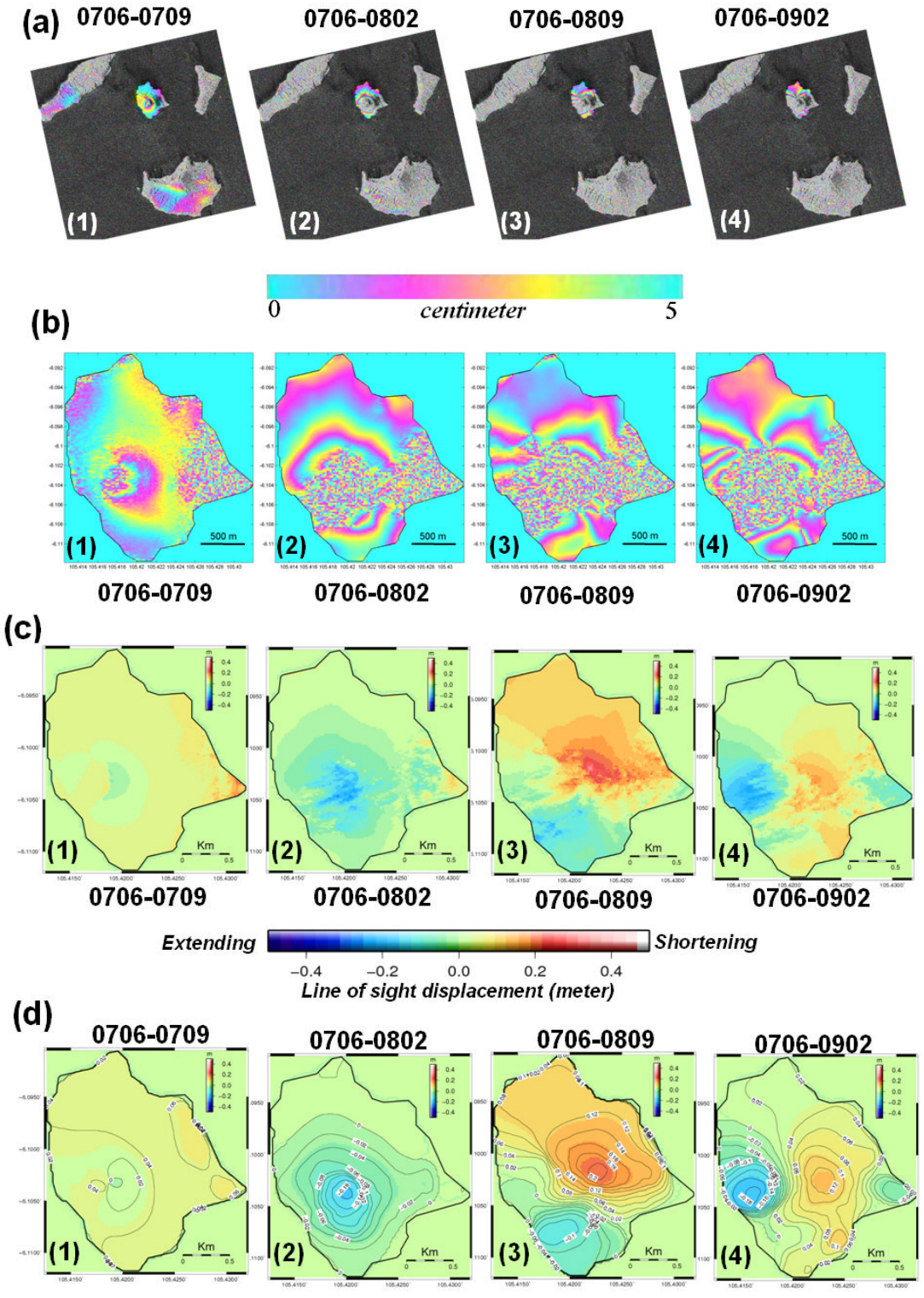

Figure 6.6 Series of Line of Sight (LOS) Displacement of Anak Krakatau. (a) LOS displacement for whole image wrapped in 5 cm, and focusing in Anak Krakatau (b). LOS displacement converted to grid data format (c) and after applying Post-Processed Filtering Strategy to obtain the smoothed grids (d).

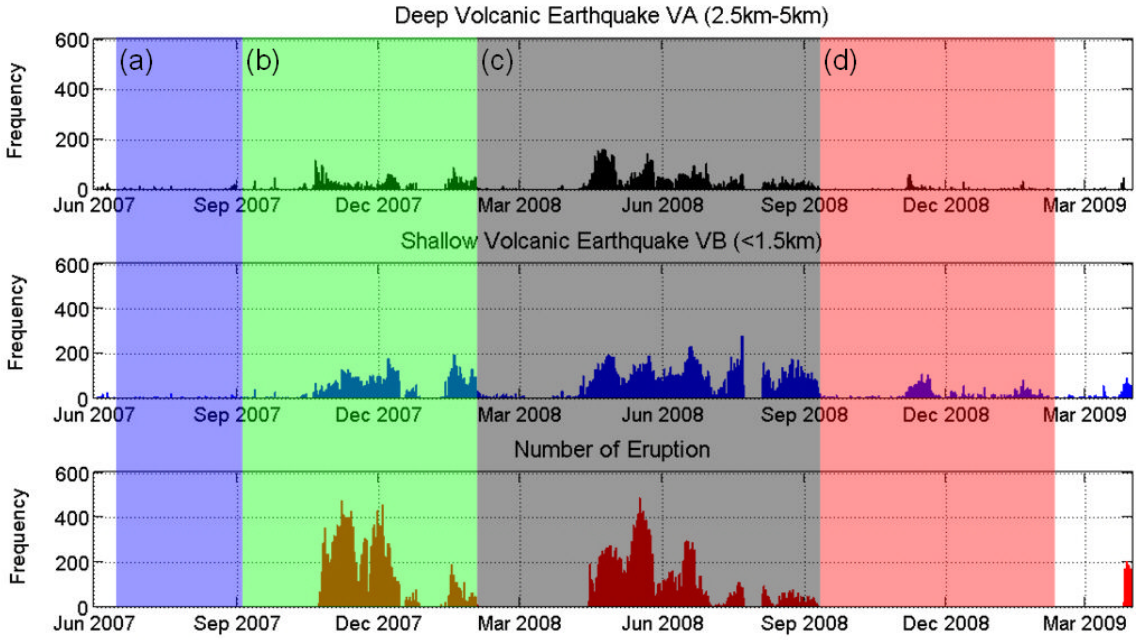

Figure 6.7 The Three Types of Seismic Data for Anak Krakatau Volcano. (i) Daily data for deep volcanic earthquake (V_A); (ii) Daily data for shallow volcanic earthquake (V_B); (iii) Daily data for volcanic earthquake related to eruptions. The data were recorded from June 2007 to March 2009 for Anak Krakatau Volcano. Each color in this graph represents the time of observation interferograms, blue color (a) for June 2007 to September 2007, green (b) for September 2007 to February 2008, black (c) for February 2008 to September 2008, and red (d) for September 2008 to February 2009. Seismic data were obtained from the Center of Volcanology and Geological Hazard Mitigation, Bandung-Indonesia.

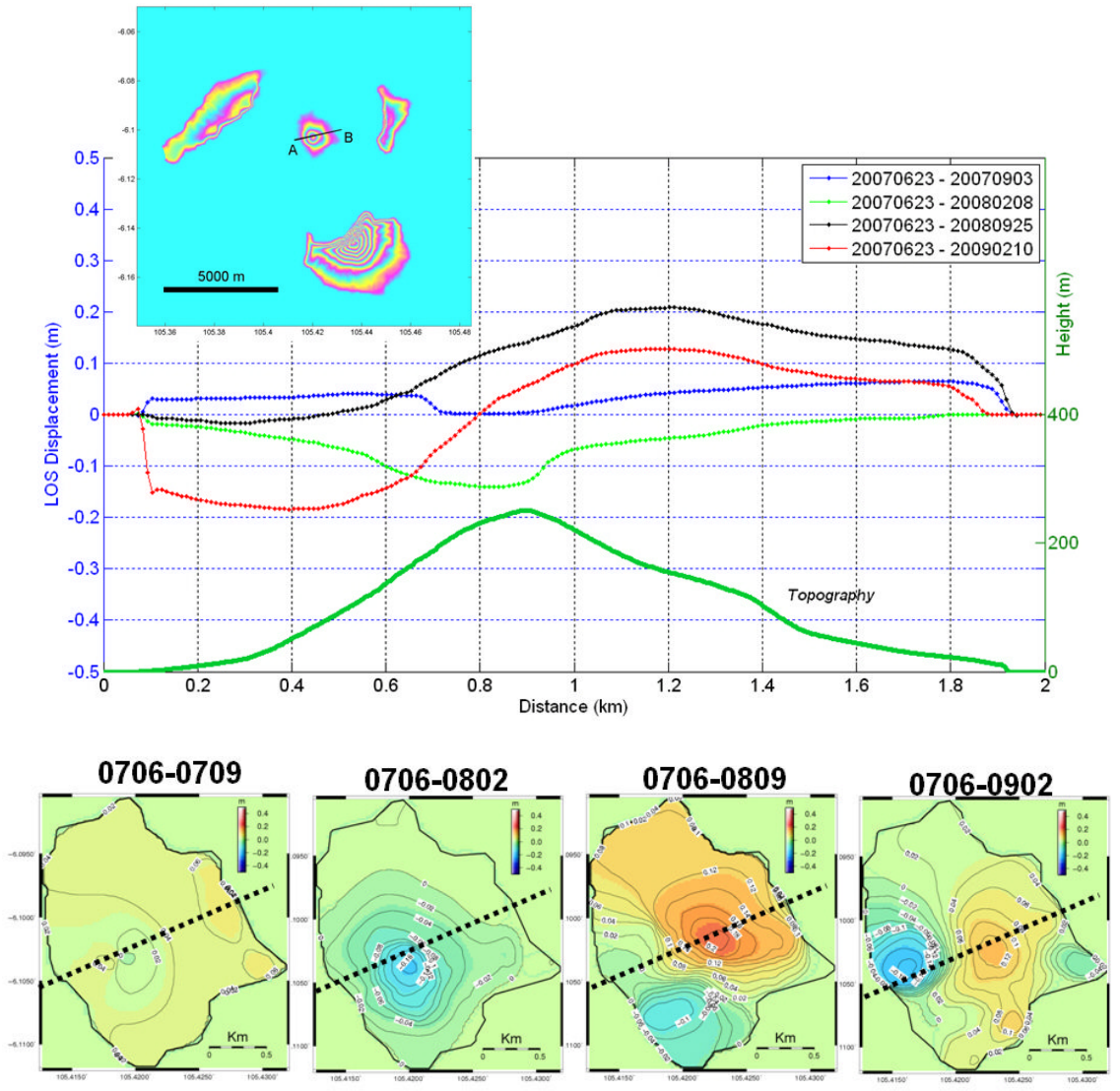

Figure 6.8 The LOS Displacement Profile for Anak Krakatau Volcano. These profiles are derived from vertical displacement InSAR estimates that represents period of observations.

Table 6.2 Fault and Dislocation Geometry Parameter for Anak Krakatau Volcano

Period	ΔT (days)	L (m)	W (m)	Depth (m)	Dip (degree)	Strike (degree)	Rake (degree)	U_1 (m)	U_2 (m)	U_3 (m)
0706-0709	92	177	2000	400	68	340	-90	0	-0.3	3
0706-0802	230	241	1400	400	50	331	-90	0	-0.1	-2
0706-0809	460	550	1500	400	50	299	-90	0	-1	2
0706-0902	598	230	1000	400	50	343	-90	0	-3	4

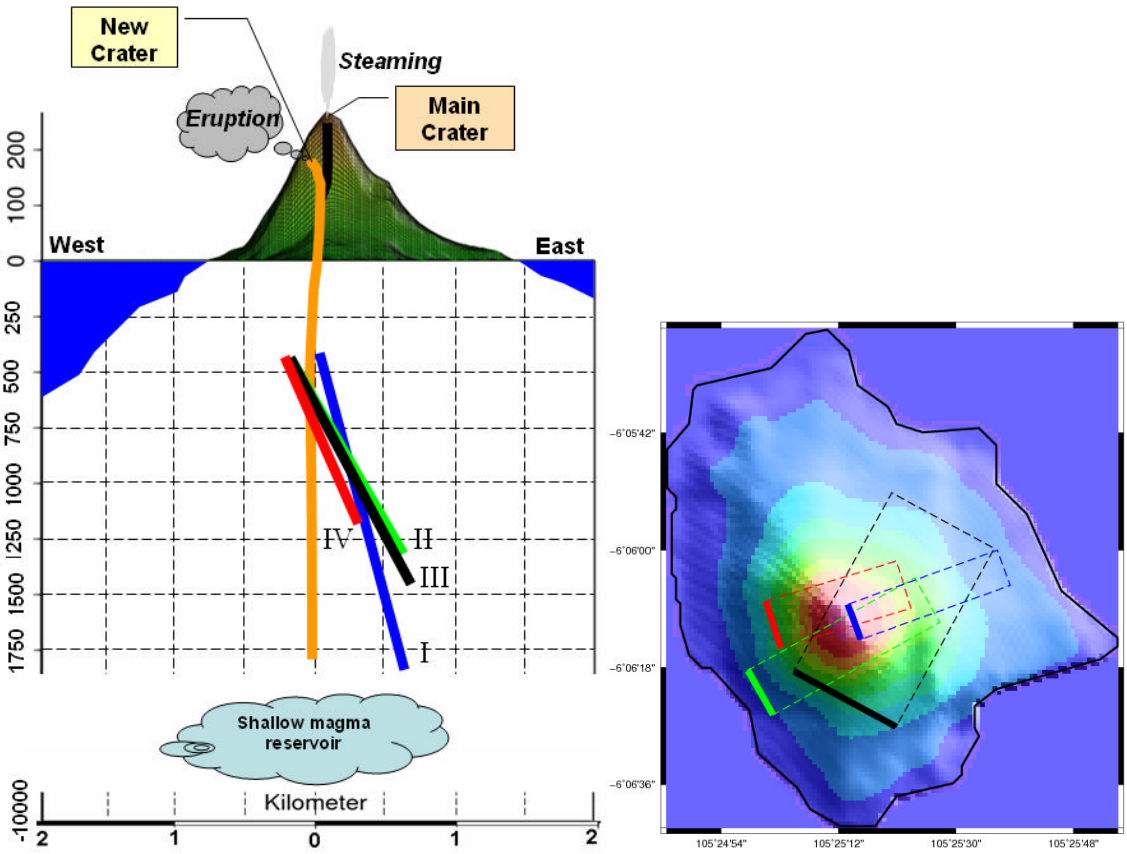

Figure 6.9 The Estimated Location of Rectangular Fault for Volcanic Source Model. The blue (I) corresponds to June 2007 – September 2007 interferogram; green (II), black (III) and red (IV) corresponds to June 2007 – February 2008, June 2007 – September 2008, June 2007 – February 2009 respectively.

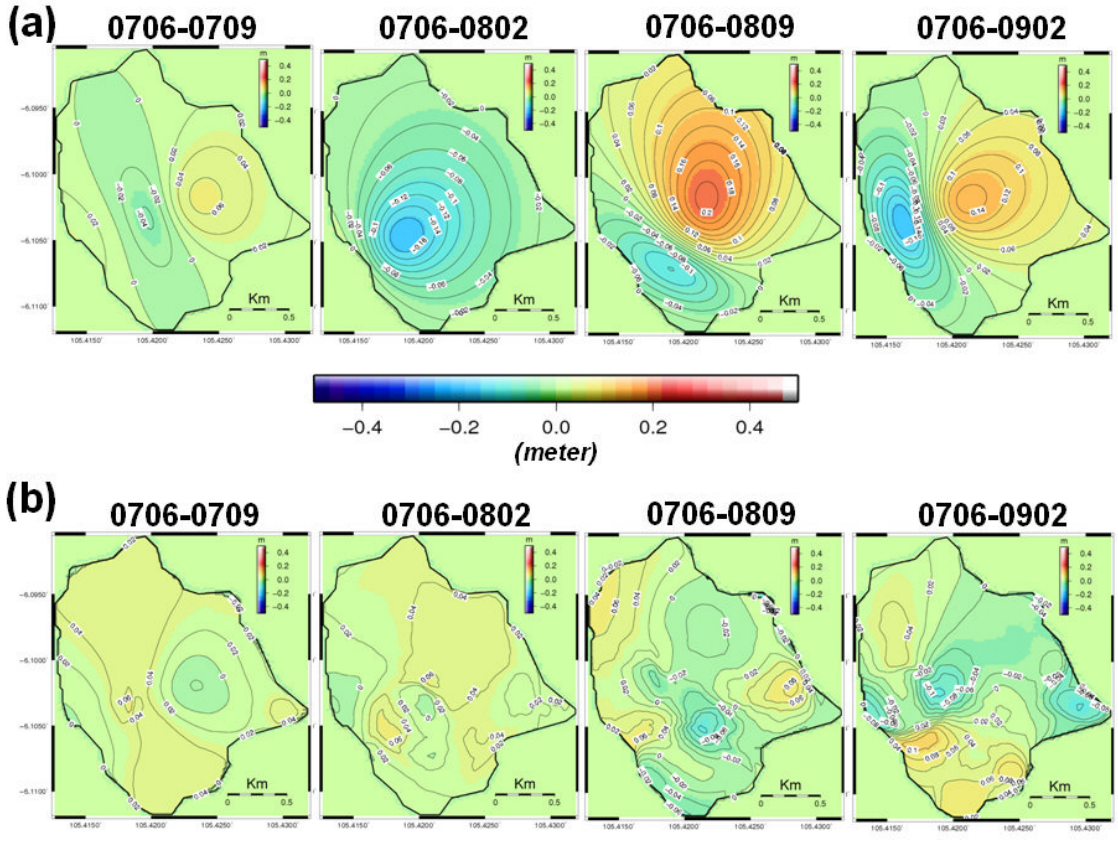

Figure 6.10 Model of Ground Deformation for Anak Krakatau Volcano. (a) The model was derived based on parameters that were listed in Table 6.2, (b) Illustrates the residual between filtered observation and model calculation.

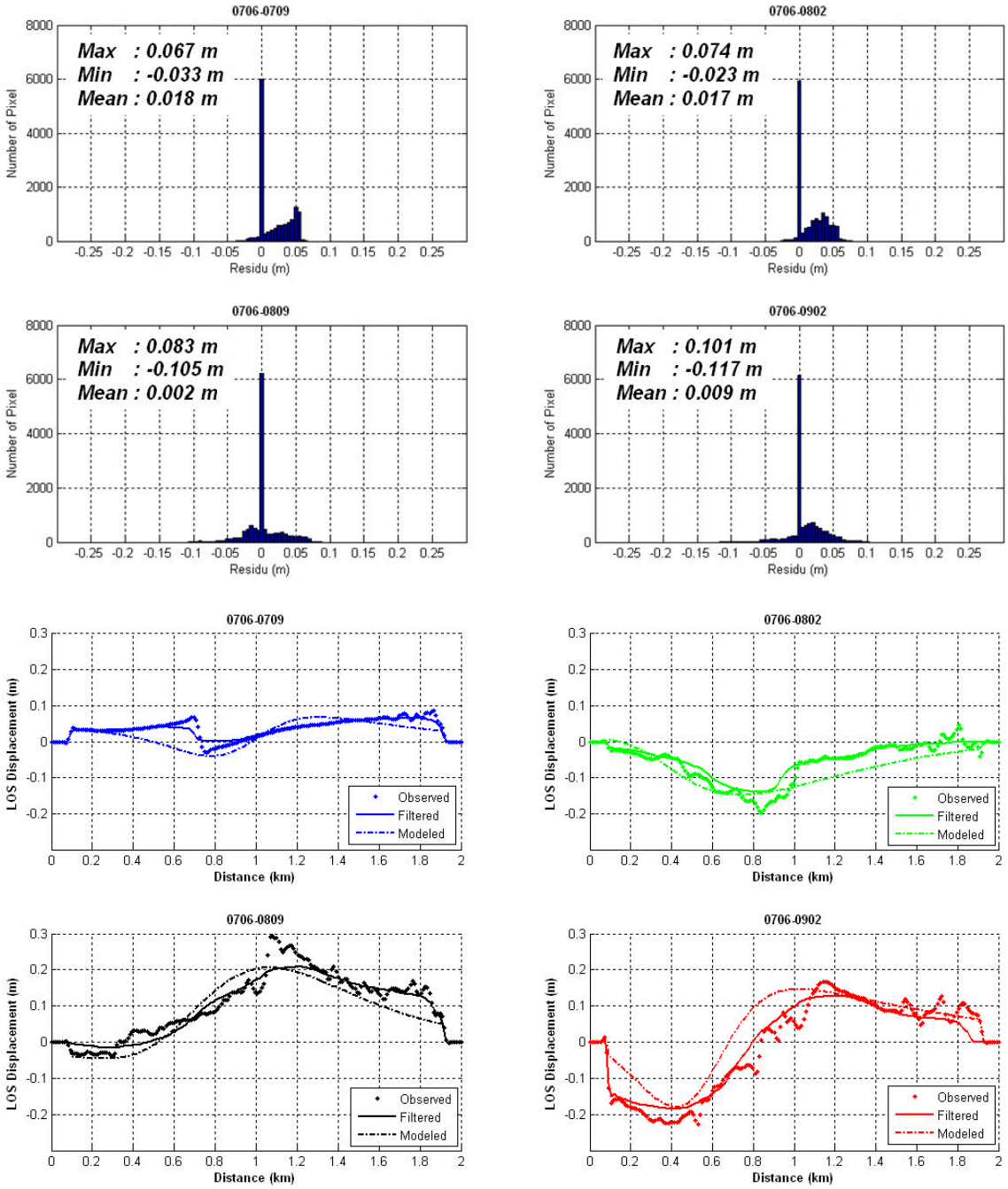

Figure 6.11 Assessment of Ground Deformation Model for Anak Krakatau. Upper part illustrates the histogram of residual between observation and calculation whereas the bottom part illustrates the profile comparison between observed, filtered and modeled along line A-B as explained in Figure 6.8.

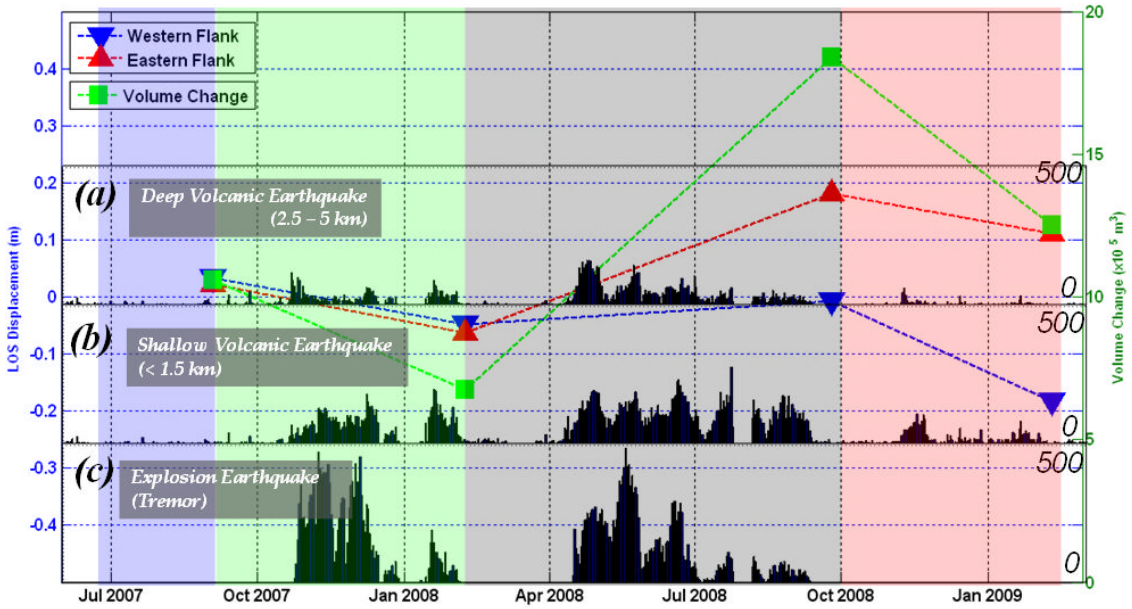

Figure 6.12 The Deformation of Anak Krakatau Volcano. It includes the line of sight displacements on the western and eastern flank of the cone, and the volumetric changes during the observation period, from June 2007 to February 2009. This figure also combined with the seismic data as explained in Figure 6.7 to show the relationship between deformation and volcanic activity.

Table 6.3 The Eruptive History of Anak Krakatau Volcano

Area of Activity	Eruption Period		Eruptive Characteristics					VEI
	Start	End	CERF	SIGC	ENPF	FLDS	FDMT	
Anak Krakatau	1927	1930	x - - x	x x - -	x x x -	- - - -	- - - -	2
Anak Krakatau	1931	1932	x x - -	- - - x	x - - -	- - - -	- - - -	2
Anak Krakatau	1932	1934	x - - -	- - - x	x - - -	- - - -	- - - -	3
Anak Krakatau	1935	1935	x - - -	x - - x	x - x -	- - - -	- - - -	2
Anak Krakatau	1936	1936	x - - -	? - - -	x - - -	- - - -	- - - -	1
Anak Krakatau	1937	1937	x - - -	- - - x	x - - -	- - - -	- - - -	2
Anak Krakatau	1938	1940	x - - -	x - - x	x - x -	- - - -	- - - -	3
Anak Krakatau	1941	1941	x - - -	- - - x	x - - -	- - - -	- - - -	2
Anak Krakatau	1942	1942	x - - -	- - - x	x - - -	- - - -	- - - -	2
Anak Krakatau	1943	1943	x - - -	- - - ?	? - - -	- - - -	- - - -	2
Anak Krakatau	1944	1944	x - - -	- - - ?	? - - -	- - - -	- - - -	2
Anak Krakatau	1945	1945	x - - -	- - - ?	? - - -	- - - -	- - - -	2
Anak Krakatau	1946	1946	x - - -	- - - x	x - - -	- - - -	- - - -	1
Anak Krakatau	1946	1947	x - - -	- - - x	x - - -	- - - -	- - - -	2
Anak Krakatau	1949	1949	x - - -	- - - x	x - - -	- - - -	- - - -	2
Anak Krakatau	1950	1950	x - - -	- - - x	x - - -	- - - -	- - - -	2
Anak Krakatau	1952	1952	x - - -	- - - x	x - - -	- - - -	- - - -	2
Anak Krakatau	1953	1953	x - - -	- - - x	x - - -	- - - -	- - - -	2
Anak Krakatau	1953	1953	x - - -	- - - x	x - - -	- - - -	- - - -	2
Anak Krakatau	1955	1955	x - - -	- - - -	x - - -	- - - -	- - - -	2
Anak Krakatau	1958	1959	x - - -	- - - x	x - - -	- - - -	- - - -	2
Anak Krakatau	1959	1963	x - - -	- - - x	x - - -	x - - -	- - - -	2
Anak Krakatau	1965	1965	x - - -	- - - -	x - x -	? - - -	- - - -	1?
Anak Krakatau	1969	1969	- - - -	- - - -	- - - -	- - - -	- - - -	2?
Anak Krakatau	1972	1973	x x - -	- - - -	x - - -	x - - -	- - - -	2
Anak Krakatau	1975	1975	x - - -	- - - -	x - - -	x - - -	- - - -	2
Anak Krakatau	1978	1978	x - - -	- - - -	x - - -	- - - -	- - - -	1
Anak Krakatau	1979	1979	x - - -	- - - -	x - - -	x - - -	- - - -	2
Anak Krakatau	1980	1980	x - - -	- - - -	x - - -	x - - -	- - - -	2
Anak Krakatau	1981	1981	x - - -	- - - -	x - - -	- - - -	- - - -	1
Anak Krakatau	1988	1988	x x - -	- - - -	x - - -	x - - -	- - - -	2
Anak Krakatau	1992	1993	x - - -	- - - -	x - - -	x - - -	x - - -	1
Anak Krakatau	1994	1995	x - - -	- - - -	x - - -	- - - -	- - - -	2
Anak Krakatau	1996	1996	x - - -	- - - -	x - - -	x - - -	- - - -	2
Anak Krakatau	1997	1997	x - - -	- - - -	x - - -	- - - -	- - - -	2
Anak Krakatau	1999	1999	x - - -	- - - -	x - - -	- - - -	- - - -	2
Anak Krakatau	2000	2000	x - - -	- - - -	x - - -	- - - -	- - - -	1
Anak Krakatau	2001	2001	x - - -	- - - -	x - - -	- - - -	- - - -	1
Anak Krakatau	2007	2008	x - - -	- - - -	x x - -	x - - -	- - - -	2

*Data obtained from Smithsonian Institution (Venzke et al., 2002). Five eruptive characteristics: related to vent location: C = Central crater eruption, E = Flank vent, R = Radial fissure eruption, F = Regional

fissure eruption; related to interaction with water: S = Submarine eruption, I = New island formation, G = Sub-glacial eruption, C = Crater lake eruption; related to Tephra: E = Explosive, N = Pyroclastic flows, P = Phreatic explosions, F = Fumarolic activity; related to lava extrusion: F = Lava flows, L = Lava lake eruption, D = Dome extrusion, S = Spine extrusion; and related to damage: F= Fatalities, D = Damage (land, property, etc), M = Mudflows (lahars), T = Tsunami. Symbol Key: X = recorded, ? = uncertain, - = not recorded. VEI = Volcanic Explosivity Index.

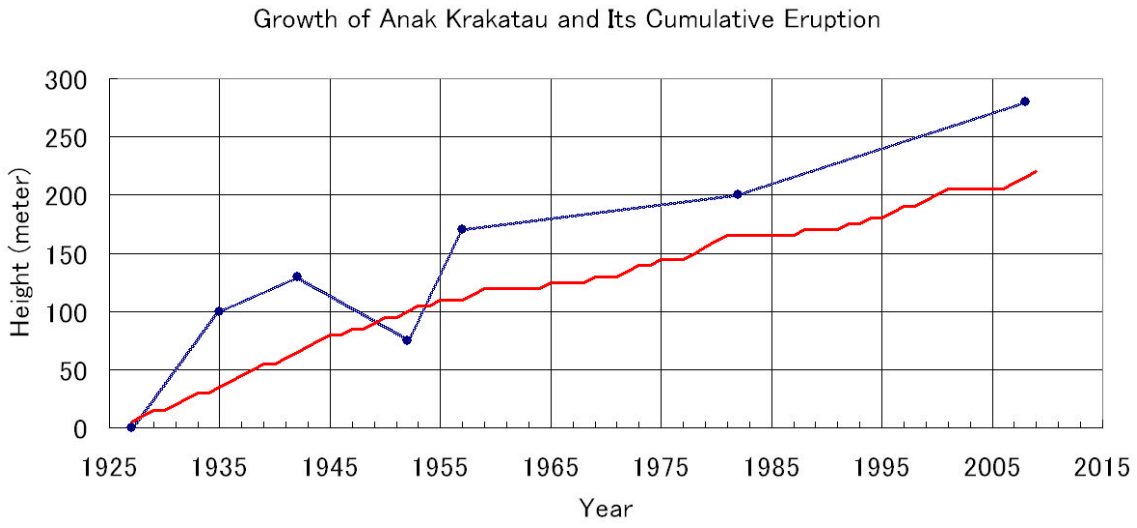

Figure 6.13 The Growth of Anak Krakatau and Its History Eruption. The growth of Anak Krakatau is illustrated in blue line (Sutawidjaja, 1997). The red line illustrates the non-scaled cumulative eruption period (Venzke et al., 2002). Horizontal line means silent period.

APPENDIX A

SCRIPT FOR SLC IMAGE GENERATION FOR RAW PALSAR DATA

```
#! /bin/csh -fe
echo " "
echo "PALSAR_PROC: Process PALSAR raw data (input are raw and leaderfile data files from)"
echo " "
if ($#argv < 4)then
 echo "usage: PALSAR_PROC_SLC <raw> <ldr> <ant> <ID> <RLK> <AZLK> [RAW_dir] [RC_dir]
[SLC_dir] [AZ_PATCH]\n"
 echo " "
 echo "       raw         (input) PALSAR raw data (input is IMG* file"
 echo "                           e.g.: IMG-HH-ALPSRP043591010-H1.0__A)"
 echo "       ldr         (input) PALSAR leaderfile (input is LED* file"
 echo "                           e.g.: LED-ALPSRP043591010-H1.0__A)"
 echo  "               ant                  (input) PALSAR antenna pattern file (e.g.
/home/gamma/MSP/sensors/palsar_ant_20061024.dat)"
 echo "       ID          identification code to be used in filenames (e.g. 20070214)"
 echo "       dir         directory path (e.g. /n/Ha; directories used will be"
 echo "                           /n/Ha/raw/20070214 and/n/Ha/slc/20070214)"
 echo "        RLK           number of range looks in the multilook intensity (MLI) image
(default=4)"
 echo "       AZLK         number of azimuth looks in the multilook intensity (MLI) image
(default=6)"
 echo "        radcal       radiometric calibration factor used oin az_proc (e.g. 6.0 dB,
default=6.0)"
 echo " "
 exit
endif


set raw = $1
set ldr = $2
set ant = $3
set ID  = $4
set dir = "."
set rawdir = "."
set slcdir = "."

set RLK = "4"
if ($#argv >= 5) then
 set RLK = $5
endif

set AZLK = "6"
if ($#argv >= 6) then
 set AZLK = $6
endif

set radcal = "6.0"
if ($#argv >= 7) then
 set radcal = $7
endif


# tests if required input files exist:
if(1) then
 echo "test if required input/output files and directories exist"
 if (-e "$raw" == 0 ) then
```

```
   echo "ERROR: PALSAR raw data file ($raw) does not exist"
   exit(-1)
 endif
 if (-e "$ldr" == 0 ) then
   echo "ERROR: PALSAR leaderfile ($ldr) does not exist"
   exit(-1)
 endif
 if ((-e "$ant" == 0 )) then
   echo "ERROR: PALSAR Antenna Data file $ant does not exist"
   exit(-1)
 endif
 if ((-e "$dir" == 0 )) then
   echo "ERROR: working directory $dir does not exist"
   exit(-1)
 endif
 echo "required input/output files and directories exist"

endif


# check if fixed raw data file exists (missing lines, range gate etc.)

cd $rawdir

set sarpar = "$rawdir/PALSAR_$ID.par"
set procpar = "$rawdir/p$ID.slc.par"
set antgain = "$rawdir/$ID.antenna.gain"
set p = "$rawdir/$ID"

echo ""
echo "PALSAR_proc $ldr $sarpar $procpar $raw $p.raw"
PALSAR_proc $ldr $sarpar $procpar $raw $p.raw > $p.PALSAR_proc.out

echo ""
echo "PALSAR_antpat $sarpar $procpar $ant $antgain"
PALSAR_antpat $sarpar $procpar $ant $antgain > $p.PALSAR_antpat.out

echo ""
echo "dop_mlcc $sarpar $procpar $p.raw $p.mlcc > $p.dop_mlcc.out"
dop_mlcc $sarpar $procpar $p.raw $p.mlcc > $p.dop_mlcc.out

echo ""
echo "azsp_IQ $sarpar $procpar $p.raw $p.azsp - - 24 > $p.azsp_IQ.out"
azsp_IQ $sarpar $procpar $p.raw $p.azsp - - 24 > $p.azsp_IQ.out

echo ""
echo "doppler $sarpar $procpar $p.raw $p.doppler - 24 0 > $p.doppler.out"
doppler $sarpar $procpar $p.fix $p.doppler - 24 0 > $p.doppler.out

echo ""
echo "rspec_IQ $sarpar $procpar $p.raw $p.rspec > $p.rspec_IQ.out"
rspec_IQ $sarpar $procpar $p.raw $p.rspec > $p.rspec_IQ.out

echo ""
echo "pre_rc $sarpar $procpar $p.raw $p.rc - - - - 2.12 8 - - 1 1.4 > $p.pre_rc.out"
pre_rc $sarpar $procpar $p.raw $p.rc - - - - 2.12 8 - - 1 1.4 > $p.pre_rc.out

echo ""
```

```
echo "autof $sarpar $procpar $p.rc $p.autof 2. 1 4096 - 1024 1 > $p.autof1.out"
autof $sarpar $procpar $p.rc $p.autof 2. 1 4096 - 1024 1 > $p.autof1.out
autof $sarpar $procpar $p.rc $p.autof 2. 1 4096 - 1024 1 > $p.autof2.out

echo ""
echo "az_proc $sarpar $procpar $p.rc $p.slc_d 16384 0 $radcal > $p.az_proc.out"
az_proc $sarpar $procpar $p.rc $p.slc_d 16384 0 $radcal 0 > $p.az_proc.out

set slc_width = `awk '$1 == "range_pixels:" {print $2}' $procpar`
set slc_nlines = `awk '$1 == "azimuth_pixels:" {print $2}' $procpar`

echo ""
echo "par_MSP $sarpar $procpar $p.slc.par_d > $p.par_MSP.out"
par_MSP $sarpar $procpar $p.slc.par_d > $p.par_MSP.out

SLC_ovr $p.slc_d $p.slc.par_d $p.slc $p.slc.par 2

echo ""
echo "multi_look $p.slc $p.slc.par $p.mli $p.mli.par $RLK $AZLK > $p.multi_look.out"
multi_look $p.slc $p.slc.par $p.mli $p.mli.par $RLK $AZLK > $p.multi_look.out

set mli_width = `awk '$1 == "range_samples:" {print $2}' $p.mli.par`
set mli_nlines = `awk '$1 == "azimuth_lines:" {print $2}' $p.mli.par`

echo ""
echo "raspwr $p.mli $mli_width 1 0 1 1 1. 1. 1 $p.mli.ras > $p.raspwr.out"
raspwr $p.mli $mli_width 1 0 5 5 1. 1. 1 $p.bmp > $p.raspwr.out
echo ""
```

APPENDIX B

SCRIPT FOR INTERFEROGRAM GENERATION BASED ON SLC IMAGES

```
#! /bin/tcsh -fe
if ($#argv < 5)then
  echo " "
  echo "INTERF_SLC: calculate interferogram, co-registered intensity images, and
correlation"
  echo " "
  echo "usage: INTERF_SLC <pass1> <pass2> <rlks> <azlks> <name> [algorithm] [cc_win]
[r_pos] [az_pos]"
  echo "       pass1       pass 1 identifier (example: pass number) reference"
  echo "       pass2       pass 2 identifier (example: pass number)"
  echo "       rlks        number of range looks"
  echo "       azlks       number of azimuth looks"
  echo "       name        name of interferogram ie interf or pass1_pass2"
  echo "       algorithm   algorithm used to determine offsets:"
  echo "                   1=intensity image cross correlation (default)"
  echo "                   2=fringe visibility"
  echo "       cc_win      window used for estimation of the correlation coefficient
(default: 3)"
  echo "       r_pos       range position of center of image patch for initial offset"
  echo "       az_pos      azimuth position of center of image patch for initial offset"
  echo ""
  exit(1)
endif

set CC_WIN = 3 #window used for coherence estimation
set CC_WGT = 1 #coherence estimation weighting: 0: uniform, 1: linear, 2: gaussian
set RLKS = $3
set AZLKS = $4
set name = $5

set ALGORITHM = 1
if ($#argv >= 6) then
  set ALGORITHM = $6
endif

# tests if required input files exist:
if(1) then
  echo "test if required input files exist"
  if (-e "$1.slc.par" == 0 ) then
    echo "ERROR: SLC parameter file ($1.slc.par) does not exist"
    exit(-1)
  endif
  if (-e "$2.slc.par" == 0 ) then
    echo "ERROR: SLC parameter file ($2.slc.par) does not exist"
    exit(-1)
  endif
  if (-e "$1.slc" == 0 ) then
    echo "ERROR: SLC data file ($1.slc) does not exist"
    exit(-1)
  endif
  if (-e "$2.slc" == 0 ) then
    echo "ERROR: SLC data file ($2.slc) does not exist"
    exit(-1)
  endif
  if (-e "$name.off" == 1 ) then
    echo "ERROR: ISP/offset parameter file ($name.off) does already exist"
    echo "Delete or rename the existing ISP/offset parameter file ($name.off)"
    echo "Script requires creation of a new ISP/offset parameter file"
    exit(-1)
  endif
  echo "required input/output files and directories exist"
endif

switch($ALGORITHM)
case "1":
  echo "OFFSET ALGORITHM: intensity image cross correlation"
  breaksw
case "2":
  echo "OFFSET ALGORITHM: fringe visibility"
  breaksw
default:
  echo ""
  echo "ERROR: invalid offset algorithm selected"
  echo ""
  exit(-1)
endsw

if ($#argv >= 7) then
  set CC_WIN = $7
endif

set R_POS = " "
if ($#argv >= 8) then
  set R_POS = $8
```

```
endif
set AZ_POS = " "
if ($#argv >= 9) then
  set AZ_POS = $9
endif

echo "number of range looks:   $RLKS"
echo "number of azimuth looks: $AZLKS"
echo "window size for correlation estimate: $CC_WIN"

if ($ALGORITHM == "1") then
  echo " "
  echo "create_offset $1.slc.par $2.slc.par $name.off $ALGORITHM"
  echo 'INTERF_SLC_1\n 0 0\n 32 32\n 128 128\n 7.0\n\n\n' > create_offset.in
  create_offset $1.slc.par $2.slc.par $name.off $ALGORITHM < create_offset.in
else
  echo " "
  echo "create_offset $1.slc.par $2.slc.par $name.off $ALGORITHM"
  echo 'INTERF_SLC_2\n 0 0\n 24 24\n 8 16\n 3.0\n\n\n' > create_offset.in
  create_offset $1.slc.par $2.slc.par $name.off $ALGORITHM < create_offset.in
endif

init_offset_orbit $1.slc.par $2.slc.par $name.off > out_init_offset_orbit.out

echo " "
echo "init_offset $1.slc $2.slc $1.slc.par $2.slc.par $name.off 1 $AZLKS $R_POS $AZ_POS >
out_init_offset.out"
init_offset $1.slc $2.slc $1.slc.par $2.slc.par $name.off 3 3 - - - - 7.0

echo ""
echo "init_offset $1.slc $2.slc $1.slc.par $2.slc.par $name.off 1 1 $R_POS $AZ_POS #>>
out_init_offset.out"
init_offset $1.slc $2.slc $1.slc.par $2.slc.par $name.off 1 1 $R_POS $AZ_POS >>
out_init_offset.out

if ($ALGORITHM == "1") then
  echo ""
  echo "offset_pwr $1.slc  $2.slc $1.slc.par $2.slc.par $name.off $name.offs $name.snr >
out_offset_pwr.out"
  offset_pwr $1.slc $2.slc $1.slc.par $2.slc.par $name.off $name.offs $name.snr >
out_offset_pwr.out
else
  echo ""
  echo "offset_SLC $1.slc  $2.slc $1.slc.par $2.slc.par $name.off $name.offs $name.snr >
out_offset_SLC.out"
  offset_SLC $1.slc $2.slc $1.slc.par $2.slc.par $name.off $name.offs $name.snr - - offsets
endif

#rm -f $name.coffs*
echo ""
echo "offset_fit $name.offs $name.snr  $name.off $name.coffs $name.coffsets >
out_offset_fit.out"
offset_fit $name.offs $name.snr  $name.off $name.coffs $name.coffsets - - 1

SLC_interp $2.slc $1.slc.par $2.slc.par $name.off $2.rslc $2.rslc.par
echo ""

##########
mv $name.off $name.off0
create_offset $1.slc.par $2.rslc.par $name.off_res < create_offset.in
offset_pwr $1.slc $2.rslc $1.slc.par $2.rslc.par $name.off_res $name.offs_res $name.snr_res
offset_fit $name.offs_res $name.snr_res  $name.off_res $name.coffs_res $name.coffsets_res -
3 1
offset_add $name.off0 $name.off_res $name.off
SLC_interp $2.slc $1.slc.par $2.slc.par $name.off $2.rslc $2.rslc.par
SLC_intf $1.slc $2.rslc $1.slc.par $2.rslc.par $name.off $name.int $RLKS $AZLKS

echo ""
echo "base_init $1.slc.par $2.slc.par $name.off $name.int $name.base 2 > out_base_init.out"
base_init $1.slc.par $2.rslc.par $name.off $name.int $name.base 2 > out_base_init.out

echo ""
echo "ph_slope_base $name.int $1.slc.par $name.off $name.base $name.flt"
ph_slope_base $name.int $1.slc.par $name.off $name.base $name.flt >out_phslopebase.out

set width =  `awk '$1 == "interferogram_width:" {print $2}' $name.off`
set nl =  `awk '$1 == "interferogram_azimuth_lines:" {print $2}' $name.off`

echo ""
echo "interferogram width, lines: $width $nl"

multi_look $1.slc $1.slc.par $1.mli $1.mli.par 2 3
multi_look $2.rslc $2.rslc.par $2.mli $2.mli.par 2 3
```

APPENDIX C

SCRIPT FOR DEM PREPARATION

```
#!/bin/sh
echo " "
DEM=$1        ### Derived from SRTM
DEMpar=$2     ### Parameter file
DEM2=$3       ### Second DEM derivation
DEM2par=$4    ### Parameter file
GC=$5            ### GC file
pass1=$6      ### Epoch 1 (master)
pass2=$7      ### Epoch 2 (slave)
echo " "
################
multi_look $6.slc $6.slc.par $6.mli $6.mli.par 4 6
multi_look $7.slc $7.slc.par $7.mli $7.mli.par 4 6
################
INTF_width=`awk '$1 == "range_samples:" {print $2}' $6.mli.par `
INTF_line=`awk '$1 == "azimuth_lines:" {print $2}' $6.mli.par `
echo " "
echo "Oversampling using gc_map"
echo " "
create_dem_par 50.dem_par $6.mli.par < dem50.in
dem_trans $DEMpar $DEM  $DEM2par $DEM2 1 1 0
gc_map $6.mli.par - $DEM2par $DEM2 $GC.gc_par $GC.gc map_to_rdc 2.5 2.5 pwr_sim_map - - - -
- - 8 3 128

echo " "
DEM_width=`awk '$1 == "width:" {print $2}' $GC.gc_par `
DEM_line=`awk '$1 == "nlines:" {print $2}' $GC.gc_par `
echo " "
mv map_to_rdc map_to_rdc.tmp
interp_ad map_to_rdc.tmp map_to_rdc $DEM_width 3 5 - 2 0 1
#interp_ad map_to_rdc.tmp map_to_rdc $DEM_width 8 16 16 2 0 1
echo " "
echo "Transform from radar to simulate using geocode"
#geocode map_to_rdc pwr_sim_map $DEM_width pwr_sim $INTF_width $INTF_line 0 0
geocode map_to_rdc pwr_sim_map $DEM_width pwr_sim $INTF_width $INTF_line 4
echo "create diff_par"
echo ' ' | awk '{printf "{\n\n\n\n\n"}' | create_diff_par $6.mli.par - tdiff.off 1
echo " "
init_offsetm pwr_sim $6.mli tdiff.off 1 1
echo " "
#offset_pwrm pwr_sim $6.mli tdiff.off tdiff.offs tdiff.snr 64 64 offsets 2 12 12 3.0
offset_pwrm pwr_sim $6.mli tdiff.off tdiff.offs tdiff.snr 64 64 offsets 4 32 32 3.0
offset_fitm tdiff.offs tdiff.snr tdiff.off tdiff.coffs tdiff.coffsets 3.0 3 1 #>
out_offsetfitm.out
echo " "
gc_map_fine map_to_rdc $DEM_width tdiff.off MAP_to_RDC 1
#geocode_back $6.mli $INTF_width MAP_to_RDC $6.mli.utm20 $DEM_width $DEM_line 2 0
geocode_back $6.mli $INTF_width MAP_to_RDC $6.mli.utm20 $DEM_width $DEM_line 0 0
raspwr $6.mli.utm20 $DEM_width
#geocode MAP_to_RDC $GC.gc $DEM_width hgt_sim $INTF_width $INTF_line 0 0
geocode MAP_to_RDC $GC.gc $DEM_width hgt_sim $INTF_width $INTF_line 4
rashgt hgt_sim $6.mli $INTF_width 1 1 0 1 1 100. 1. .4
rashgt_shd $GC.gc $GC.gc $DEM_width 10 10 1 $DEM_line 1 1 45 135 0.0 100. 1 $GC.gc.ras
echo " "
#geocode MAP_to_RDC pwr_sim_map $DEM_width pwr_sim $INTF_width $INTF_line 1 0
#echo " "
```

APPENDIX D

SCRIPT FOR DINSAR DATA PROCESSING

```
#!/bin/sh
SLC1=$1                 ###SLC file for master
SLC2=$2         ###SLC file for slave
SLCpar1=$3              ###Parameter file for master
SLCpar2=$4              ###Parameter file for slave
GC=$5                   ###GC file from DEM preparation
name=$6         ###Common name: "interf"
diff_par=$7             ###Common name: "par_diff"
out=$8          ###Output name

echo " "
INTF_width=`awk '$1 == "interferogram_width:" {print $2}' $name.off `
INTF_line=`awk '$1 == "interferogram_azimuth_lines:" {print $2}' $name.off `
DEM_width=`awk '$1 == "width:" {print $2}' $GC.gc_par `
DEM_line=`awk '$1 == "nlines:" {print $2}' $GC.gc_par `
echo " "
echo "Dimension is $INTF_width and $INTF_line"
echo "simulate topographic fringes using phase_sim"
#########
echo "base_init_orbit"
base_init $SLCpar1 $SLCpar2 $name.off $name.int $name.base_orbit 0 > out_base_init.out
#########
phase_sim $SLCpar1 $name.off $name.base_orbit hgt_sim $name.sim_orbit 0 0
SLC_diff_intf $SLC1 $SLC2 $SLCpar1 $SLCpar2 $name.off $name.sim_orbit $name.diff0 2 3 1 1
0.25 1 1
rasmph_pwr $name.diff0 $name.pwr1 $INTF_width 1 1 0 2 2 - - - diff0_orbit.bmp
base_init $SLCpar1 $SLCpar2 $name.off $name.diff0 $name.base_res 4
base_add $name.base_orbit $name.base_res $name.base 1
phase_sim $SLCpar1 $name.off $name.base hgt_sim $name.sim_add 0 0
mv $name.diff0 $name.diff0_orbit
SLC_diff_intf $SLC1 $SLC2 $SLCpar1 $SLCpar2 $name.off $name.sim_add $name.diff0 2 3 1 1
0.25 1 1
rasmph_pwr $name.diff0 $name.pwr1 $INTF_width 1 1 0 2 2 - - - diff0.bmp

#adapt_filt $name.diff0 $name.diff0.sm $INTF_width 0.4 32
#cc_wave $name.flt $name.pwr1 $name.pwr2 $name.cc0 $INTF_width 32 32 1

adf $name.diff0 $name.diff0.sm $name.cc0 $INTF_width 1.0 64 7 2 0 0 0.2
rasmph_pwr $name.diff0.sm $name.pwr1 $INTF_width 1 1 0 2 2 - - - diff0sm64.bmp
#########
rm -f interf.rascc_mask.ras
#rm -f interf.diff0.sm.unw22
rm -f interf.diff0.unw
rascc_mask $name.cc0 $name.pwr1 $INTF_width 1 1 0 1 1 0.35 0.3 0.9 1.0 0.35 1
interf.rascc_mask.ras
#multi_cpx $name.diff0.sm $name.off $name.diff0.sm22 $name.off22 2 2
#multi_real $name.cc0 $name.off $name.cc0.m22 $name.off22 2 2
#echo "Unwrapping the multireal"
mcf $name.diff0.sm $name.cc0 interf.rascc_mask.ras $name.diff0.sm.unw $INTF_width 1 0 0 - -
1 1 512
#mcf $name.diff0.sm22 $name.cc0.m22 interf.rascc_mask.ras $name.diff0.sm.unw22 908 1 0 0 -
- 1 1 512
#multi_real $name.diff0.sm.unw22 $name.off22 $name.diff0.unw_22 $name.off_22 -2 -2
#unw_model $name.diff0.sm $name.diff0.unw_22 $name.diff0.sm.unw $INTF_width 0 0
interp_ad $name.diff0.sm.unw $name.diff0.unw $INTF_width 32 9 18 2
##########
echo " "
echo ' ' | awk '{printf "\n\n\n\n\n"}' | create_diff_par $name.off - $diff_par 0
##########
sub_phase $name.diff0.unw $name.sim_orbit $diff_par $name.int.unw 0 1
rascc_mask $name.cc0 $name.pwr1 $INTF_width 1 1 0 1 1 0.6 0.6 0.9 1.0 0.35 1 gcp_mask.ras
extract_gcp hgt_sim $name.off $name.gcp 256 256 gcp_mask.ras
gcp_phase $name.int.unw $name.off $name.gcp $name.gcp_ph 3
cp $name.base_orbit $name.base
base_ls $SLCpar1 $name.off $name.gcp_ph $name.base 0 1 1 1 1 1. > out_base1.out
##########
echo "Resimulate unw_sim"
rm -f $diff_par
echo ' ' | awk '{printf "\n\n\n\n\n"}' | create_diff_par $name.off - $diff_par 0
phase_sim $SLCpar1 $name.off $name.base hgt_sim $name.unw.sim.p 0 1 >> out_phase_sim.out
echo "Sub_phase int_unw - sim_unw "
#diff_ls_fit $name.int.unw $name.unw.sim.p $diff_par 32 32 - lsfit.out > out_difflsfit.out
#diff_ls_unw $name.int.unw $name.unw.sim.p $diff_par $diff_par $name.diff1.unw 0 >
out_difflsunw.out
sub_phase $name.int.unw $name.unw.sim.p $diff_par $name.diff1.unw 0 0
atm_mod $name.diff1.unw hgt_sim $diff_par $name.atm 8 8 - > out_atm.out
sub_phase $name.diff1.unw $name.atm $diff_par $name.diff3.unw 0 0
#
rm -f disp_map
rm -f disp_mapV
rm -f disp_mapH
dispmap $name.diff3.unw hgt_sim $SLCpar1 $name.off disp_map 0
dispmap $name.diff3.unw hgt_sim $SLCpar1 $name.off disp_mapV 1
dispmap $name.diff3.unw hgt_sim $SLCpar1 $name.off disp_mapH 2
```

```
#
echo "#########GEOCODING################"
geocode_back interf.pwr1 $INTF_width MAP_to_RDC interf.pwr1.geo $DEM_width 0 0 0
geocode_back interf.int $INTF_width MAP_to_RDC interf.int.geo $DEM_width 0 0 1
geocode_back interf.flt $INTF_width MAP_to_RDC interf.flt.geo $DEM_width 0 0 1
geocode_back interf.cc0 $INTF_width MAP_to_RDC interf.cc.geo $DEM_width 0 0 0
#geocode_back $name.diff2.unw $INTF_width MAP_to_RDC $name.diff2.geo $DEM_width 0 3 0
geocode_back $name.diff3.unw $INTF_width MAP_to_RDC $name.diff_unw.geo $DEM_width 0 3 0
geocode_back $name.diff1.unw $INTF_width MAP_to_RDC $name.diff1.geo $DEM_width 0 3 0
geocode_back $name.atm $INTF_width MAP_to_RDC $name.atm.geo $DEM_width 0 3 0
##########
geocode_back disp_map $INTF_width MAP_to_RDC disp_map.geo $DEM_width 0 3 0
geocode_back disp_mapV $INTF_width MAP_to_RDC disp_mapV.geo $DEM_width 0 3 0
geocode_back disp_mapH $INTF_width MAP_to_RDC disp_mapH.geo $DEM_width 0 3 0
geocode_back hgt_sim $INTF_width MAP_to_RDC hgt_sim.geo $DEM_width 0 2
###########
rasmph_pwr interf.int.geo interf.pwr1.geo $DEM_width 1 1 0 2 2 1.0 0.5 1 $out.int.geo.bmp
rasmph_pwr interf.flt.geo interf.pwr1.geo $DEM_width 1 1 0 2 2 1.0 0.5 1 $out.flt.geo.bmp
rascc interf.cc.geo interf.pwr1.geo $DEM_width 1 1 0 2 2 0.1 0.9 1 0.5 1 $out.cc.geo.bmp
raspwr interf.pwr1.geo $DEM_width 1 0 2 2 1. .5 1 $out.pwr.geo.bmp
rashgt disp_map.geo interf.pwr1.geo $DEM_width 1 1 0 2 2 0.02 1. .5 1 $out.dispmap.geo.bmp
rashgt disp_mapV.geo interf.pwr1.geo $DEM_width 1 1 0 2 2 0.02 1. .5 1
$out.dispmapV.geo.bmp
rashgt disp_mapH.geo interf.pwr1.geo $DEM_width 1 1 0 2 2 0.02 1. .5 1
$out.dispmapH.geo.bmp
rashgt hgt_sim.geo interf.pwr1.geo $DEM_width 1 1 0 2 2 100 1. .5 1 $out_sim_geo.bmp
###########
rasrmg interf.atm.geo interf.pwr1.geo $DEM_width 1 1 0 2 2 0.33333 1. .5 .0 1
$out.atm.geo.bmp
rasrmg interf.diff1.geo interf.pwr1.geo $DEM_width 1 1 0 2 2 0.33333 1. .5 .0 1
$out.diff1.geo.bmp
rasrmg interf.diff_unw.geo interf.pwr1.geo $DEM_width 1 1 0 2 2 0.33333 1. .5 .0 1
$out.diff_unw.geo.bmp
#rasrmg interf.diff2.geo interf.pwr1.geo $DEM_width 1 1 0 2 2 0.33333 1. .5 .0 1
$out.diff2.geo.bmp
echo "geo dimension $DEM_width $DEM_line ; int dimension $INTF_width $INTF_line"
#rm *.slc
rm pwr_sim*
rm map_*
```

APPENDIX E

PUBLICATIONS

1. Agustan, Djoko Nugroho, Lena Sumargana, Irwan Meilano, Mohd. Effendi Daud, Fumiaki Kimata, Yusuf S. Djadjadihardja. (2009) Water Level Changes in Weh Island due to the Postseismic Deformation of the 2004 Sumatra-Andaman Earthquake, Advances in Geosciences, Vol. 13, Ch. 14, World Scientific Publishing Co., pp. 203 – 213.
2. Agustan, Fumiaki Kimata. (in press) Ground Deformation Assessment around Toba Lake using DInSAR, Advances in Geosciences, Vol. 19, SE-0067, World Scientific Publishing Co.
3. Agustan, Fumaki Kimata, Hasanuddin Abidin, Yoga Era Pamitro (2010) Measuring ground deformation of the tropical volcano, Ibu, using ALOS-PALSAR data, Remote Sensing Letters, 1(1): 37-44, Taylor & Francis. DOI: 10.1080/01431160903246717.